

Modeling and Simulation of Soft Switching in Traction Inverter

Master's Thesis in Electric Power Engineering

Kuang Lu, Lakshmi Priya Gandla

DEPARTMENT OF ELECTRICAL ENGINEERING

CHALMERS UNIVERSITY OF TECHNOLOGY

Gothenburg, Sweden 2023

www.chalmers.se

MASTER'S THESIS 2023

Modeling and Simulation of Soft Switching in Traction Inverter

Kuang Lu, Lakshmi Priya Gandla



CHALMERS
UNIVERSITY OF TECHNOLOGY

Department of Energy and Environment
Electrical Engineering Division
CHALMERS UNIVERSITY OF TECHNOLOGY
Gothenburg, Sweden 2023

Modeling and Simulation of Soft Switching in Traction Inverter
Kuang Lu, Lakshmi Priya Gandla

© Kuang Lu, Lakshmi Priya Gandla, 2023.

Supervisor: Kooros Moabber, Volvo Cars
Examiner: Stefan Lundberg, Chalmers University of Technology

Master's Thesis 2023
Department of Energy and Environment
Division of Electrical Engineering
Electric Power Engineering MPEPO
Chalmers University of Technology
SE-412 96 Gothenburg
Telephone +46 31 772 1000

Cover: Resonant inductor current in soft switching inverter
Typeset in L^AT_EX
Printed by Chalmers Reproservice
Gothenburg, Sweden 2023

Abstract

In this thesis, two soft switching inverter topologies the Active Clamped Resonant DC Link Inverter (ACRDCLI) and the Auxiliary Resonant Commutated Pole Inverter (ARCPI) are designed. Their performance is compared with the Hard Switched Inverter (HSI) in simulations. In order to ensure the balance of the soft switching resonant circuit and to achieve a certain reference current, the parameters of the circuit components are selected according to the references and modified appropriately. The load is modelled as a Permanent Magnet Synchronous Machine (PMSM) equivalent circuit and the parameters are taken from the Finite Element Method (FEM) data based on a fixed operating point. The total power losses in the switches are calculated based on the loss profile in Piecewise Linear Electrical Circuit Simulation (PLECS).

Hysteresis current control and Space Vector Pulse Width Modulation (SVPWM) are used to control the current of the ACRDCLI and the ARCPI respectively. Two different state machines have also been designed to ensure the proper operation of the two soft switching topologies. The same control method is used for two HSIs as a control group to have a fair comparison. By simulating each topology under the similar conditions it can be concluded that each topology can output similar power and the total losses in two soft switching topologies are reduced by 18% compared to HSI, especially in switching losses by 98% at 33 kHz switching frequency.

Due to the circuit complexity and poor Total Harmonic Distortion (THD) performance of the ACRDCLI only the ARCPI is further analysed for different switching frequencies and current operating points. At high switching frequency of 80 kHz the THD value for the ARCPI is 0.286 % and for the HSI the THD is 0.366 %. With increasing switching frequency the THD for the ARCPI is smaller than the HSI and the ACRDCLI. The ARCPI gives the maximum efficiency of 97.57 % at 25 kHz switching frequency. Compared to the HSI there is an efficiency improvement of 1.71 % with the ARCPI at high switching frequency.

Acknowledgements

We would like to thank our thesis examiner as well as our favorite lecturer, Stefan Lundberg, for his patient guidance and enlightening suggestions through each stage of the process. This thesis would not be possible without Stefan's support with power electronics and the control system. We also want to thank Lars Johansson from Volvo Cars, who provided us the valuable opportunity and support. We are grateful to our supervisor Kooros Moabber in Volvo Cars for providing an interesting and challenging thesis topic and for giving us all the technical support.

Kuang Lu, Lakshmi Priya Gandla, Gothenburg, March 2023

Contents

List of Figures	xi
List of Tables	xvii
Acronyms	xix
Symbols	xx
1 Introduction	1
1.1 Background	1
1.2 Aim	2
1.3 Scope and limitation	2
2 Electric Drive System	3
2.1 PMSM model	3
2.1.1 abc to dq transformation	4
2.1.2 The dq model of the PMSM	5
2.2 Three-phase Hard Switched Inverter	6
2.2.1 Space Vector Pulse Width Modulation (SVPWM)	8
2.2.2 Hysteresis Current Control	9
2.3 Losses in HSI	10
2.3.1 Switching losses	12
2.3.2 Conduction losses	13
2.4 Thermal model of the Switch	14
2.5 Total Harmonic Distortion (THD)	14
3 Active Clamped Resonant DC Link Inverter	15
3.1 Three-phase ACRDCLI	15
3.2 ACRDCLI equivalent circuit	16
3.3 Losses in ACRDCLI	20
3.3.1 Clamp Switch Losses	21
3.3.2 ESR Losses	21
3.3.3 Resonant Inductor Losses	22
4 Auxiliary Resonant Commutated Pole Inverter	23
4.1 Three-phase ARCPI	23
4.2 Single-phase ARCPI Circuit	24

4.3	Losses in ARCPI	30
4.3.1	Auxiliary Switch losses	30
4.3.2	ESR losses	30
4.3.3	Resonant Inductor losses	31
5	Case setup	33
5.1	Machine Setup	33
5.2	HSI Setup	33
5.2.1	Reference Calculation	35
5.2.2	Triggered Subsystem	35
5.2.3	Power Losses Calculation	35
5.3	ACRDCLI Setup	37
5.3.1	Reference resonant inductor current calculation	39
5.3.2	Triggered subsystem	39
5.3.3	State Machine	39
5.3.4	Average Frequency Calculation	41
5.4	ARCPI Setup	41
5.4.1	Reference Calculation	42
5.4.2	State Machine	42
6	Results and Discussions	45
6.1	HSI	45
6.2	ACRDCLI	47
6.3	ARCPI	51
6.4	Comparison of ACRDCLI, ARCPI with HSI	61
6.5	ARCPI performance	63
6.6	Component number comparison	69
7	Conclusion and Future work	71
	References	73

List of Figures

2.1.1 Simplified equivalent circuit for phase a of the PMSM. The circuit is similar for the other two phases b and c.	3
2.1.2 The PMSM equivalent circuit for the d-axis and the q-axis, the circuits described by (2.1.10).	6
2.2.1 The three phase two level HSI comprising of the DC link capacitor, C_{DC} , and the six MOSFETs, S_1 to S_6 , connected to the battery, the DC voltage source, and to the PMSM modeled as an RL-circuit and a voltage source.	7
2.2.2 The eight possible voltage vectors that can be created with a three-phase inverter. The vectors V_1 to V_6 are the active vectors and V_0 and V_7 are the zero vectors. In the figure the six switching sectors are also defined, I to VI.	8
2.2.3 Theoretical waveform showing hysteresis band current control where actual current $i(t)$ is compared with the reference current $i_{ref}(t)$ and $2\Delta i$ is the hysteresis bandwidth.	10
2.3.1 Theoretical waveform showing simplified turn on-off characteristics in the phase leg for phase a in the three-phase HSI. The highlighted area in the bottom plot represents the switching energies.	11
2.4.1 Equivalent circuit showing the thermal description of one of the MOSFET modules.	14
3.1.1 The three-phase ACRDCLI comprising of the auxiliary circuit connected to the battery, the DC voltage source and the six MOSFETs, S_1 to S_6 , and to the PMSM modeled as an RL-circuit and a voltage source.	16
3.2.1 Equivalent circuit of the ACRDCLI under load operation.	17
3.2.2 Simulated waveforms of the ACRDCLI showing the resonant DC link voltage V_{Cr} and the resonant inductor current i_{Lr} illustrating four operating states.	17
3.2.3 Circuit during the boost period before $t_1 < 0$, where S_m is on and S_c is off.	18
3.2.4 Circuit during pre-charge transition between t_1 to t_2 , where the S_m is off and the S_c is off.	19
3.2.5 Circuits during clamping period between t_2 to t_3 where the S_m is off and the S_c is on.	19

3.2.6	Circuit during the discharge transition period between t_3 to t_4 , where S_m is off and S_c is off.	20
3.3.1	Capacitor Equivalent Circuit	21
4.1.1	The three-phase ARCPI comprizing of the auxiliary circuit connected to the battery, the DC voltage source and six MOSFETS, S_1 to S_6 and to the PMSM modeled as an RL-circuit and a voltage source. . .	23
4.2.1	The single-phase ARCPI circuit.	24
4.2.2	Simulated waveforms of the single-phase ARCPI circuit showing the load current i_{load} , the resonant inductor current i_{Lr} , the voltages across the top and bottom switches V_{Cr1} , V_{Cr2} showing State 1 to State 5 operation with respect to the Pulse Width Modulation (PWM) control signal.	25
4.2.3	The single-phase ARCPI during State 1, free-wheeling operation where S_2 is on and A_1 , A_2 and S_1 are off.	26
4.2.4	The single-phase ARCPI State 2, pre-charge of the resonant inductor with the load current where S_2 , A_2 are on and S_1 , A_1 are off.	26
4.2.5	The single-phase ARCPI State 3, resonant operation where A_2 is on and S_1 , S_2 and A_1 are off.	27
4.2.6	The single-phase ARCPI State 4, discharge of resonant inductor where S_1 , A_2 are on and S_2 , A_1 are off.	27
4.2.7	The single-phase ARCPI State 5, with completion of transition where S_1 is on and S_2 , A_1 , A_2 are off.	28
4.2.8	The single-phase ARCPI State 6, where S_1 , S_2 , A_1 and A_2 are turned off.	29
4.2.9	Simulated waveforms of the single-phase ARCPI circuit showing the load current i_{load} , the resonant inductor current i_{Lr} , the voltages across the top and the bottom switches V_{Cr1} , V_{Cr2} showing State 6 with respect to PWM control signal	29
5.2.1	Overview of the three-phase HSI with the SVPWM control showing the SVPWM block and the reference calculation block.	34
5.2.2	Overview of the three-phase HSI with the hysteresis current control showing the triggered subsystem block and the reference calculation block.	34
5.2.3	MOSFET turn-on (left plot) and turn-off (right plot) switching energies profile.	36
5.2.4	MOSFET conduction losses profile	37
5.2.5	Diode conduction losses profile	37
5.3.1	Overview of the three-phase ACRDCLI with hysteresis current control system showing different blocks for the zero crossing detection logic, state machine, triggered subsystem and the reference calculation.	38
5.3.2	Flow chart for the ACRDCLI with pre-conditions showing state 1 to state 4.	40
5.4.1	Overview of the three-phase ARCPI with the hysteresis current control system showing different blocks for the zero crossing detection logic, the state machine, the SVPWM, and the reference calculation	41

5.4.2	Flow chart for the phase leg for phase a in the three-phase ARCPI. The load current represents the phase current, in this case $i_{load} = i_a$.	43
6.1.1	Simulated waveforms of HSI with SVPWM showing voltage and current (top plot), switching energies (middle plot) and conduction losses (bottom plot) of the one of the Metal Oxide Semiconductor Field Effect Transistors (MOSFETs) in phase leg a. The PWM switching frequency $f_{sw} = 33$ kHz.	46
6.1.2	Zoomed-in plot showing voltage and current (top plot), switching energies (middle plot), and conduction losses (bottom plot) of the one of the MOSFETs in phase leg a. The PWM switching frequency $f_{sw} = 33$ kHz.	47
6.2.1	Resonant DC link voltage V_{Cr} waveform for the three-phase ACRD-CLI with a total clamping voltage of 1200 V.	48
6.2.2	Simulated plots of three-phase ACRDCLI showing current flowing through the resonant inductor i_{Lr} (blue plot), inverter DC link current i_x (red plot) and the reference inductor current i_{Lr}^* (yellow plot)	48
6.2.3	Voltage across the clamp capacitor Cc (top plot) and the current flowing through the clamp circuit (bottom plot). The initial voltage of the clamp capacitor is 500 V.	49
6.2.4	Zoomed in plot showing the voltage across the clamp capacitor Cc (top plot) and the current flowing through the clamp circuit (bottom plot).	50
6.3.1	Simulated phase b waveforms for the three-phase ARCPI when the load current is positive. The voltage across the resonant capacitors (top plot) which are connected parallel to the top and bottom switches and the current is through the auxiliary circuit (bottom plot). The input DC link voltage is 700 V and the PWM switching frequency is 45 kHz.	51
6.3.2	Zoomed-in simulated phase b waveforms showing turn on and off instants for the three-phase ARCPI when the load current is positive. The voltage across the resonant capacitors (top plot) is connected to the top and bottom switches and the current is through the auxiliary circuit (bottom plot). The input DC link voltage is 700 V and the PWM switching frequency is 45 kHz.	52
6.3.3	Simulated phase c waveform for the three-phase ARCPI when the load current is negative. The voltage across the resonant capacitors (top plot) which are connected parallel to the top and bottom switches and the current is through the auxiliary circuit (bottom plot). The input DC link voltage is 700 V and the PWM switching frequency is 45 kHz.	53

6.3.4	Zoomed-in simulated phase c waveforms showing turn on and off instants for the three-phase ARCPI when the load current is negative. The voltage across the resonant capacitors (top plot) is connected to the top and bottom switches and the current is through the auxiliary circuit (bottom plot). The input DC link voltage is 700 V and the PWM switching frequency is 45 kHz.	54
6.3.5	Top plot shows the three-phase output current and the bottom plot shows the resonant current inductor currents flowing through the auxiliary circuit.	55
6.3.6	Zoomed-in plot of phase A output current (top plot) and resonant inductor current (bottom plot). Zero crossing can be seen when the current changes from negative to positive.	56
6.3.7	Simulated waveforms of ARCPI showing voltage and current (top plot), switching energies (middle plot), and conduction losses (bottom plot) of one of the MOSFETs in phase leg A. The PWM switching frequency $f_{sw} = 33$ kHz.	57
6.3.8	Zoomed-in plot showing voltage and current (top plot), switching energies (middle plot), and conduction losses (bottom plot) of the one of the MOSFETs in phase leg A. The PWM switching frequency $f_{sw} = 33$ kHz.	58
6.3.9	Simulated waveforms of the three-phase ARCPI showing the voltage across and the current flowing (top plot), switching energies (middle plot), and the conduction losses (bottom plot) of one of the auxiliary switch A_1 in phase leg a auxiliary circuit.	59
6.3.10	Zoomed-in plot showing voltage and current (top plot), switching energies (middle plot), and conduction losses (bottom plot) of one of the Auxiliary switch A_1 in phase leg A.	60
6.5.1	The average total power losses of the ARCPI and the HSI during one electrical period with different current operating points and switching frequencies. The left plot shows the Total power losses vs the current i_q ranging from 100 A to 550 A with the PWM switching frequency of 33 kHz. The right plot shows the total power losses vs switching frequencies from 25 kHz to 80 kHz with the current $i_q = 550$ A	63
6.5.2	The average MOSFET switching losses of ARCPI and HSI during one electrical period. (Left plot) shows the switching losses with different current operating points and (Right plot) shows the total switching losses with different switching frequencies.	64
6.5.3	Simulated results showing the distribution of the power losses of HSI during one electrical period with different switching frequency operating points where the reference $i_q = 550$ A.	65
6.5.4	The resonant inductor losses of ARCPI during one electrical period with different switching frequency operating points and quality factor where the reference current $i_q = 550$ A.	66
6.5.5	The average load current THD of ARCPI and HSI during three electrical periods with $i_q = 550$ A and different switching frequency operating points.	67

6.5.6 Efficiency of ARCPI and HSI during one electrical period with $i_q =$
550 A and different switching frequency operating points. 68

List of Tables

5.1.1 Machine parameters used in each simulated topologies	33
5.3.1 ACRDCLI circuit parameters and the initial settings	38
5.3.2 Switching combination table for the six main switches of the ACRDCLI	40
5.4.1 ARCPI circuit parameters and the initial settings	42
5.4.2 Switching combination table for the ten states of the phase leg for phase a in the three-phase ARCPI.	44
6.4.1 Average total power losses, efficiency, and the THD of all topologies at 33 kHz switching frequency.	61
6.6.1 Circuit component number for three topologies	69

Acronyms

AC	Alternating Current. 1, 3
ACRDCLI	Active Clamped Resonant DC Link Inverter. v, xi, xvii, 1, 2, 15–18, 20–22, 30, 33–35, 37–39, 41, 42, 45, 61, 62, 69, 71
ARCPI	Auxiliary Resonant Commutated Pole Inverter. v, xii, xiii, xvii, 2, 23–31, 33–35, 41–45, 51, 56, 58, 61–65, 67–69, 71, 72
DC	Direct Current. 1
EMF	Electromotive force. 35, 39, 42
EMI	Electromagnetic Interference. 1
ESR	Equivalent Series Resistance. 20–22, 30, 31, 66, 71
EV	Electric Vehicle. 1–3, 71
FEM	Finite Element Method. v, 33
HSI	Hard Switched Inverter. v, xiii, 1–3, 6, 7, 11, 15, 23, 33, 45, 46, 61–65, 68, 69, 71, 72
MOSFET	Metal Oxide Semiconductor Field Effect Transistor. xiii, xiv, 6, 12, 13, 20, 21, 30, 35–37, 45–47, 58
PLECS	Piecewise Linear Electrical Circuit Simulation. v, 33
PMSM	Permanent Magnet Synchronous Machine. v, xii, 3, 6, 7, 23, 33
PWM	Pulse Width Modulation. xii–xiv, 1, 23, 25, 26, 29, 42, 43, 46, 47, 51, 52, 58, 63
QRDCLI	Quasi Resonant DC Link Inverter. 2, 71

RTI	Resonant Transition Inverter. 2
SiC	Silicon Carbide. 35
SVPWM	Space Vector Pulse Width Modulation. v, xiii, 2, 7, 8, 33, 35, 41, 42, 46, 71
THD	Total Harmonic Distortion. 3, 7, 14, 62, 67, 71
ZCS	Zero Current Switching. 58
ZVS	Zero Voltage Switching. 18, 20, 52, 57

Symbols

Symbol	Description	Unit
A_1	Auxiliary switch connected to phase A and is triggered when the load current is negative	-
A_2	Auxiliary switch connected to phase A and is triggered when the load current is positive	-
A_4	Auxiliary switch connected to phase B and is triggered when the load current is positive	-
A_5	Auxiliary switch connected to phase C and is triggered when the load current is negative	-
A_6	Auxiliary switch connected to phase C and is triggered when the load current is positive	-
C_c	Clamp Capacitor	F
C_{r1}	Resonant Capacitor across the Main Switch S_1	F
C_{r2}	Resonant Capacitor across the Main Switch S_2	F
C_{r6}	Resonant Capacitor across the Main Switch S_6	F
C_r	Resonant Capacitor	F
D_c	Clamp Diode	-
I_x	Constant Current Source	A
L_d	Inductance in the d direction	H
L_q	Inductance in the q direction	H
L_{ra}	Resonant Inductor connected in series to auxiliary auxiliary for phase A	H
L_{rc}	Resonant Inductor connected in series to auxiliary swicthes for phase C	H
L_r	Resonant Inductor	H
L_s	Phase inductance	H
R_s	Phase resistance	Ω
S_1	Top main switch in phase leg A	-
S_2	Bottom main switch in phase leg A	-
S_3	Top main switch in phase leg B	-
S_4	Bottom main switch in phase leg B	-
S_5	Top main switch in phase leg C	-
S_6	Bottom main switch in phase leg c	-
S_c	Clamp Switch	-
S_m	Main switch	-
V_{Cc}	Clamp Capacitor Voltage	V

Symbol	Description	Unit
V_{Cr1}	Voltage across the resonant capacitor Cr1	V
V_{Cr2}	Voltage across the resonant capacitor Cr2	V
V_{Cr3}	Voltage across the resonant capacitor Cr3	V
V_{Cr4}	Voltage across the resonant capacitor Cr4	V
V_{Cr5}	Voltage across the resonant capacitor Cr5	V
V_{Cr6}	Voltage across the resonant capacitor Cr6	V
V_{Cr}	Voltage across the resonant capacitor Cr	V
$V_{DC} + V_{Cc}$	Total Clamping Voltage	V
V_{DC}	DC link voltage	V
ψ_m	Magnet flux linkage	Wb
Q	Quality factor	-
e_a	Back EMF	V
f_f	Fundamental frequency	Hz
f_{sw}	Switching frequency	Hz
i_{Cc}	Clamp Current	A
i_{Lrb}	Resonant Inductor Current flowing through phase B Auxiliary circuit	A
i_{Lrc}	Resonant Inductor Current flowing through phase C Auxiliary circuit	A
i_{Lr}^*	Reference Resonant Inductor Current	A
i_{Lr}	Resonant Inductor Current	A
i_a	Phase a current	A
i_{load}	Load current	A
i_x	Inverter DC link current	A
u_a	Phase voltage	V

1

Introduction

1.1 Background

Growing environmental concerns and compulsory legislation leads to that the automotive industry are investing significant resources in the development of hybrid and fully Electric Vehicles (EVs). Battery and power electronics are acknowledged as the two leading technologies for the development of today's EV [1]. The voltage source Hard Switched Inverter (HSI) are widely used in modern traction drives to convert Direct Current (DC) from the battery to Alternating Current (AC) to drive the traction electric machines. HSI with Pulse Width Modulation (PWM) has been a great choice in EV applications because of its simple circuit design and robust control scheme [2]. The significant requirements for traction inverters are expressed in terms of overall reliability, performance and cost [3].

In HSI, both voltage and current are applied to the switch during turn on and off transitions. This results in switching losses, that can be significant at high switching frequencies, which in turn results in switching stresses on the devices and Electromagnetic Interference (EMI) generation due to high voltage slew rates (dv/dt) [4]. To resolve these problems, various soft switching topologies have been investigated for the traction inverters to improve efficiency and reduce the EMI by turning the devices on and off at nearly zero voltage or current. Recent achievements suggest that soft switching inverters may be more reliable and efficient compared to HSI [5]. Various soft switching topologies have different advantages and disadvantages, so the different topologies need to be investigated to understand which ones that are most suitable for EV applications.

Over a decade ago the Active Clamped Resonant DC Link Inverter (ACRDCLI) was introduced and it was one of the first type of DC link soft switching topology [6]. A resonant inductor-capacitor circuit and active clamp circuit are added between the DC link and the inverter bridge switches to provide a resonant voltage and to clamp the bus voltage from overshooting [7]. In [2], a performance comparison with an HSI shows that the ACRDCLI is more efficient at switching frequencies above 10 kHz and promising for EV applications. Some fundamental issues with this circuit include the resonant voltage overshoot and the large inductor. Furthermore, the ACRDCLI requires the main switches to operate simultaneously, which requires a more complicated PWM scheme [8].

To overcome the problems caused by the ACRDCLI, a new concept of Resonant Transition Inverter (RTI) was proposed, which includes the Auxiliary Resonant Commutated Pole Inverter ARCPI [9]. The ARCPI topology receives the DC link voltage through the center-tapped DC link capacitor and uses three sets of independently controlled auxiliary switches to create zero voltage switching [10]. A comparative study of different RTI results shows that the ARCPI has the best efficiency improvement at higher switching frequencies and is more suitable for EV applications [11].

1.2 Aim

The aim of this thesis is to model and simulate two soft switching topologies, the ACRDCLI and ARCPI. The two soft switching topologies are compared with a HSI to evaluate their performance based on different criteria, such as switching losses and harmonics.

1.3 Scope and limitation

This project will focus on a simulation study of soft switching inverters and their comparison with HSI. There are different soft switching topologies, but only two types of topologies will be evaluated in this project.

Based on the literature study, the ACRDCLI was selected as it is one of the first DC link soft switching topologies. This topology requires a minimum number of extra switches and resonant components and is simple to implement [12]. Initially a simplified ACRDCLI under load simulation will be simulated to understand the behavior of soft switching in this topology. Later a three-phase ACRDCLI will be simulated and compared with the three-phase HSI. Hysteresis current control will be implemented for this topology. To implement the Space Vector Pulse Width Modulation (SVPWM) control method, an improved topology Quasi Resonant DC Link Inverter (QRDCLI) was introduced in recent times [13]. However, this topology will not be investigated. Instead, another concept of the soft switching technique, the ARCPI will be evaluated. The advantage of this topology is that the SVPWM control technique can be implemented [14]. The ARCPI topology with artificial intelligence control was recently introduced by the company Pre-Switch Inc. In comparison to HSI their results show a reduction of switching losses by 99 % and efficiency of 99 % with 100 kHz switching frequency [15] [16]. The simulation results of the ARCPI will be compared to the ACRDCLI and the HSI. However, the drawbacks with the ARCPI are additional components and complexity of the control system.

As this project is focused on the inverter power losses, the complete battery model and DC link capacitor are not considered. Instead, the battery is simplified as a DC voltage source and its losses are ignored. The losses of the electrical machine are also not considered.

2

Electric Drive System

This chapter describes the main components in the electric drive system of an EV, except for the battery that is, as mentioned before, only modeled as a voltage source. In the first section the theory for the Permanent Magnet Synchronous Machine (PMSM) is described. After this the three-phase Hard Switched Inverter (HSI), which is used as the reference inverter in this thesis project, is introduced together with a description of different modulation techniques for the inverter. Finally, the equations for calculating the inverter power losses and the Total Harmonic Distortion (THD), that are used to evaluate the performance of the investigated inverters, are introduced.

2.1 PMSM model

The PMSM is an AC synchronous motor where the field excitation is provided by permanent magnets in the rotor. The machine is magnetised by permanent magnets that are attached to the rotor.

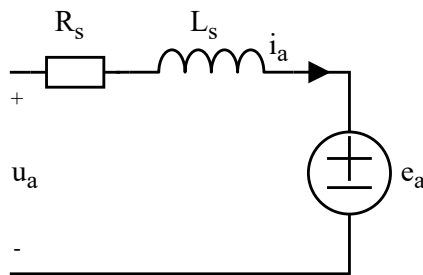


Figure 2.1.1: Simplified equivalent circuit for phase a of the PMSM. The circuit is similar for the other two phases b and c.

Figure 2.1.1 shows the simplified equivalent circuit of the PMSM for phase a. The simplification that is made is that it is assumed that the phase inductance L_s is constant and not depending on the rotor position, as it is in a salient machine. The circuit includes the phase voltage u_a , the phase current i_a , the phase resistance R_s , the phase inductance L_s and the back EMF e_a which is caused by the rotational speed of the rotor. Based on this the three phase voltages can be expressed as [17]

$$u_a = R_s i_a + \frac{d\Psi_a}{dt} \quad (2.1.1a)$$

$$u_b = R_s i_b + \frac{d\Psi_b}{dt} \quad (2.1.1b)$$

$$u_c = R_s i_c + \frac{d\Psi_c}{dt}. \quad (2.1.1c)$$

where Ψ_a is the flux linkage for phase a. The three-phase voltages can be combined using vectors and matrices as

$$u_{abc} = R_s i_{abc} + \frac{d\Psi_{abc}}{dt}. \quad (2.1.2)$$

Three-phase flux can be obtained as

$$\Psi_{abc} = \begin{bmatrix} L_s & 0 & 0 \\ 0 & L_s & 0 \\ 0 & 0 & L_s \end{bmatrix} i_{abc} + \Psi_m \begin{bmatrix} \cos(\theta_r) \\ \cos\left(\theta_r - \frac{2\pi}{3}\right) \\ \cos\left(\theta_r + \frac{2\pi}{3}\right) \end{bmatrix}. \quad (2.1.3)$$

where:

- Ψ_{abc} is the three phase flux linkage,
- i_{abc} is the three phase currents,
- Ψ_m is the magnet flux linkage,
- θ_r is the electrical rotor angle.

2.1.1 abc to dq transformation

To simplify the modeling of the PMSM transformations are commonly used. First the three-phase machine is transformed into a two-phase machine by using Clarke transformation, the transformation between abc to $\alpha\beta$ quantities. In matrix form the Clarke transformation can be written as [18]

$$\begin{bmatrix} u_a \\ u_b \\ u_c \end{bmatrix} = \begin{bmatrix} 1 & 0 \\ -\frac{1}{2} & \frac{\sqrt{3}}{2} \\ -\frac{1}{2} & -\frac{\sqrt{3}}{2} \end{bmatrix} \begin{bmatrix} u_\alpha \\ u_\beta \end{bmatrix}. \quad (2.1.4)$$

The transformation in (2.1.4) is for amplitude invariant scaling, meaning that the amplitude of the phase voltage (the peak value) is equal to the length of the complex vector $u^s = u_\alpha + ju_\beta$. The inverse of this transformation gives the transformation from $\alpha\beta$ to abc quantities, which can be expressed as

$$\begin{bmatrix} u_\alpha \\ u_\beta \end{bmatrix} = \begin{bmatrix} \frac{2}{3} & -\frac{1}{3} & -\frac{1}{3} \\ 0 & \frac{1}{\sqrt{3}} & -\frac{1}{\sqrt{3}} \end{bmatrix} \begin{bmatrix} u_a \\ u_b \\ u_c \end{bmatrix}. \quad (2.1.5)$$

To further simplify the modeling the AC $\alpha\beta$ quantities are transformed to, in steady-state, DC dq quantities. The dq coordinate system is a synchronous coordinate

system rotating at the electrical speed of the rotor. The real and imaginary axis of these vectors is constant in a steady state. The Park transformation is used to move from the stationary $\alpha\beta$ -system to the rotating dq-system and it can be expressed as

$$u = u_d + ju_q = u^s e^{-j\theta_r}. \quad (2.1.6)$$

Similarly, the transformation from the rotating to the stationary system can be defined as:

$$u^s = u e^{j\theta_r}. \quad (2.1.7)$$

The transformations can also be expressed in matrix form by splitting up the real and imaginary parts as

$$\begin{bmatrix} u_\alpha \\ u_\beta \end{bmatrix} = \begin{bmatrix} \cos \theta_r & -\sin \theta_r \\ \sin \theta_r & \cos \theta_r \end{bmatrix} \begin{bmatrix} u_d \\ u_q \end{bmatrix}. \quad (2.1.8)$$

$$\begin{bmatrix} u_d \\ u_q \end{bmatrix} = \begin{bmatrix} \cos \theta_r & \sin \theta_r \\ -\sin \theta_r & \cos \theta_r \end{bmatrix} \begin{bmatrix} u_\alpha \\ u_\beta \end{bmatrix} \quad (2.1.9)$$

The DC quantities are helpful for the analysis and the implementation of a control system, as it is easier to design a controller for signals that are constant in steady-state instead of alternating [19].

2.1.2 The dq model of the PMSM

By using the Clark and Park transformations the three-phase PMSM model can be transformed to the two phase dq-model as

$$u_d = R_s i_d + L_s \frac{di_d}{dt} - \omega_r L_s i_q \quad (2.1.10a)$$

$$u_q = R_s i_q + L_s \frac{di_q}{dt} + \omega_r L_s i_d + \omega_r \Psi_m. \quad (2.1.10b)$$

where:

- u_d is the voltage in d direction,
- u_q is the voltage in q direction,
- i_d is the current in d direction,
- i_q is the current in q direction,
- ω_r is the electrical rotor speed = $w_{mek} n_p$,
- w_{mek} is the mechanical rotor speed.

Figure 2.1.2 shows the PMSM machine model in the dq-system from (2.1.10) as an electric circuit where the resistance models the resistive voltage drop in the stator, the dynamic voltage drop of the stator inductance, $j\omega_r L_s i$ the steady-state voltage drop of the stator inductance and $w_r \psi_m$ represents the back EMF of the PMSM. The torque produced by the PMSM in the dq-system can be calculated as

$$T_e = \frac{3n_p}{2} \Psi_m i_q \quad (2.1.11)$$

Since the PMSM is modeled as a non-salient machine it is only the q-current that produces torque. Due to this the d-current is set to zero for low speeds of the PMSM, since it does not contribute to the torque. The d-current is used to reduce the effect of the back-emf at high speeds, it is then negative and it is decreasing with increasing speeds.

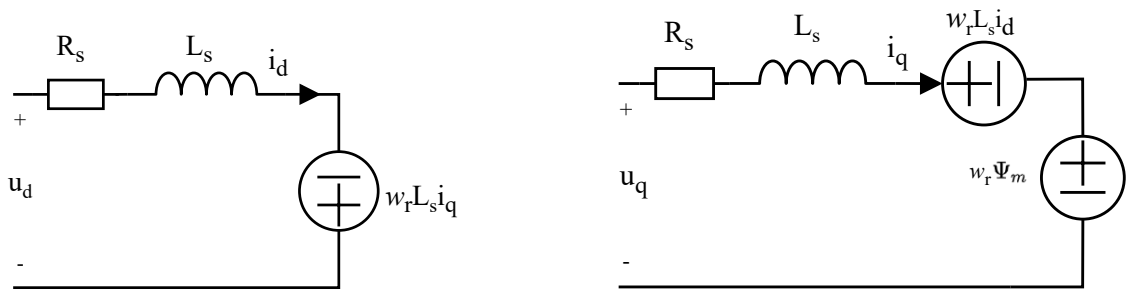


Figure 2.1.2: The PMSM equivalent circuit for the d-axis and the q-axis, the circuits described by (2.1.10).

2.2 Three-phase Hard Switched Inverter

The three-phase HSI is a power electronic converter that converts the input DC voltage V_{DC} , the battery voltage, to a variable three-phase AC voltage that is supplied to the PMSM, as shown in Figure 2.2.1. As can be seen in the figure the three-phase inverter is built up from three phase legs, where each phase leg comprises of two series connected MOSFET switches with their anti-parallel diode. The phase of the PMSM is connected between the switches, phase a is connected between switch S_1 and S_2 , phase b between S_3 and S_4 and phase c between S_5 and S_6 .

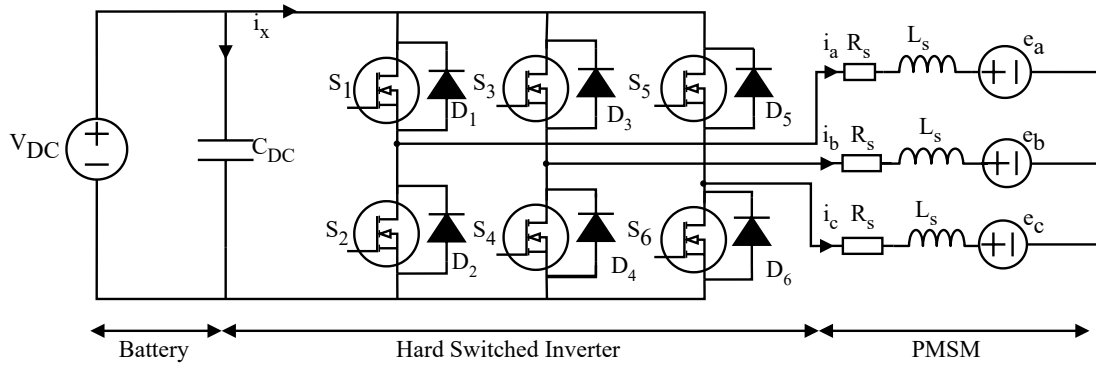


Figure 2.2.1: The three phase two level HSI comprising of the DC link capacitor, C_{DC} , and the six MOSFETs, S_1 to S_6 , connected to the battery, the DC voltage source, and to the PMSM modeled as an RL-circuit and a voltage source.

For the HSI the switches in a phase leg is on (conducting) one at the time, i.e. when the top switch is on the bottom switch is off and when the top switch is off then the bottom switch is on. In the transition between changing the switch that is on both switches are off for a short period of time, the blanking time, to avoid shorting the DC voltage. Each phase leg can have two different switching states S_x . If the switching state for the phase is 1 then the top switch is on and if it is 0 then the bottom switch is on (x is a, b or c). This gives that there are eight possible switch combinations (S_a, S_b, S_c) for the three phase legs. Each switch combination generates a three-phase voltage to the PMSM and if these voltages are transformed with the Clarke transformation eight $\alpha\beta$ voltage vectors are obtained.

In Figure 2.2.2 these eight voltage vectors are shown, V_0 to V_7 , together with the corresponding switch combination (S_a, S_b, S_c) . The vectors V_1 to V_6 are the active vectors and V_0 and V_7 are the zero vectors. The active vectors have the same length, equal to $2/3V_{DC}$. To generate the required voltage to the PMSM, for example the voltage reference vector, V_{ref} , in Figure 2.2.2 the two closest active vectors, V_1 and V_2 in this example, together with the zero vectors are used to produce the reference vector as the average voltage over the switching period. The switching period t_{sw} is much smaller than the fundamental frequency of the PMSM, f_f . How the active and the zero vectors are used to generate the wanted voltage depends on which modulation technique that is used.

In the following two sections the Space Vector Pulse Width Modulation (SVPWM) modulation technique and the Hysteresis Current Control are explained. After these sections the losses generated in the switches will be explained and it is shown how the THD that is generated by the switching is calculated.

2.2.1 Space Vector Pulse Width Modulation (SVPWM)

When using SVPWM, the reference voltage vector, i.e. the voltage that should be delivered to the PMSM, is expressed as the time average of the three voltage vectors that define the hexagonal sector in which the reference voltage vector lies. The six hexagonal sectors, the voltage vectors and the switching states are shown in Figure 2.2.2. In the figure a example voltage reference vector, V_{ref} , is shown and this vector is in the I sector. The first sector is defined by the active voltage vector V_1 that is generated by the switch combination (100), the active voltage vector V_2 that is generated by the switch combination (110) and the zero voltage vectors V_0 and V_7 . The reference voltage vector is generated as a time average of these vectors as [20]

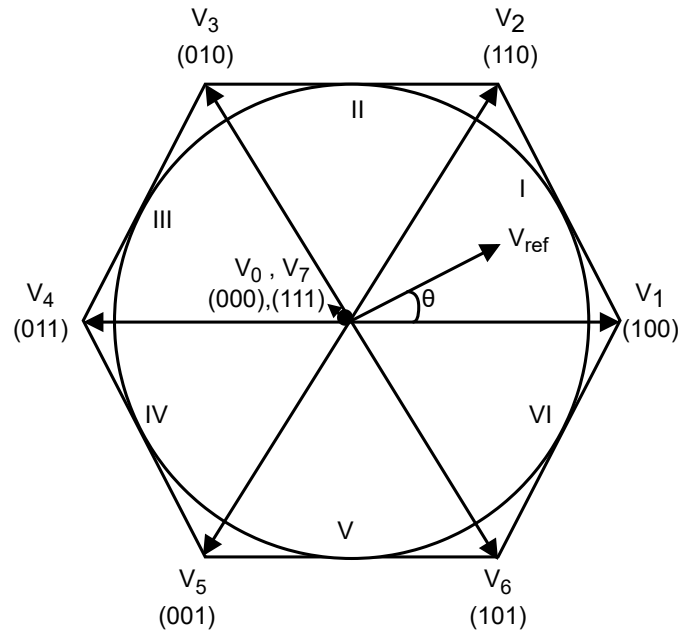


Figure 2.2.2: The eight possible voltage vectors that can be created with a three-phase inverter. The vectors V_1 to V_6 are the active vectors and V_0 and V_7 are the zero vectors. In the figure the six switching sectors are also defined, I to VI.

$$V_{ref} = \frac{t_1}{t_{sw}} \cdot V_1 + \frac{t_2}{t_{sw}} \cdot V_2 + \frac{t_0}{t_{sw}} \cdot V_0. \quad (2.2.1)$$

where:

- V_{ref} is the reference voltage in the $\alpha\beta$ frame,
- t_1 is the on time of V_1 ,
- t_2 is the on time of V_2 ,
- t_0 is the on time of V_0 or V_7 ,
- t_{sw} is the switching time.

The voltage vectors can be defined using the sine rule

$$V_0 = 0, V_1 = \frac{2}{3}V_{DC}, V_2 = \frac{2}{3}V_{DC}e^{j\frac{\pi}{3}}. \quad (2.2.2)$$

The relative on time duration for the active vectors and zero vectors can be derived using the above relations and by separating the reference voltage into real and imaginary parts which gives

$$t_1 = t_s w \frac{\sqrt{3}|V_{ref}|}{V_{DC}} \sin\left(\frac{\pi}{3} - \theta\right) \quad (2.2.3a)$$

$$t_2 = t_s w \frac{\sqrt{3}|V_{ref}|}{V_{DC}} \sin(\theta) \quad (2.2.3b)$$

$$t_0 = t_{sw} - t_1 - t_2. \quad (2.2.3c)$$

where θ is the angle between the reference voltage vector and the beginning vector of the sector, the angle between V_{ref} and V_1 in the example used here..

2.2.2 Hysteresis Current Control

With hysteresis current control the system does not generate a specific voltage vector, a reference voltage, it instead puts out the voltage vector, one of the possible eight vectors, that "keeps" the phase currents within the hysteresis band. The hysteresis current control is one of the simplest current control methods because of the ease of implementation and quick response [21].

In the hysteresis current control, the switching combinations (S_a, S_b, S_c) for the three-phase HSI are generated by comparing the three-phase output currents to the reference currents and the difference between them, the control error is send to the hysteresis function. The hysteresis function outputs 0 or 1 and the required output voltage is produced to the PMSM. Figure 2.2.3 shows the working principle of the hysteresis current control. This theoretical waveform will be used to explain the hysteresis current control to generate the switching states to one of the phase leg in the three-phase HSI. In the figure the actual load current $i(t)$ is compared with the reference current $i_{ref}(t)$ by the hysteresis function which has a dead band Δi . When the difference between the actual current and the reference current is greater than the hysteresis dead band the positive voltage is applied across the load and the $i(t)$ increases i.e the top switch is turned on. Similarly, when the difference between the actual current and the reference current is lower than the hysteresis dead band the negative voltage is put across the load and the $i(t)$ decreases, switching is reversed i.e bottom switch is turned on. The switching states for a phase leg can be defined as

$$i(t) - i_{ref}(t) > \Delta i \text{ then } S_1 = \text{on and, } S_2 = \text{off} \quad (2.2.4a)$$

$$i(t) - i_{ref}(t) < \Delta i \text{ then } S_1 = \text{off and, } S_2 = \text{on.} \quad (2.2.4b)$$

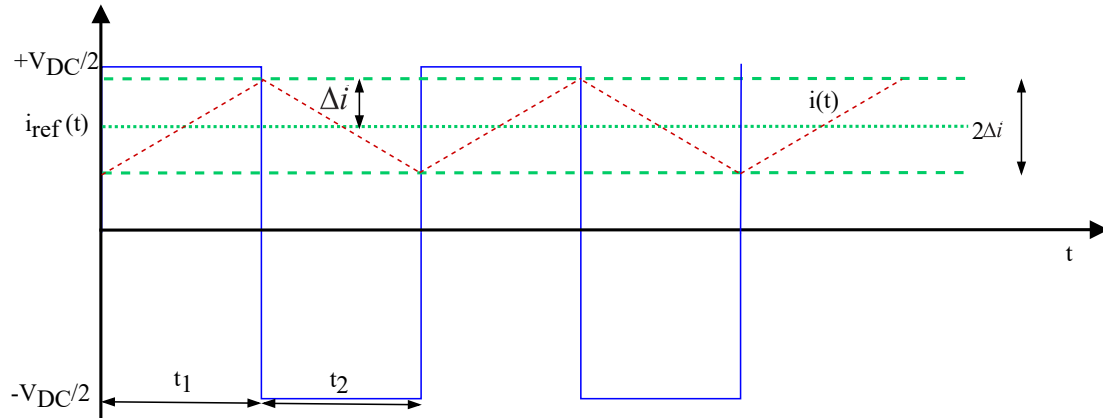


Figure 2.2.3: Theoretical waveform showing hysteresis band current control where actual current $i(t)$ is compared with the reference current $i_{ref}(t)$ and $2\Delta i$ is the hysteresis bandwidth.

It can be observed that the switching frequency f_{sw} in hysteresis current control is determined by how quickly the current changes from $+\Delta i$ to $-\Delta i$ and vice-versa. This is influenced by the input DC link voltage, back emf and the phase inductance [22]. In hysteresis control, switching frequency changes with the current rather than remaining constant and can be calculated as

$$f_{sw} = \frac{1}{t_1 + t_2}. \quad (2.2.5)$$

where:

- t_1 is the turn-on period of the top switch,
- t_2 is the turn-off period of the top switch.

2.3 Losses in HSI

The main losses in the inverter are due to power losses in the switches and the free-wheeling diodes. The total power losses consists of switching losses and the conduction losses. Switching characteristics of the MOSFET is required to understand how to calculate these losses.

Figure 2.3.1 shows the simplified turn on-off characteristics in the phase leg for phase a in the three-phase HSI. The figure is valid for the positive output current and for the negative current it is instead the top diode D_1 that will be conducting for a short period of time. Initially the top switch S_1 is conducting and at t_1 it is turned off. The bottom diode D_2 will not start to conduct until it is forward biased. This means that the the voltage V_{S1} starts increasing and the voltage V_{S2} decreases.

When the voltage V_{S2} reaches zero the diode D_2 starts to conduct and the current through it increases. During the transition there is both a voltage across and current flows through the switch S_1 which generates turn-off switching losses. Conduction losses occurs during the current conduction of the switches and the diodes. At t_6 after the blanking time the switch S_1 starts to conduct but the diode D_2 will not stop to conduct until the current reaches zero. This means the current i_{S1} increases and the the current i_{S2} decreases. At t_7 when the current flowing through the diode D_2 reaches negative value, due to the reverse recovery, the diode D_2 starts to block and the voltage V_{S1} decreases. When V_{S1} is zero the transition is over and the switch S_1 gets turned on. During this transition there will be turn-on switching losses in the switch S_1 and reverse recovery losses in the diode D_2 .

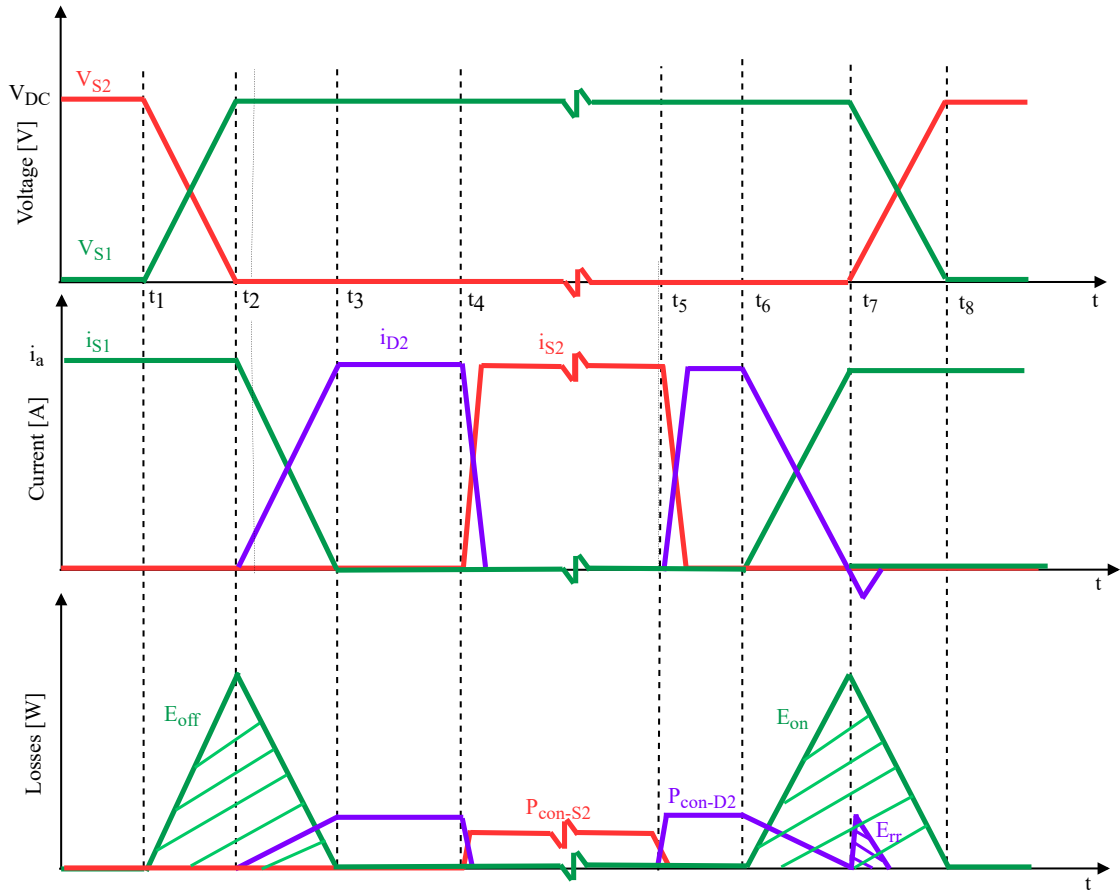


Figure 2.3.1: Theoretical waveform showing simplified turn on-off characteristics in the phase leg for phase a in the three-phase HSI. The highlighted area in the bottom plot represents the switching energies.

The average total losses in the HSI can be expressed as

$$P_{\text{tot-HSI}} = 6(P_{\text{MOSFET-sw}} + P_{\text{MOSFET-con}} + P_{\text{Diode-sw}} + P_{\text{Diode-con}}). \quad (2.3.1)$$

where

$P_{sw-MOSFET}$ is the average value of switching losses in one of the six MOSFETs,
 $P_{cond-MOSFET}$ is the average value of conduction losses in one of the six MOSFETs,
 $P_{sw-Diode}$ is the average value of switching losses in one of the six Diodes,
 $P_{cond-Diode}$ is the average value of conduction losses in one of the six Diodes.

2.3.1 Switching losses

Switching losses occurs during the transition from on state into off state and vice-versa due to presence of voltage across and current through the switch, as can be seen in the Figure 2.3.1. The average switching losses are calculated as [23]

$$P_{MOSFET-sw} = \frac{\sum_{i=1}^{n=t_f f_{sw}} (E_{on,i}(V_{DC}, i_x, T_j) + E_{off,i}(V_{DC}, i_x, T_j) + E_{rr,i}(V_{DC}, i_x, T_j))}{t_f} \quad (2.3.2)$$

where:

V_{DC} is the DC link voltage,
 i_x is the phase current for the switch,
 T_j is the MOSFET junction temperature,
 E_{on} is the energy losses during turn-on of the MOSFET,
 E_{off} is the energy losses during turn-off of the MOSFET,
 E_{rr} is the reverse recovery energy losses of the free-wheeling diode,
 t_f is the fundamental period,
 f_{sw} is the switching frequency.

The switching energies are depending on the voltage across the switch, current through it and the temperature of the junction. The values and these variations can be taken from the data sheet of the switch. The switching losses in the MOSFET and the diode can be modeled as [24]

$$E_{on} = E_{on,ref} \left(\frac{V_{DC}}{V_{ref}} \right)^{K_{v,on}} \left(\frac{1}{\pi} \frac{i_x}{I_{ref}} \right)^{K_{i,on}} (1 + TC_{on} (T_j - T_{j,ref})) \quad (2.3.3)$$

$$E_{off} = E_{off,ref} \left(\frac{V_{DC}}{V_{ref}} \right)^{K_{v,off}} \left(\frac{1}{\pi} \frac{i_x}{I_{ref}} \right)^{K_{i,off}} (1 + TC_{off} (T_j - T_{j,ref})) \quad (2.3.4)$$

$$E_{rr} = E_{rr,ref} \left(\frac{V_{DC}}{V_{ref}} \right)^{K_{v,rr}} \left(\frac{1}{\pi} \frac{i_x}{I_{ref}} \right)^{K_{i,rr}} (1 + TC_{rr} (T_j - T_{j,ref})). \quad (2.3.5)$$

where:

V_{ref}, I_{ref} are the values from the datasheet at which switching energy is calculated,
 $k_{i,on,off,rr}$ are the exponents for the current, can be obtained in the datasheet,
 $k_{v,on,off,rr}$ are the exponents for the voltage, can be obtained in the datasheet,
 $TC_{E,on,off}, TC_{E,rr}$ are the temperature coefficients.

2.3.2 Conduction losses

The losses that occur during the static operation of switches are classified as conduction losses. The conduction of current through the switch and the free wheeling-diode causes these losses. The average value of the conduction losses over one switching period in the MOSFET can be obtained by integrating the instantaneous power losses over the switching cycle [25][26]

$$\begin{aligned} P_{\text{con-MOSFET}} &= \frac{1}{t_{sw}} \int_0^{t_{sw}} v(t)i(t)dt \\ &= \frac{1}{t_{sw}} \int_0^{t_{sw}} R_{on}i^2(t)dt. \end{aligned} \quad (2.3.6)$$

where:

$v(t)$ is the instantaneous voltage across the MOSFET when it is conducting ,
 $i(t)$ is the instantaneous current flowing through the MOSFET,
 R_{on} is the drain-source on state resistance of the MOSFET.

The average conduction losses during one fundamental period can be calculated as

$$P_{\text{MOSFET-con}} = \frac{1}{t_f} \int_0^{t_1} v(t)i(t)dt. \quad (2.3.7)$$

The free-wheeling diode conduction losses can be calculated using a diode approximation with a series DC voltage source and on-state resistance. The average conduction losses of the diode over one switching period can be obtained as

$$\begin{aligned} P_{\text{con-Diode}} &= \frac{1}{t_{sw}} \int_0^{t_{sw}} v_d(t)i_d(t)dt \\ &= \frac{1}{t_{sw}} \int_0^{t_{sw}} (V_d i(t) + R_d i^2(t))dt. \end{aligned} \quad (2.3.8)$$

where:

V_d is the on-state voltage of the diode at zero current,
 $v_d(t)$ is the instantaneous voltage across the diode when it is conducting,
 $i_D(t)$ is the instantaneous current flowing through the diode,
 R_d is the on-state resistance of the diode.

The average conduction losses of the diode over one fundamental period can be obtained as

$$P_{\text{Diode-con}} = \frac{1}{t_f} \int_0^{t_1} v_d(t)i_d(t)dt. \quad (2.3.9)$$

2.4 Thermal model of the Switch

The switching losses and conduction losses generate heat and as a result temperature of the switch increases. To evaluate the thermal behaviour of the switch, the equivalent Cauer model of one of the MOSFET modules used in this project is presented in Figure 2.4.1.[27]

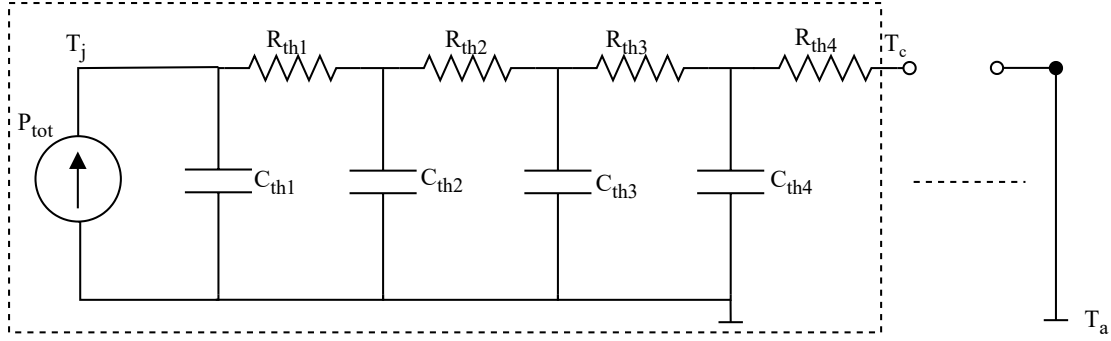


Figure 2.4.1: Equivalent circuit showing the thermal description of one of the MOSFET modules.

The MOSFET module junction temperature T_j can be estimated as

$$T_j = Z_{th1-4} P_{tot} + T_a \quad (2.4.1)$$

where:

- Z_{th1-4} are the 4 RC thermal impedance elements of one MOSFET module,
- P_{tot} is the total losses in one MOSFET module,
- T_a is the ambient temperature.

2.5 Total Harmonic Distortion (THD)

THD is defined as the ratio of the equivalent rms voltage or current of all the harmonic frequencies (from the 2nd harmonic on) over the rms voltage or current of the fundamental frequency f_f . In this project, the THD of the load current is calculated using

$$\text{THD} = \sqrt{\frac{\sum_{v \geq 2} I_v^2}{I_1^2}} = \sqrt{\frac{I_{\text{rms}}^2 - I_0^2 - I_1^2}{I_1^2}}. \quad (2.5.1)$$

where I_v is the rms current of the v^{th} harmonic, and I_{rms} is its overall rms current.

3

Active Clamped Resonant DC Link Inverter

This chapter introduces the first soft switching topology the ACRDCLI. In the first section, detailed description of the three-phase ACRDCLI is introduced. To understand the working principle of this topology different modes of operation under no load condition is explained using it's voltage and current waveforms. Finally, the total loss equations are presented and the additional component losses are calculated.

3.1 Three-phase ACRDCLI

The circuit schematic for the three-phase ACRDCLI is shown in Figure 3.1.1. The theory explained in this chapter is referred from the thesis [28] [29]. An auxiliary circuit is added to the DC link of the three-phase HSI. The auxiliary circuit consists of a resonant circuit and a clamp circuit. The inductor L_r and capacitor C_r forms the resonant circuit which creates the resonant operation in the DC link and the resonant frequency is calculated as

$$f_r = \frac{1}{2\pi\sqrt{L_r C_r}}. \quad (3.1.1)$$

The voltage across the resonant capacitor C_r is referred to as the resonant DC link voltage V_{Cr} . To achieve low switching losses, the inverter main switches are synchronized to the zero crossings of the V_{Cr} . The clamp circuit utilises a clamp capacitor C_c and a clamp switch S_c with a free-wheeling diode D_c . The resonant DC link voltage V_{Cr} is limited to the clamping voltage and is expressed as $V_{DC} + V_{Cc}$.

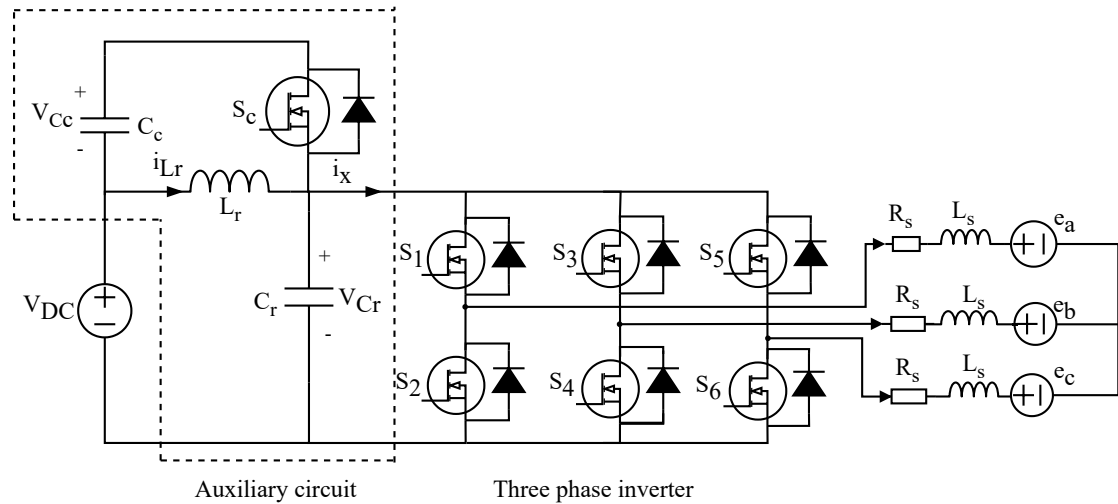


Figure 3.1.1: The three-phase ACRDCLI comprizing of the auxiliary circuit connected to the battery, the DC voltage source and the six MOSFETs, S_1 to S_6 , and to the PMSM modeled as an RL-circuit and a voltage source.

3.2 ACRDCLI equivalent circuit

To understand the working principle of the three-phase ACRDCLI, Figure 3.1.1 is simplified into an equivalent circuit for load operation as shown in Figure 3.2.1. The main switch S_m represents the six main switches of the three-phase ACRDCLI and a constant current source I_x used to represent the DC link current i_x . When the switch S_m in Figure 3.2.1 is 1, it represents the six main switches of the three-phase ACRDCLI are on. When the switch S_m is zero, six main switches of the three-phase ACRDCLI are turned on or off according to the reference inductor current. The principle of operation of the ACRDCLI can be divided into four states (State 1 to State 4) which will be explained in this section using the voltage and current waveforms, shown in Figure 3.2.2 of the circuit in Figure 3.2.1

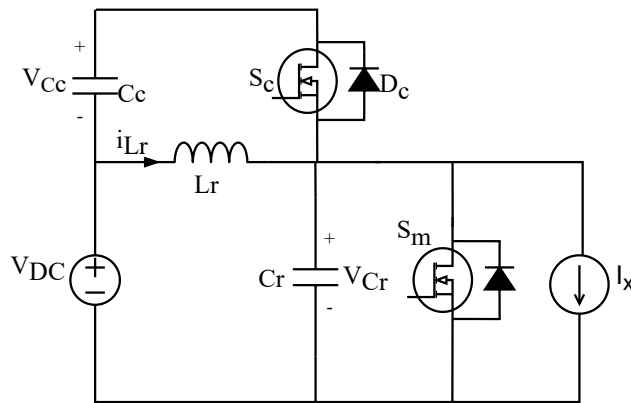


Figure 3.2.1: Equivalent circuit of the ACRDCLI under load operation.

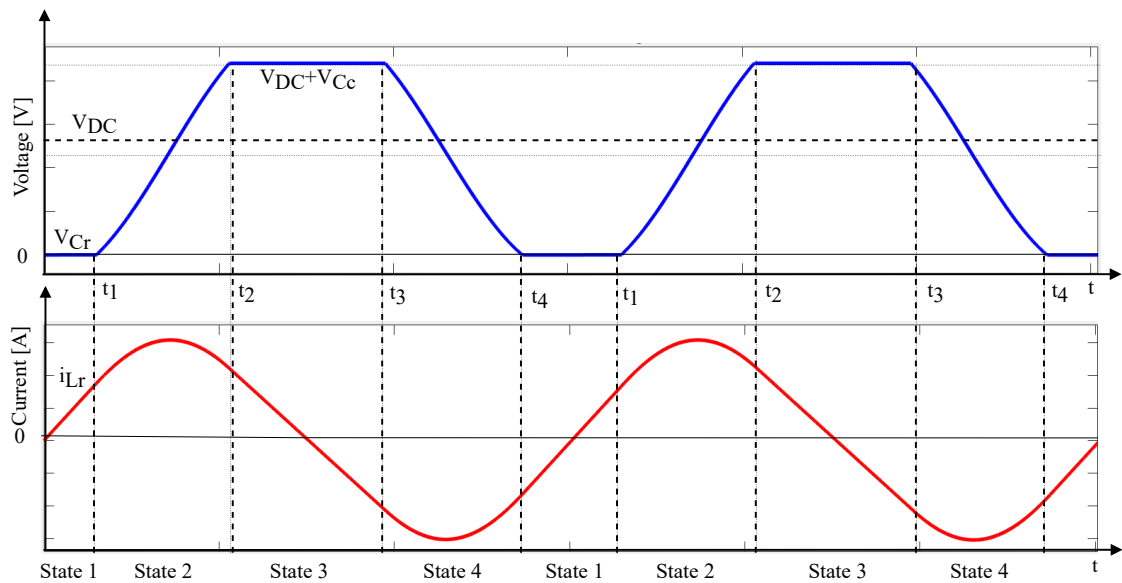


Figure 3.2.2: Simulated waveforms of the ACRDCLI showing the resonant DC link voltage V_{Cr} and the resonant inductor current i_{Lr} illustrating four operating states.

State 1:

The start of circuit operation begins by turning on the switch S_m when the voltage V_{Cr} is zero and this creates a short circuit of the DC link bus as can be seen in Figure 3.2.3.

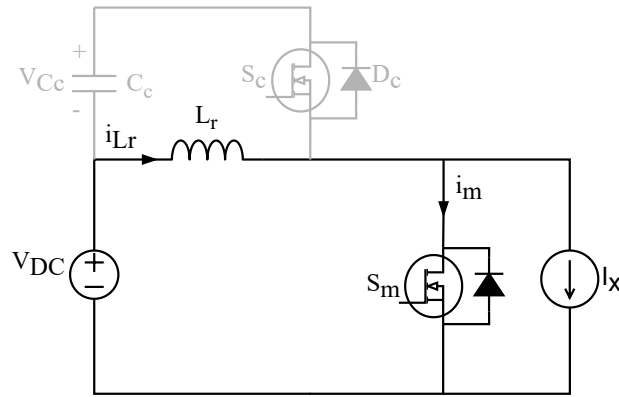


Figure 3.2.3: Circuit during the boost period before $t_1 < 0$, where S_m is on and S_c is off.

The resonant inductor L_r charges through the main switch S_m and the resonant inductor current i_{Lr} starts increasing linearly. During this state, the resonant DC link voltage V_{Cr} is zero and S_m turns on and turns off under Zero Voltage Switching (ZVS) conditions. The short circuit is released after enough energy is stored in L_r . State 1 changes to State 2 when i_{Lr} reaches the required reference resonant inductor current i_{Lr}^* and it is expressed as [30]

$$i_{Lr}^* = I_x + I_{Lr}(min). \quad (3.2.1)$$

where:

I_x is the inverter DC current,

$I_{Lr}(min)$ is the minimum current required to turn off the S_m and to overcome losses.

For the three-phase ACRDCLI the reference inductor current i_{Lr}^* calculation for the next switching cycle is explained in Section 5.3.1. This is required to ensure that a proper reference current is applied to L_r at the starting of each resonant cycle.

State 2:

This state starts when the switch S_m is turned off and the $L_r C_r$ resonant operation occurs. At the start of State 2, the energy stored in the L_r is given as

$$E = \frac{1}{2} L_r i_{Lr}^{*2}. \quad (3.2.2)$$

In Figure 3.2.4, the current flowing through L_r is transferred to C_r . The voltage V_{Cr} starts rising and reaches the clamping voltage $V_{DC} + V_{Cc}$ in the end of State 2.

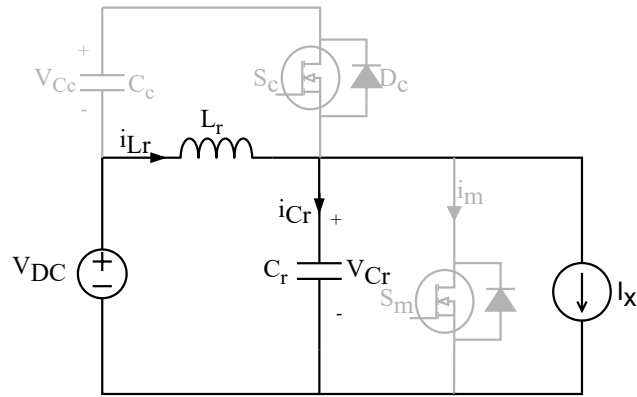


Figure 3.2.4: Circuit during pre-charge transition between t_1 to t_2 , where the S_m is off and the S_c is off.

State 3:

After reaching the $V_{DC} + V_{C_c}$, the clamp diode D_c starts conducting and clamps the resonant DC link voltage V_{C_r} . At the same time the switch S_c turns on and the clamp current i_{C_c} transfers to the S_c as shown in Figure 3.2.5. The i_{L_r} linearly decreases as the voltage across the L_r is negative. This state ends when the total charge flowing through the clamp capacitor C_c becomes zero and then the S_c is turned off.

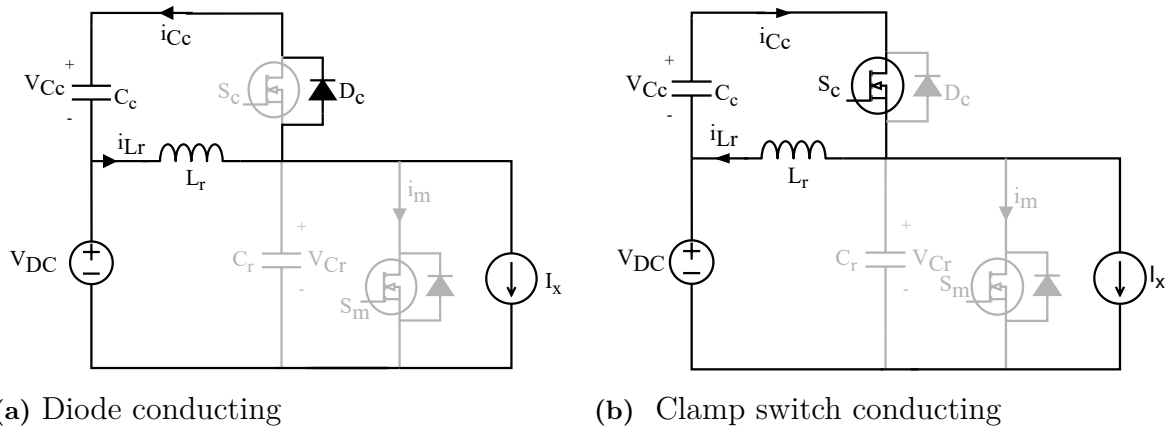


Figure 3.2.5: Circuits during clamping period between t_2 to t_3 where the S_m is off and the S_c is on.

State 4:

State 4 starts when the switch S_c is turned off and again resonance operation takes place. It can be seen from Figure 3.2.2 when the voltage V_{C_r} starts decreasing. This mode ends when the V_{C_r} approaches zero, it will be clamped by the free-wheeling diode of the main switch and a new resonating operation will begin (start of State 1).

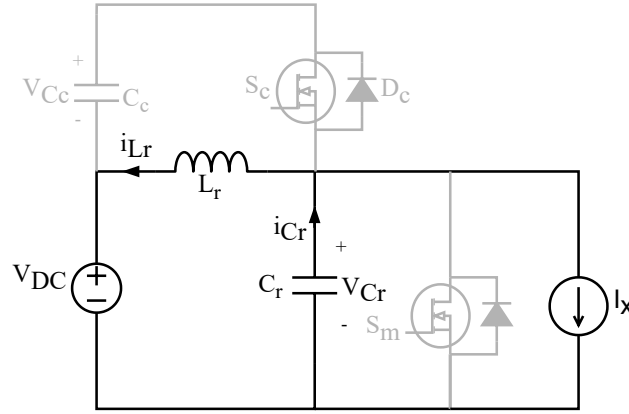


Figure 3.2.6: Circuit during the discharge transition period between t_3 to t_4 , where S_m is off and S_c is off.

3.3 Losses in ACRDCLI

In the ACRDCLI, the total losses include losses in the main switches and losses in the auxiliary circuit. The additional losses are clamp switch losses, Equivalent Series Resistance (ESR) losses of the clamp capacitor, the resonant capacitor and the inductor losses are calculated as

$$P_{\text{tot-ACRDCLI}} = P_{\text{tot-HSI}} + P_{\text{Clamp}} + P_{Cr} + P_{Cc} + P_{Lr}. \quad (3.3.1)$$

where:

- $P_{\text{tot-HSI}}$ is the average value of total losses in the six main switches,
- P_{Clamp} is the average value of total losses in the clamp switch,
- P_{Cr} is the total losses in the resonant capacitor,
- P_{Cc} is the total losses in clamp capacitor,
- P_{Lr} is the total losses in the resonant inductor.

The three-phase ACRDCLI operates under the same conditions as the three-phase HSI. So the total Power losses calculations explained in Section 2.3 will be used for the six main switches in the ACRDCLI. The main switches are turned on and off at ZVS condition, switching losses will not be considered. The conduction losses calculations are similar to the three-phase HSI as the conducting current through and the voltage across the switch is same. The total average losses in the six main switches can be re-expressed as

$$P_{\text{tot-HSI}} = 6(P_{\text{MOSFET-con}} + P_{\text{Diode-con}}). \quad (3.3.2)$$

where

- $P_{\text{MOSFET-cond}}$ is the average value of conduction losses in one of the six MOSFETs,
- $P_{\text{Diode-cond}}$ is the average value of conduction losses in one of the six Diodes.

Due to additional components there are extra losses which will be explained in the following sections.

3.3.1 Clamp Switch Losses

In the auxiliary circuit, one extra switch is used to clamp the resonant DC link voltage and has the same rating as the main switch. The clamp switch is turned on and off under Zero Current Conditions (ZCS). This means the switching losses are not considered in the equations. Hence, the losses of the clamp switch include conduction losses of the MOSFET and the diode can be seen as

$$P_{\text{Clamp}} = (P_{\text{MOSFET-con}} + P_{\text{Diode-con}}). \quad (3.3.3)$$

where:

$P_{\text{MOSFET-con}}$ is the average value of conduction losses in the clamp MOSFET,
 $P_{\text{Diode-con}}$ is the average value of conduction losses in in the clamp Diode.

3.3.2 ESR Losses

In the ACRDCLI as the current circulates in the auxiliary circuit, losses occur in the Equivalent Series Resistance ESR of the resonant capacitor C_r and the clamp capacitor C_c . The capacitor equivalent circuit is shown in Figure 3.3.1, the sum of the inductive elements including the leads, a high-resistance DC path (R_p) in parallel with the capacitance, and the series resistance combined into a single element.

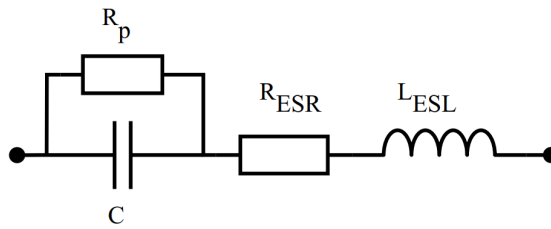


Figure 3.3.1: Capacitor Equivalent Circuit

For the ESR it is frequency-dependent, temperature-dependent, and changes as components age. It is usually an important consideration in selecting the capacitors. In this project, only capacitance, ESR and its losses are considered and ESR is assumed as a resistor with a constant resistance, other components in the capacitor equivalent circuit will be neglected.

For the ESR components of the clamp capacitor and the resonant capacitor in the ACRDCLI, losses are obtained as

$$\begin{aligned}
 P_{\text{ESR}} &= P_{C_r} + P_{C_c} \\
 &= R_{C_r} i_{C_r-rms}^2 + R_{C_c} i_{C_c-rms}^2.
 \end{aligned} \tag{3.3.4}$$

where:

- R_{C_r} is the ESR value of the resonant capacitor,
- R_{C_c} is the ESR value of the clamp capacitor,
- i_{C_r-rms} is the rms current flowing through the resonant capacitor,
- i_{C_c-rms} is the rms current flowing through the clamp capacitor.

3.3.3 Resonant Inductor Losses

The resonant inductor L_r carries the resonant inductor current i_{L_r} , inverter DC current i_x and increases the overall losses of the ACRDCLI. To derive a simple expression for the inductor losses, the ESR value of L_r is calculated using quality factor Q [31], can be seen as

$$R_{L_r} = \frac{X_{L_r}}{Q}. \tag{3.3.5}$$

where:

- X_{L_r} is the reactance of the resonant inductor at a resonant frequency,
- Q is the quality factor of the resonant inductor .

The losses in the resonant inductor are calculated as

$$P_{L_r} = R_{L_r} i_{L_r-rms}^2. \tag{3.3.6}$$

where i_{L_r-rms} is the rms current flowing through the resonant inductor.

4

Auxiliary Resonant Commutated Pole Inverter

This chapter explains the theoretical knowledge required for an Auxiliary Resonant Pole Commutated Inverter (ARCPI). The working principle of this topology is explained using a single-phase ARCPI circuit with its voltage, current and PWM signal waveforms. In the last section, total losses calculations are shown.

4.1 Three-phase ARCPI

The ARCPI is a load-side Resonant Transition Inverter (RTI) type soft switching topology which can be seen in Figure 4.1.1. The auxiliary circuit is added to the three-phase HSI. The auxiliary circuit consists of the independently controlled circuits for three phases with the six auxiliary switches, A_1 to A_6 in series with the three resonant inductors, L_{ra} to L_{rc} . The six resonant capacitors, C_{r1} to C_{r6} are connected in parallel to each of the main switches.

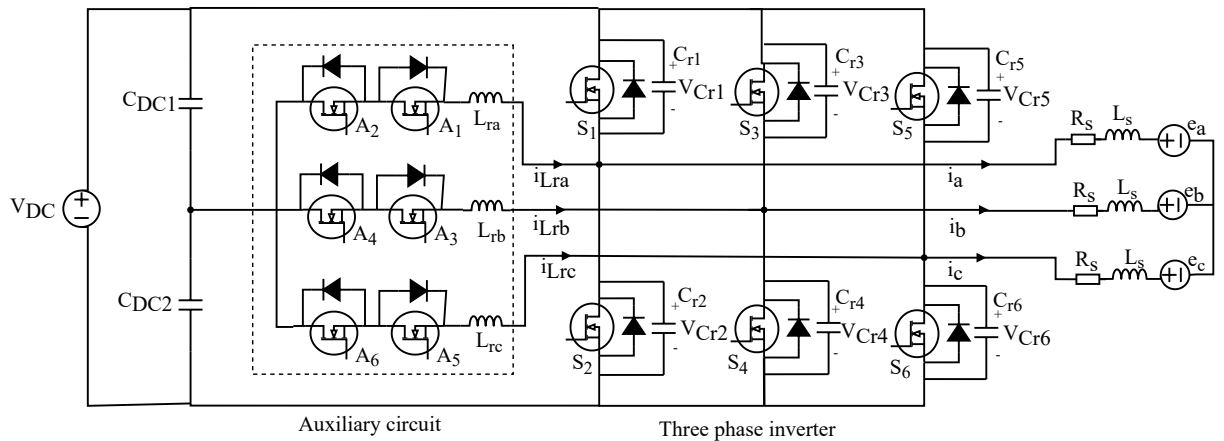


Figure 4.1.1: The three-phase ARCPI comprising of the auxiliary circuit connected to the battery, the DC voltage source and six MOSFETS, S_1 to S_6 and to the PMSM modeled as an RL-circuit and a voltage source.

4.2 Single-phase ARCPI Circuit

In this section the single-phase ARCPI circuit will be analysed to understand the working principle of the three-phase circuit. Figure 4.2.1 shows the circuit diagram of the single-phase ARCPI. The circuit consists of two main switches S_1 and S_2 and an auxiliary circuit. The resonant capacitors, C_{r1} , C_{r2} are connected parallel to the switches and they hold the DC link voltage during turn on and off of the switches. This enables the zero voltage switching (ZVS) when the switch is being turned on and off, which eliminates the switching losses in the main switches. The resonant inductor L_r is connected in series with the auxiliary switches A_1 and A_2 and they operate under the Zero Current Switching (ZCS). The detailed description of the single-phase ARCPI can be found in [32].

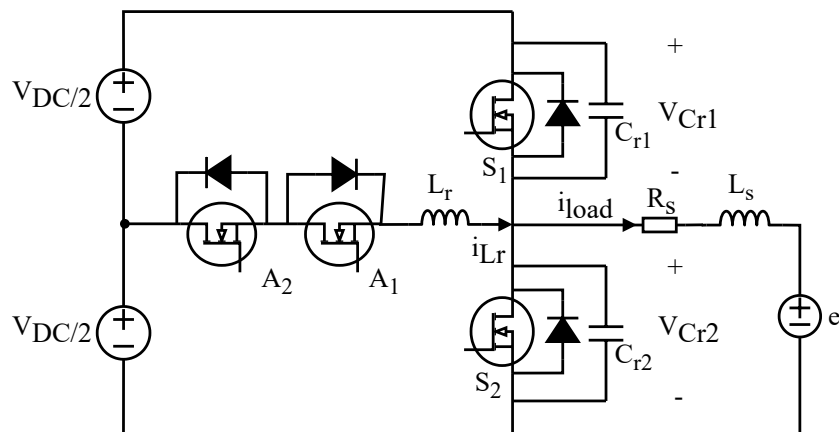


Figure 4.2.1: The single-phase ARCPI circuit.

In this section, the circuit will be explained only for the positive load current under six different states using the voltage, current and the control signal waveforms as shown in Figure 4.2.2 and Figure 4.2.9. When the load current is negative, the principle will be the opposite. Different operating states and their working principle is explained in [33].

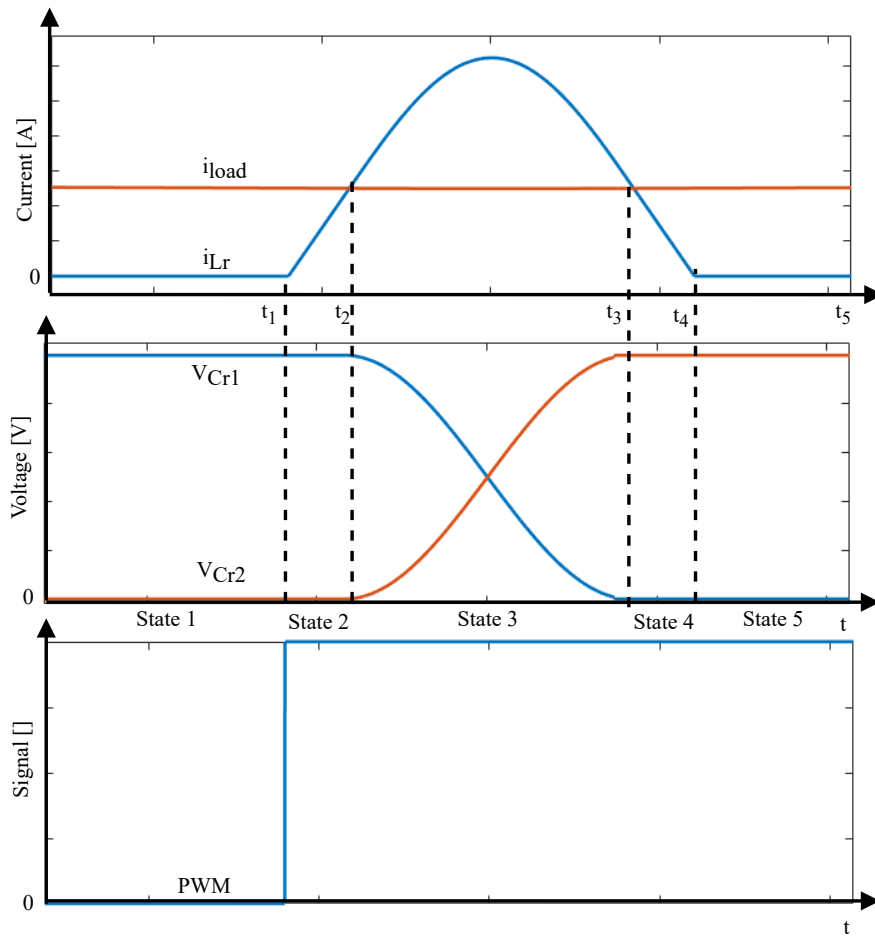


Figure 4.2.2: Simulated waveforms of the single-phase ARCPI circuit showing the load current i_{load} , the resonant inductor current i_{Lr} , the voltages across the top and bottom switches V_{Cr1} , V_{Cr2} showing State 1 to State 5 operation with respect to the PWM control signal.

State 1:

As seen in Figure 4.2.2 and Figure 4.2.3 the bottom switch S_2 is conducting during state 1. In this state, the transition to move the load from the bottom switch S_2 to the top switch S_1 is started. When the switch S_2 is conducting, the voltage across the resonant capacitor V_{Cr1} is equal to DC link voltage V_{DC} . In this state, the auxiliary circuit is not used and the resonant inductor current i_{Lr} is zero, which can be seen in Figure 4.2.2.

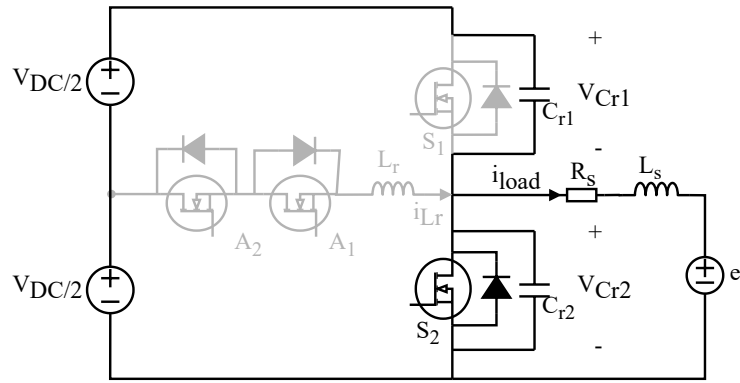


Figure 4.2.3: The single-phase ARCPI during State 1, free-wheeling operation where S_2 is on and A_1 , A_2 and S_1 are off.

State 2:

This state is triggered by the control signal. When the PWM control signal changes from 0 to 1 (low to high), the auxiliary switch A_2 is turned on, as is shown in Figure 4.2.4. The voltage across the resonant inductor L_r is half of the DC link voltage, $V_{DC}/2$. During this period the resonant inductor current i_{Lr} increases as,

$$i_{Lr} = \frac{V_{DC}}{2} \frac{(t - t_1)}{L_r}. \quad (4.2.1)$$

where:

- t_1 is the starting time for State 2,
- t is the time,

This state ends, when the current i_{Lr} is equal to the load current i_{load} and the switch S_2 is turned off.

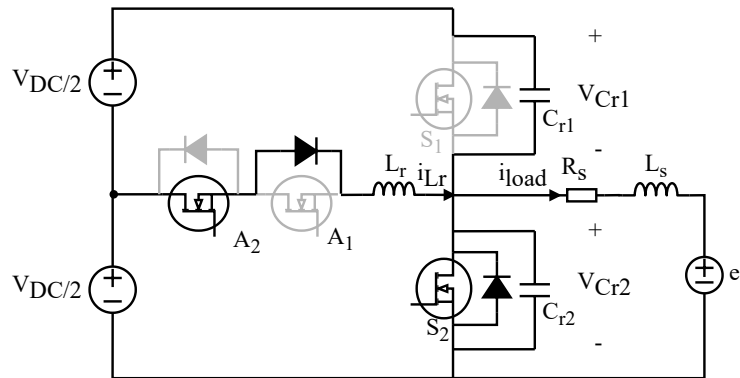


Figure 4.2.4: The single-phase ARCPI State 2, pre-charge of the resonant inductor with the load current where S_2 , A_2 are on and S_1 , A_1 are off.

State 3:

It can be seen in the Figure 4.2.2, the current i_{Lr} increases above the load current

i_{load} . When the bottom switch S_2 is turned off, the current that exceeds the i_{load} charges the resonant capacitors $C_{r1} + C_{r2}$ as is shown in Figure 4.2.5. At t_2 , the voltage V_{Cr2} starts increasing from 0 V. The current i_{Lr} keeps increasing until V_{Cr2} is equal to $V_{DC}/2$. When the voltage across the resonant inductor L_r turns negative, the current i_{Lr} start to decrease. The resonant frequency during this time is expressed as

$$f_r = \frac{1}{2\pi\sqrt{L_r(C_{r1} + C_{r2})}}. \quad (4.2.2)$$

When the resonant capacitor voltage V_{Cr1} approaches zero level, the top switch S_1 is turned on and State 3 changes to State 4.

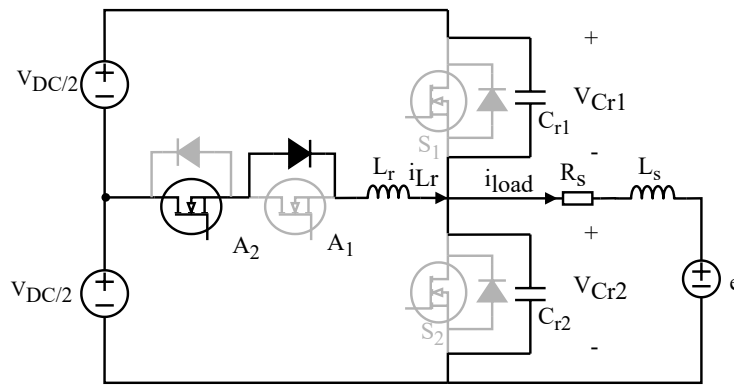


Figure 4.2.5: The single-phase ARCPI State 3, resonant operation where A_2 is on and S_1 , S_2 and A_1 are off.

State 4:

As is shown in Figure 4.2.6 when the top switch S_1 is turned on, the voltage across the resonant capacitor C_{r1} remains zero. During this state, the current i_{Lr} keeps decreasing to zero and the auxiliary switch A_2 is turned off. When the switch A_2 is off, the current flowing through auxiliary circuit is zero, hence there are no switching losses in the switch A_2 .

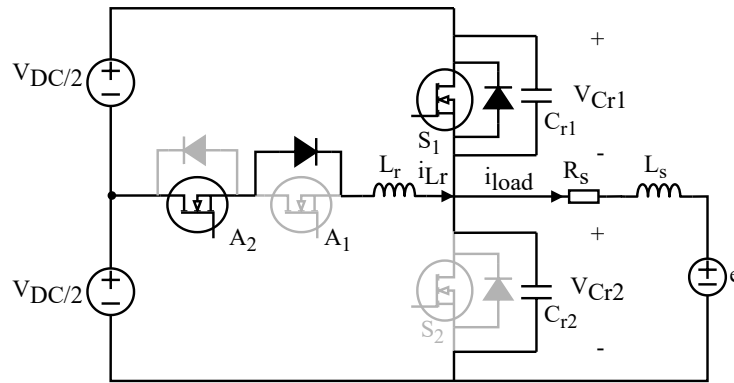


Figure 4.2.6: The single-phase ARCPI State 4, discharge of resonant inductor where S_1 , A_2 are on and S_2 , A_1 are off.

State 5:

In Figure 4.2.7, the switch S_1 is conducting and the auxiliary circuit is turned off. With minimal switching losses, the transition from S_2 to S_1 is completed in State 5. The circuit remains in this state as long as the PWM control signal is 1 (high).

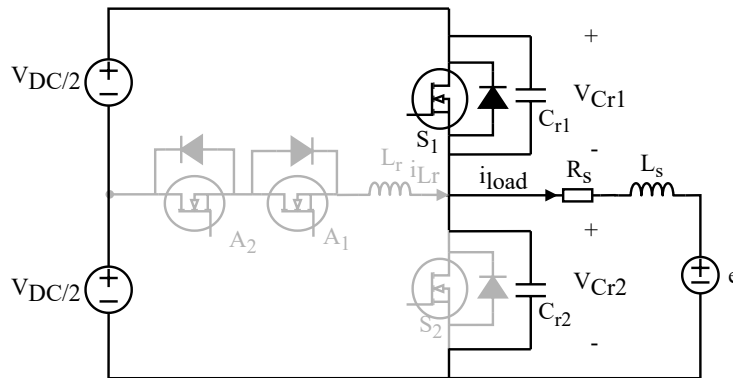


Figure 4.2.7: The single-phase ARCPI State 5, with completion of transition where S_1 is on and S_2 , A_1 , A_2 are off.

State 6:

This state is entered when the PWM control signal changes from 1 to 0 (high to low) and then the switch S_1 is turned off as shown in Figure 4.2.8. In this state the voltage across the top switch V_{Cr1} increases and bottom switch V_{Cr2} decreases as shown in 4.2.9. During this state, the load current i_{load} charges the resonant capacitor C_{r1} until the top switch voltage V_{Cr1} becomes V_{DC} . Similarly, the bottom switch voltage V_{Cr2} reaches zero when C_{r2} is fully discharged and at this point the switch S_2 is turned on and State 6 is ended. The circuit then enters State 1 and the transition from S_1 to S_2 is completed with minimum switching losses and without using the auxiliary circuit. The rate of the capacitor voltage is controlled by $C_{r1} + C_{r2}$. The rise and fall time during this period is given as [34]

$$t_{rise} = t_{fall} = \frac{2(C_{r1} + C_{r2})V_{DC}}{i_{load}}. \quad (4.2.3)$$

It can be seen from (4.2.3) when the load current i_{load} is small, the longer this period becomes. To obtain low switching times the switches can be turned off by hard-switching or by using the auxiliary switches for these cases with a low load current..

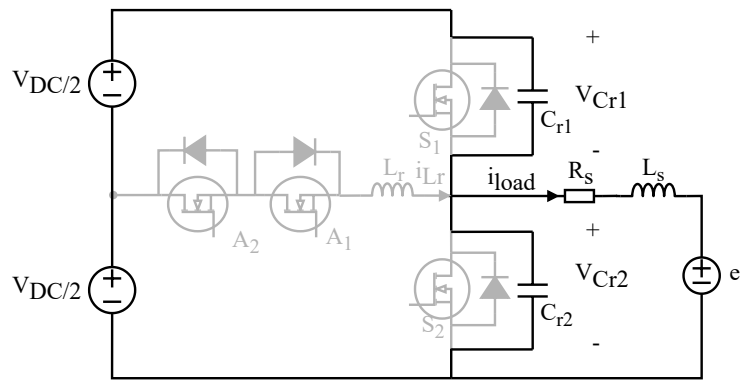


Figure 4.2.8: The single-phase ARCPI State 6, where S_1 , S_2 , A_1 and A_2 are turned off.

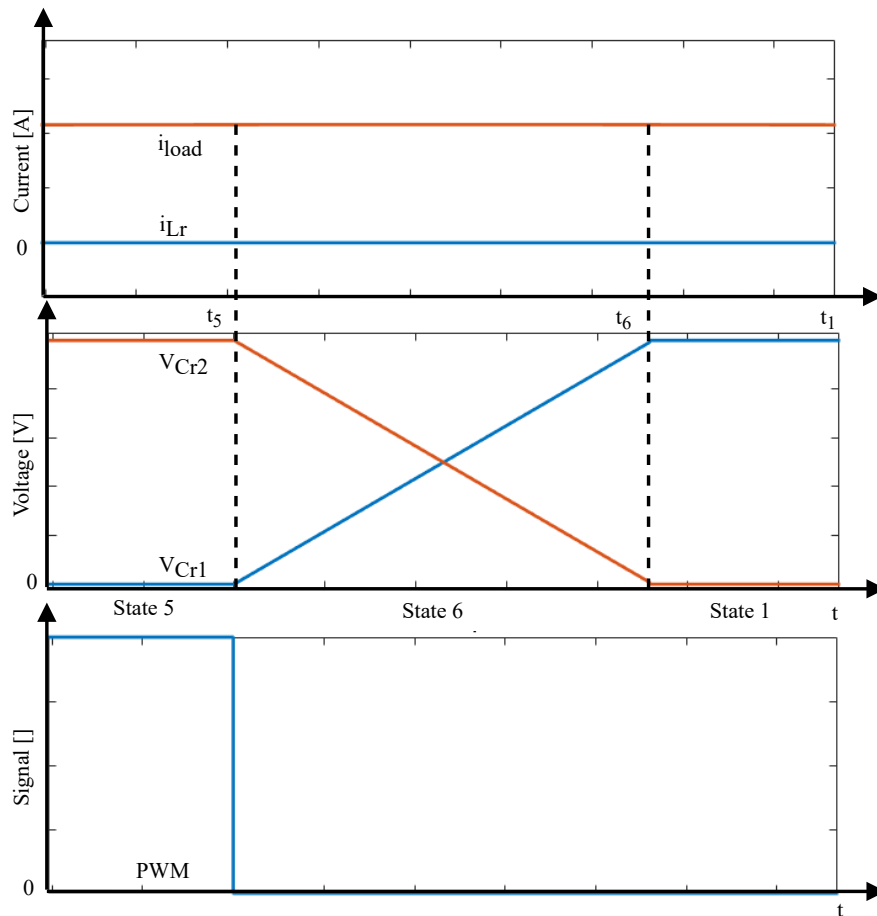


Figure 4.2.9: Simulated waveforms of the single-phase ARCPI circuit showing the load current i_{load} , the resonant inductor current i_{Lr} , the voltages across the top and the bottom switches V_{Cr1} , V_{Cr2} showing State 6 with respect to PWM control signal

4.3 Losses in ARCPI

The total losses in the ARCPI are calculated similarly compared to the ACRDCLI. The total losses can be calculated as:

$$P_{\text{tot-ARCPI}} = P_{\text{tot-HSI}} + 6P_{\text{Aux}} + 6P_{\text{Cr}} + 3P_{\text{Lr}} \quad (4.3.1)$$

where:

- $P_{\text{tot-HSI}}$ is the average value of total power losses in the six main switches,
- P_{Aux} is the average value of total power losses in the auxiliary switches,
- P_{Cr} is the total losses in the resonant capacitors,
- P_{Lr} is the total losses in the resonant inductors.

As the ARCPI works under the same conditions as the HSI and the ACRDCLI. The total power losses equations for the six main switches can be found in Section 2.3 and Section 5.2.3. The additional loss equations due to the auxiliary circuit are explained in the following sections.

4.3.1 Auxiliary Switch losses

The auxiliary switches are used to change the load from the bottom main switch to the top main switch and vice-versa to ensure minimum turn-on voltage. The auxiliary switches are turned on and off under Zero Current Switching (ZCS) conditions, hence the switching losses are negligible. There are six auxiliary switches in the ARCPI and the power losses consist of conduction losses in the MOSFET and the diode. These losses are calculated with (2.3.7) and (2.3.9)

$$P_{\text{Aux}} = 6(P_{\text{MOSFET-con}} + P_{\text{Diode-con}}). \quad (4.3.2)$$

where:

- $P_{\text{MOSFET-cond}}$ is the average value of conduction losses in the auxiliary MOSFET,
- $P_{\text{Diode-cond}}$ is the average value of conduction losses in in the auxiliary diode.

4.3.2 ESR losses

In the ARCPI, the six resonant capacitors are connected in parallel to each of the six main switches. Detailed ESR losses with capacitor equivalent circuit is explained in Section 3.3.2. The ESR loss equation of this component can be calculated as

$$P_{\text{ESR}} = 6R_{\text{Cr}}i_{\text{Cr-rms}}^2. \quad (4.3.3)$$

where:

R_{Cr} is the ESR value of the resonant capacitor,
 i_{Cr-rms} is the rms current flowing through the six resonant capacitor,

4.3.3 Resonant Inductor losses

As explained in Section 3.3.3, the losses of the three resonant inductors in the ARCPI are calculated by estimating the ESR value using quality factor Q and by finding the rms current flowing through it. The total losses can be calculated as

$$P_{Lr} = 3R_{Lr}i_{Lr-rms}^2. \quad (4.3.4)$$

where:

R_{Lr} is the ESR value of the resonant inductor,
 i_{Lr-rms} is the rms current flowing through the resonant inductor.

5

Case setup

The HSI and the two soft switching inverters topologies the ACRDCLI, the ARCPI are designed in PLECS and analysed in Matlab. Then each soft switching topology will be compared with the HSI using a similar control method to understand the difference in performance.

5.1 Machine Setup

To perform a fair comparison between the results of each topology, the same three-phase RLE equivalent circuit of a non-salient PMSM is applied for each simulated topology, as explained in Section 2.1. To simplify the simulation process and to analyse the performance of the motor at high load currents, R_s , L_d , L_q and ψ_m of the motor are selected based on a fixed operating point in the FEM data of the used machine. In this project, L_s is considered a constant value and it is estimated as

$$L_s = \frac{L_d + L_q}{2}. \quad (5.1.1)$$

The machine parameters based on a fixed operating point $i_d = 0$ A, $i_q = 550$ A, $\Omega_r = 3000$ RPM and $T_m = 65$ °C and the parameters are listed in Table 5.1.1.

Table 5.1.1: Machine parameters used in each simulated topologies

Description	Symbol	Value
Phase resistance	R_s [Ω]	0.1394
Phase inductance	L_s [mH]	0.1683
Magnet flux linkage	Ψ_m [Wb]	0.0904
Number of pole pairs	n_p	4
Mechanical rotor speed	Ω_r [RPM]	3000
Electrical rotor speed	ω_r [rad/s]	314.15
Machine initial temperature	T_m [°C]	65
Reference q current	i_q [A]	550
Reference d current	i_d [A]	0

5.2 HSI Setup

Figure 5.2.1 and Figure 5.2.2 show the overview of the HSI with the SVPWM control and the hysteresis current control. They use two different methods to control the

load current and later will be compared with the ARCPI and the ACRDCLI using the same control method respectively.

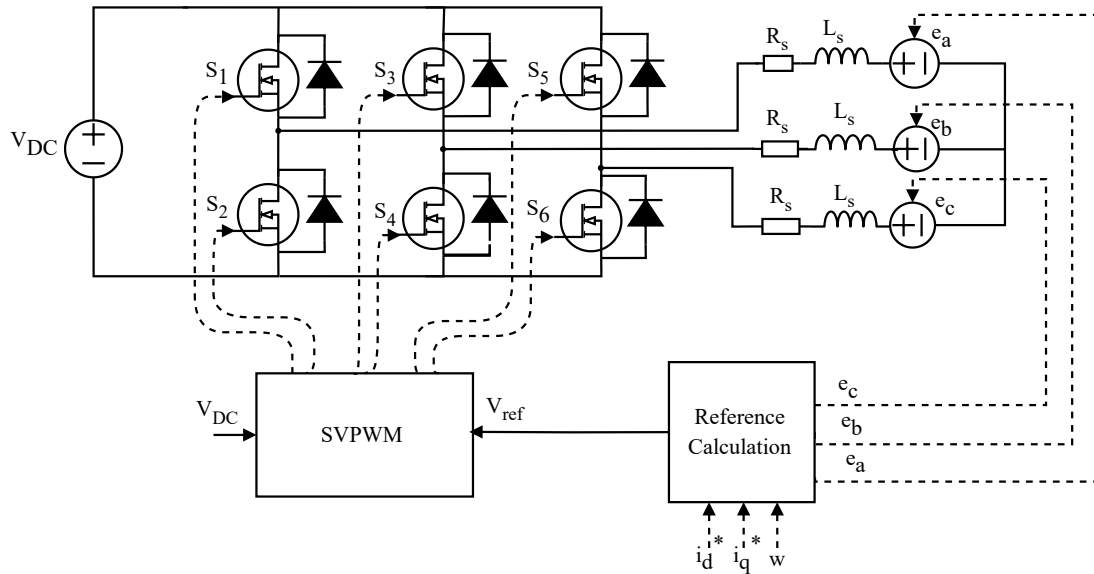


Figure 5.2.1: Overview of the three-phase HSI with the SVPWM control showing the SVPWM block and the reference calculation block.

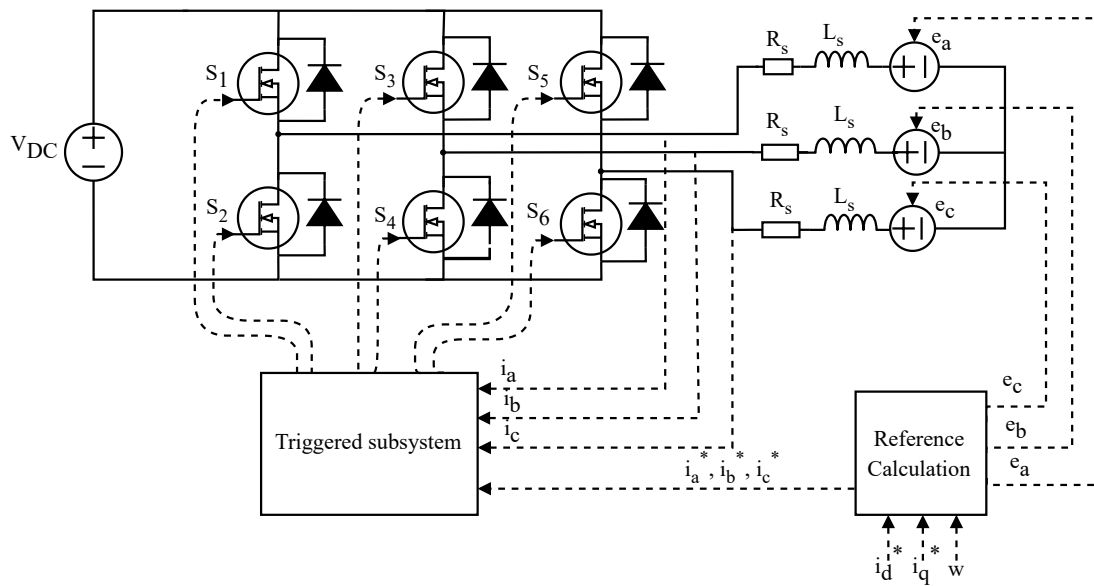


Figure 5.2.2: Overview of the three-phase HSI with the hysteresis current control showing the triggered subsystem block and the reference calculation block.

5.2.1 Reference Calculation

The reference calculation block in Figure 5.2.1 provides the reference phase voltage signals and the reference back Electromotive force (EMF) signals. The reference phase voltage V_{ref} needs to be obtained for the SVPWM, and the reference phase voltage in dq coordinates can be calculated as

$$V_{ref} = (i_d + ji_q)(R_s + jL_s\omega_r) + j\omega_r\Psi_m. \quad (5.2.1)$$

Later Park to Clarke Angle Transformation converts V_{ref} from dq coordinates to $\alpha\beta$ coordinates for SVPWM. In the project, it is assumed that the back EMF is only in the q direction. So $j\omega_r\Psi_m$ in (5.2.1) is the reference back EMF in dq coordinates. Inverse Park Transformation will be used to convert the back EMF signal from dq coordinates to abc coordinates. The three phase back EMF signals will be used on the controlled voltage source in EMF circuits to simulate the back EMF in a real machine.

The reference calculation block in Figure 5.2.2 also provides the three phase reference back EMF signals. In addition, Inverse Park Transformation converts the reference current from dq coordinates to abc coordinates. The three phase reference currents will be used for the hysteresis current control.

5.2.2 Triggered Subsystem

The triggered subsystem block in Figure 5.2.2 is triggered by a steady pulse signal with the calculated average frequency of the ACRDCLI resonant circuit to perform a fair comparison between the two topologies. The Relay block in Simulink is used to perform the hysteresis current control as explained in Section 2.2.2. It determines the switch state by the error of the actual load current and the reference load current. If the error exceeds the higher threshold, the upper switch is off and the lower switch is on in the next switching period to reduce the load current. If the error is lower than the lower threshold, the next switch states would be the opposite. In this way, the load current will be limited to within the band of the reference current. Each phase has its own relay block to control the phase current.

5.2.3 Power Losses Calculation

The voltage blocking capability between the main and auxiliary switches for the ACRDCLI are the same but the ARCPI needs half the voltage rating. The current rating for the auxiliary switch in the ACRDCLI could be lower than the main switches. Still, for the ARCPI the peak current is higher than through the main switches, but since the time to conduct current is low the RMS value should be lower than in the auxiliary switch, so the current rating could maybe be lower also for the ARCPI. To ease the simulation in this project, only one Silicon Carbide (SiC) MOSFET model is used for the switches. The main inverter losses come from the switching losses and the conduction losses in the MOSFETs. In PLECS, switching devices such as MOSFETs and diodes are considered ideal, i.e. they have no voltage

drop when the devices are conducting. However, the energy losses or the voltage drop can still be obtained by the datasheet through interpolating in look-up tables. Figure 5.2.3 shows the MOSFET turn-on and turn-off switching losses profile used in PLECS for the simulations. When the MOSFET turns on or off, the instantaneous energy losses on the z-axis of the MOSFET can be obtained by interpolating current, temperature, and voltage in the 3D look-up table. As explained in Section 2.3.1, the turn-on and turn-off switching losses of MOSFETs during a switching period can be calculated.

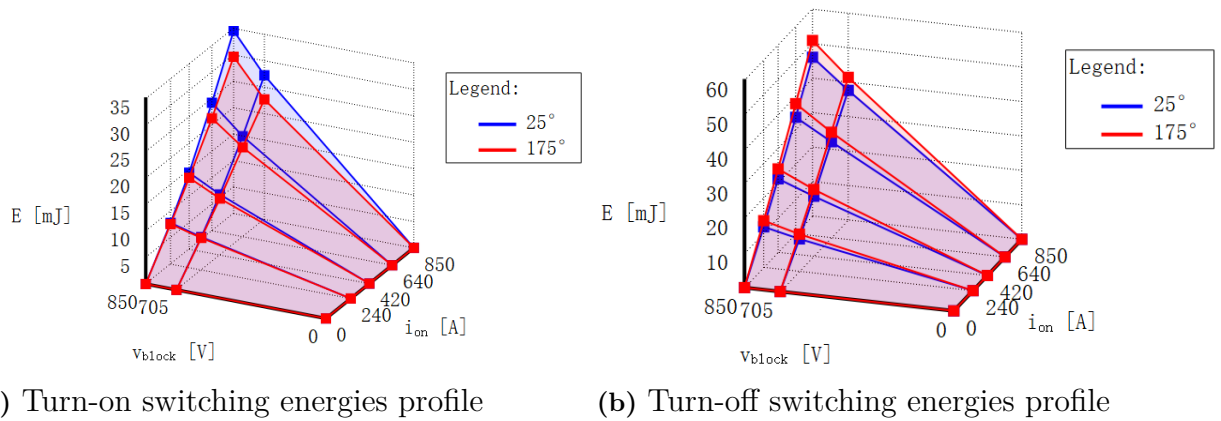


Figure 5.2.3: MOSFET turn-on (left plot) and turn-off (right plot) switching energies profile.

When the MOSFET is conducting, the MOSFET conduction losses profile which is presented in Figure 5.2.4 will be used to calculate the MOSFET conduction losses. Since the MOSFET in PLECS is an ideal component, an estimated voltage drop on the y-axis provided by the datasheet can be obtained through the interpolation of current and temperature. Later the conduction losses of MOSFETs during one switching period can be calculated as explained in Section 2.3.2.

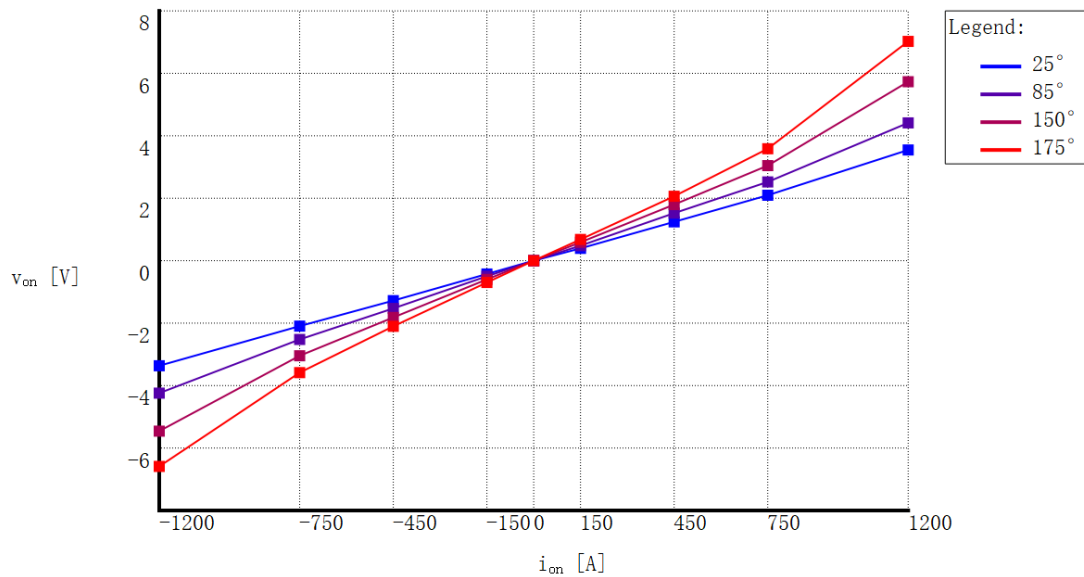


Figure 5.2.4: MOSFET conduction losses profile

In addition to the losses in the MOSFETs, the conduction losses of diodes will also be taken into account. The principles are the same as the calculation of conduction losses for MOSFETs. The diode conduction losses profile is shown in Figure 5.2.5.

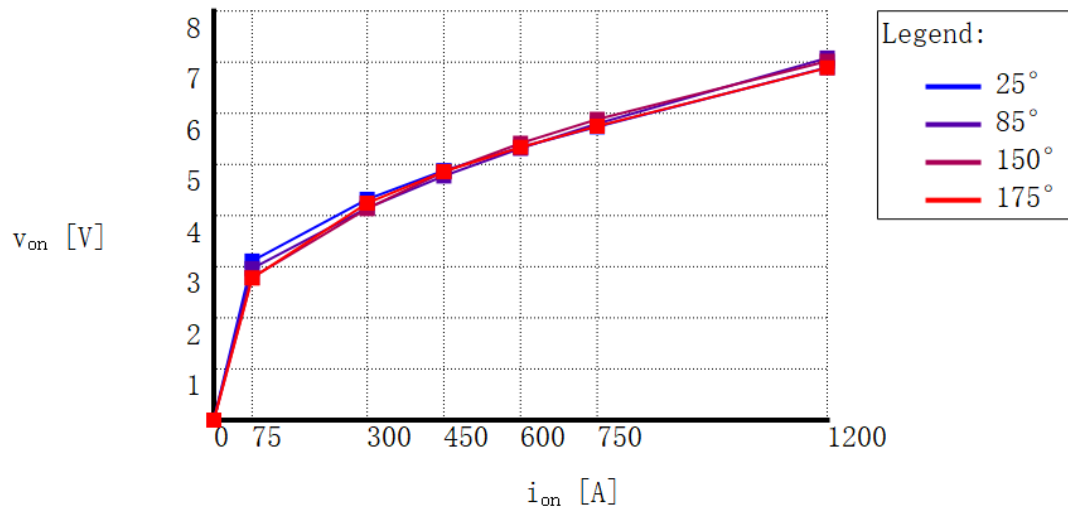


Figure 5.2.5: Diode conduction losses profile

5.3 ACRDCLI Setup

Figure 5.3.1 shows an overview of the three-phase ACRDCLI with the control system. In addition to the circuit, the control system is designed to enable control of the current and to maintain the proper operation.

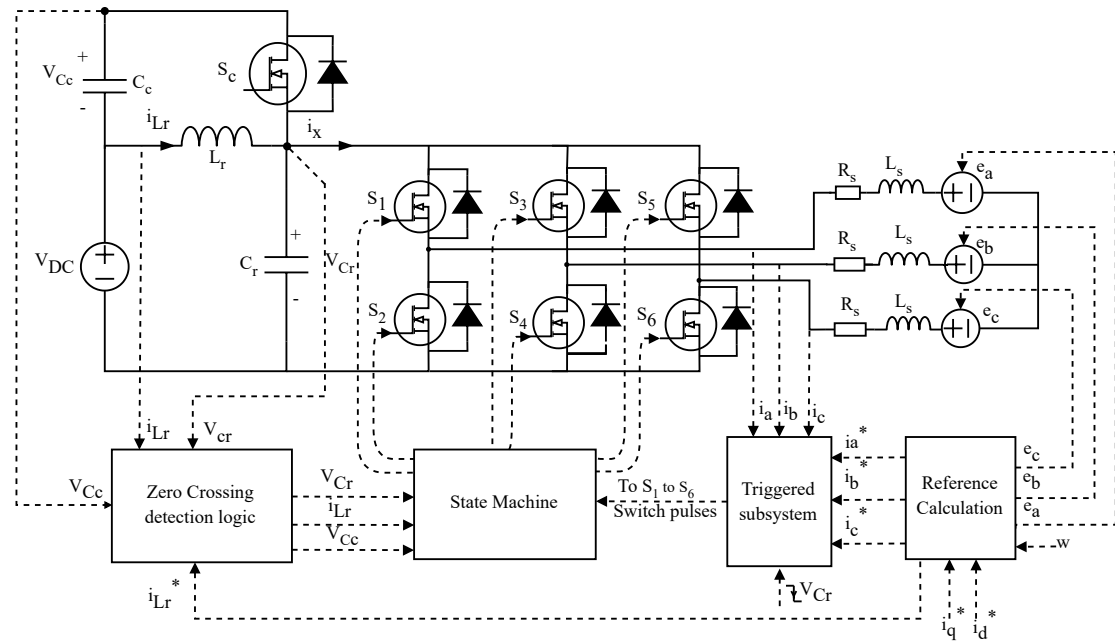


Figure 5.3.1: Overview of the three-phase ACRDCLI with hysteresis current control system showing different blocks for the zero crossing detection logic, state machine, triggered subsystem and the reference calculation.

Table 5.3.1 shows the ACRDCLI circuit parameters and initial conditions of different components used for the simulation. The resonant components and clamp capacitor values were taken from [35], but re-scaled to reach high power requirements.

Table 5.3.1: ACRDCLI circuit parameters and the initial settings

Description	Symbol	Value
Clamp capacitor	C_c [mF]	2.860
Resonant capacitor	C_r [μ F]	0.46
Resonant inductor	L_r [μ H]	10
ESR on clamp capacitor	R_{C_c} [m Ω]	0.1
ESR on resonant capacitor	R_{C_r} [m Ω]	10
ESR on resonant inductor	R_{L_r} [m Ω]	10
DC link voltage	V_{DC} [V]	700
Initial voltage of clamp capacitor	V_{C_c-init} [V]	500
Initial voltage of resonant capacitor	V_{C_r-init} [V]	0
Initial current of resonant inductor	I_{L_r-init} [A]	350
Initial current of phase A load inductor	i_{a-init} [A]	2
Initial current of phase B load inductor	i_{b-init} [A]	472.3
Initial current of phase C load inductor	i_{c-init} [A]	-474.3

5.3.1 Reference resonant inductor current calculation

For the reference calculation block in Figure 5.3.1, the reference back EMF and the reference load current are calculated in Section 5.2.1. Besides, the reference resonant inductor current will be estimated to generate a proper reference current signal to the resonant inductor to eliminate inductor overcharged which becomes

$$i_{Lr}^* = \hat{i}_x + I_{Lr}(min). \quad (5.3.1)$$

The estimated sum of three-phase load current \hat{i}_x can be calculated as

$$\hat{i}_x = i_a S_1 + i_b S_3 + i_c S_5. \quad (5.3.2)$$

where:

i_a, i_b, i_c are the phase currents in phase a, b, and c
 S_1, S_3, S_5 are the switching states (0 or 1) of the upper switch of phase leg a, b, and c.

If \hat{i}_x is negative, the inductor current reference would be 0 since the inductor doesn't need to be charged if the sum of the three-phase load current is negative. If \hat{i}_x is higher than or equal to 0, the output would be the sum of \hat{i}_x and the initial inductor current as the reference inductor current to ensure the inductor can be boosted properly during each period.

5.3.2 Triggered subsystem

The triggered subsystem block for ACRDCLI in Figure 5.3.1 is triggered by the falling signal of resonant voltage V_{Cr} and used for current control. It uses the hysteresis current control to maintain proper currents as explained in Section 5.2.2. However, for the first operating mode of ACRDCLI, all six main switches should be on to maintain the proper operating condition. Therefore, the output signals need to be processed by the state machine before they can be applied to switches.

5.3.3 State Machine

The zero crossing detection block in Figure 5.3.1 detects the pre-conditions of the next operating state of the ACRDCLI as explained in four modes of operation in Section 3.2. When the simulation starts, the state machine starts at State 1. If the pre-condition for the next state is fulfilled, the state machine would proceed to the next state. The same principle is used for the rest of the states in the state machine. During the transition between State 4 and State 1, the state machine overwrites the phase leg switch signal of the previous switching period with the new switch signal of the triggered subsystem to control the load current. The progression and cycling between states allow for current control and energy balancing of the resonant components. The flow chart of the ACRDCLIs state machine is shown in Figure 5.3.2.

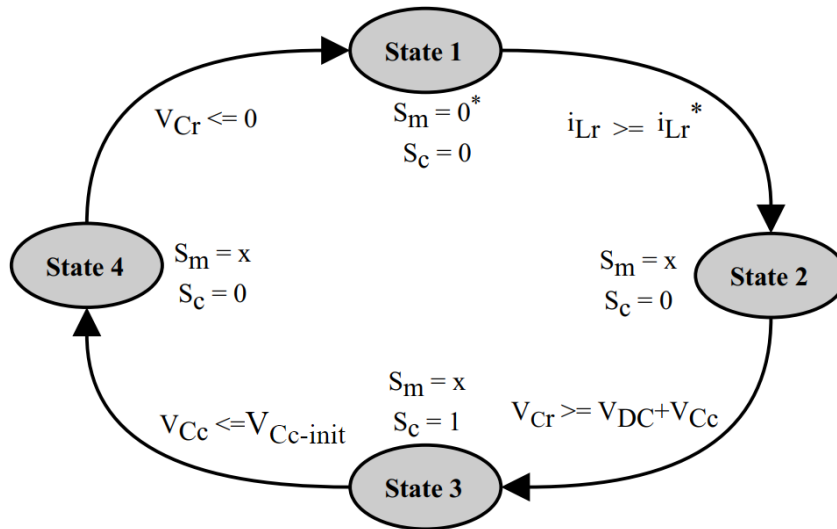


Figure 5.3.2: Flow chart for the ACRDCLI with pre-conditions showing state 1 to state 4.

Table 5.3.2 shows the switching combination table for the six main switches. Switch state 0 means that the upper switch of the phase leg is off and the lower switch is on. Switch state is 1 means that the upper switch of the phase leg is on and the lower switch is off. When the state x is 0^* , it represents a special case that all six main switches are turned on, which is used during State 1 in Figure 5.3.2. It is the hysteresis function in the triggered subsystem block that decides which switch state that should be used in States 2, 3, and 4 to keep the phase currents within the hysteresis band. The phase currents are sampled in the transition between State 4 to State 1 and based on these currents the switch state that is going to be used when the transition to State 2, 3, and 4 happens is determined. From the sampled currents also the reference for the L_r inductor current is calculated with (5.3.1).

Table 5.3.2: Switching combination table for the six main switches of the ACRD-CLI

x	S_1	S_3	S_5
1	0	0	0
2	0	0	1
3	0	1	0
4	0	1	1
5	1	0	0
6	1	0	1
7	1	1	0
0^*	1	1	1

5.3.4 Average Frequency Calculation

In the ACRDCLI, the time to charge the resonant inductor of each period is different due to different reference resonant inductor currents which will result in a different switching frequency for each period. An average switching frequency f_{sw} within one fundamental period is needed when compared with other topologies and it can be calculated as

$$f_{sw} = \frac{N}{T_p} \quad (5.3.3)$$

where:

f_{sw} is the resonant circuit average switching frequency,

T_p is the simulation time,

N is the number of cycles completed by the resonant circuit of the ACRDCLI during T_p

5.4 ARCPI Setup

Figure 5.4.1 shows an overview of the three-phase ARCPI with the control system. ARCPIs control system includes the zero crossing block, the state machine, the SVPWM block, and the reference calculation block. They are used to control the load current and maintain the energy balance in the resonant components.

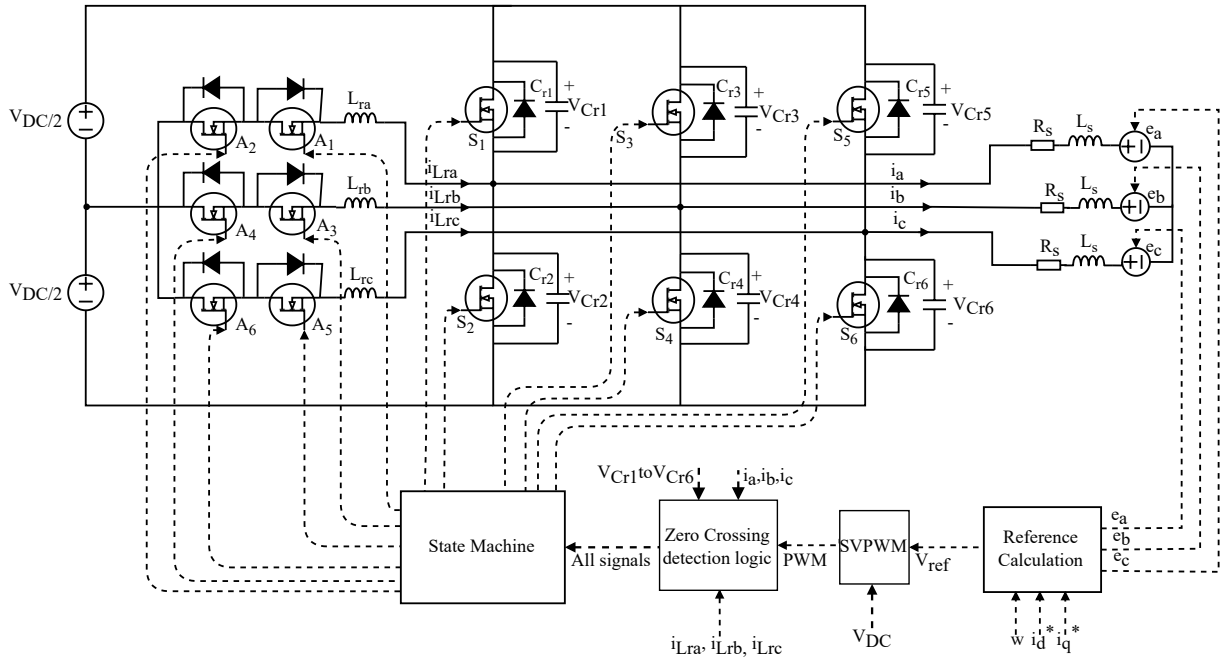


Figure 5.4.1: Overview of the three-phase ARCPI with the hysteresis current control system showing different blocks for the zero crossing detection logic, the state machine, the SVPWM, and the reference calculation

The ARCPI resonant component parameters used in this project are taken from Pre-Switch Inc [36] and the parameters are listed in Table 5.4.1.

Table 5.4.1: ARCPI circuit parameters and the initial settings

Description	Symbol	Value
Resonant capacitor	C_{rx} [nF]	1
Resonant inductor	L_{rx} [nH]	360
ESR on resonant capacitor	R_{Crx} [m Ω]	60
ESR on resonant inductor	R_{Lrx} [m Ω]	10
DC link voltage	V_{DC} [V]	700
Initial voltage of resonant capacitor 1	$V_{Cr1-init}$ [V]	700
Initial voltage of resonant capacitor 2	$V_{Cr2-init}$ [V]	0
Initial voltage of resonant capacitor 3	$V_{Cr3-init}$ [V]	700
Initial voltage of resonant capacitor 4	$V_{Cr4-init}$ [V]	0
Initial voltage of resonant capacitor 5	$V_{Cr5-init}$ [V]	0
Initial voltage of resonant capacitor 6	$V_{Cr6-init}$ [V]	700
Initial current of resonant inductor	$I_{Lrx-init}$ [A]	0
Initial current of phase A load inductor	i_{a-init} [A]	2
Initial current of phase B load inductor	i_{b-init} [A]	472.3
Initial current of phase C load inductor	i_{c-init} [A]	-474.3

5.4.1 Reference Calculation

In the reference calculation block in Figure 5.4.1, the reference back EMF and the reference phase voltage in $\alpha\beta$ coordinates are calculated as Section 5.2.1. The SVPWM block in Figure 5.4.1 uses the reference phase voltage in $\alpha\beta$ coordinates and V_{DC} to generate the PWM signals as explained in Section 2.2.1.

5.4.2 State Machine

Figure 5.4.2 shows the flow chart of the ARCPIs state machine block used by the phase leg for phase a in the three-phase ARCPI. The red rising symbol represents the rising edge of the PWM signal, the green falling symbol represents the falling edge of the PWM signal. The other two phase legs, use the same state machine but separately. Therefore the control system for each phase leg is independent and they receive the PWM signals for their phase leg. The zero crossing detection block in Figure 5.4.1 detects the pre-conditions of the next operating state similar to ACRDCLI. The state machine for one phase leg will be explained and the flow chart is the same for the other two phases. The load current in Figure 5.4.2 represents the phase current, in this case $i_{load} = i_a$.

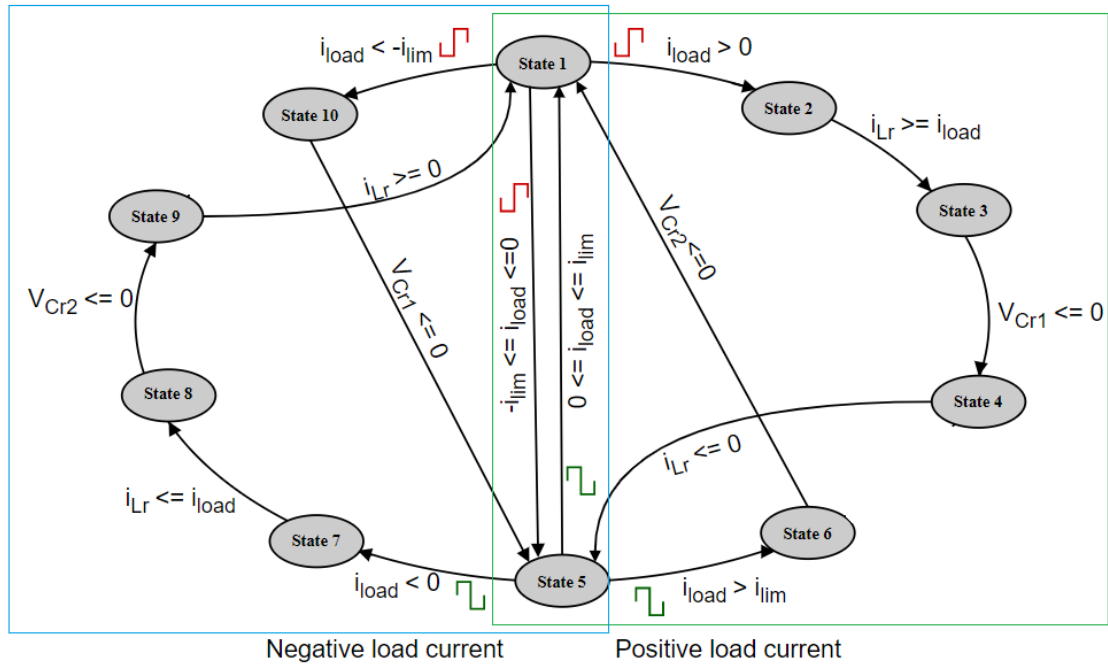


Figure 5.4.2: Flow chart for the phase leg for phase a in the three-phase ARCPI. The load current represents the phase current, in this case $i_{load} = i_a$

When the load current is positive, the state machine will stay in the circulation of positive load current cases which are shown as the states in the green box in Figure 5.4.2, and the working principles are explained in Section 4.2.1. When the load current is negative, the state machine will stay in the circulation of the negative case, which is shown as the states in the blue box. The preconditions of the negative cases are different from those of the positive cases which are shown in the conditions between negative states in Figure 5.4.2.

However, an extreme case has also been considered. When the load current varies from positive to negative or from negative to positive, the current will be zero or very small for a very short time. Assume it is a positive case and the state machine is at State 6, V_{Cr2} needs to be discharged to 0 V to fulfill the precondition of State 1 to continue. If V_{Cr2} can not be discharged before the rise PWM signal of the next period, the state machine would stop working due to it always stays at State 6. To prevent this, when the state machine is at State 5 with the load current lower than the threshold (i_{lim}) and higher than 0, it would directly transit to State 1 using hard switching. On the other hand, when the state machine is at State 1 with the load current higher than the threshold ($-i_{lim}$) and lower than 0, it would directly transit to State 5 using hard switching.

Table 5.4.2 shows the switching combination table for the ten states of the phase leg for phase a in the three-phase ARCPI where 0 represents that the switch is turned off and 1 represents that the switch is turned on.

Table 5.4.2: Switching combination table for the ten states of the phase leg for phase a in the three-phase ARCPI.

State	A_1	A_2	S_1	S_2
1	0	0	0	1
2	0	1	0	1
3	0	1	0	0
4	0	1	1	0
5	0	0	1	0
6	0	0	0	0
7	1	0	1	0
8	1	0	0	0
9	1	0	0	1
10	0	0	0	0

6

Results and Discussions

In this chapter, the simulation results from the HSI, ACRDCLI, and ARCPI with two different control methods will be presented and discussed based on the explanation from the previous chapter. Losses in different components are calculated and a comparison table of the losses will be shown for the different converters. Finally, the performance of the ARCPI was evaluated for operation at different frequencies and reference q currents, with the reference d current set to 0 A.

6.1 HSI

Before calculating the average power losses of the MOSFETs, it would be advantageous to understand the switching behaviour of the HSI. Figure 6.1.1 shows the waveforms of voltage across and current flowing through the top switch S_1 in phase leg a, the switching energies and the conduction losses for one electrical period. The top plot shows the voltage across and current flowing through top MOSFET S_1 in phase leg a. In this case, the RMS value of the output phase current is 384 A and the PWM switching frequency is $f_{sw} = 33$ kHz. The most interesting aspect from the plots are that it can be observed that between $t = 4$ ms to 7 ms the top switch is off and in between $t = 14$ ms to 17 ms the switch is in constant conduction mode. This is connected to the SVPWM control technique which can be seen in Figure 2.2.2, to generate the required average voltage in sector I, phase a is always on which means phase a is always off in IV. Similarly, phase b is on in sector III and off in VI whereas in sector II phase c is off and phase c is on in sector V. Due to this switching pattern, the other two phases are switching to generate the average reference voltage during these periods. This is done to minimize the switching instants.

The middle and bottom plot illustrates the instantaneous values of turn on and off switching energies according to (2.3.2) of the MOSFET and the conduction losses of the MOSFET and diode calculated with (2.3.6) and (2.3.8). There are no switching losses between $t = 0$ to 10 ms, during this time it is the bottom switch that has the switching losses. Also, the conduction losses occur due to current conduction, between 14 to 17 ms there is a ripple this is because the other two phases are switching in the HSI. By taking the average of these over a switching period and summing them together the total average power losses for the six MOSFETs and the diodes can be calculated with (3.3.2) to 2.69 kW in this case.

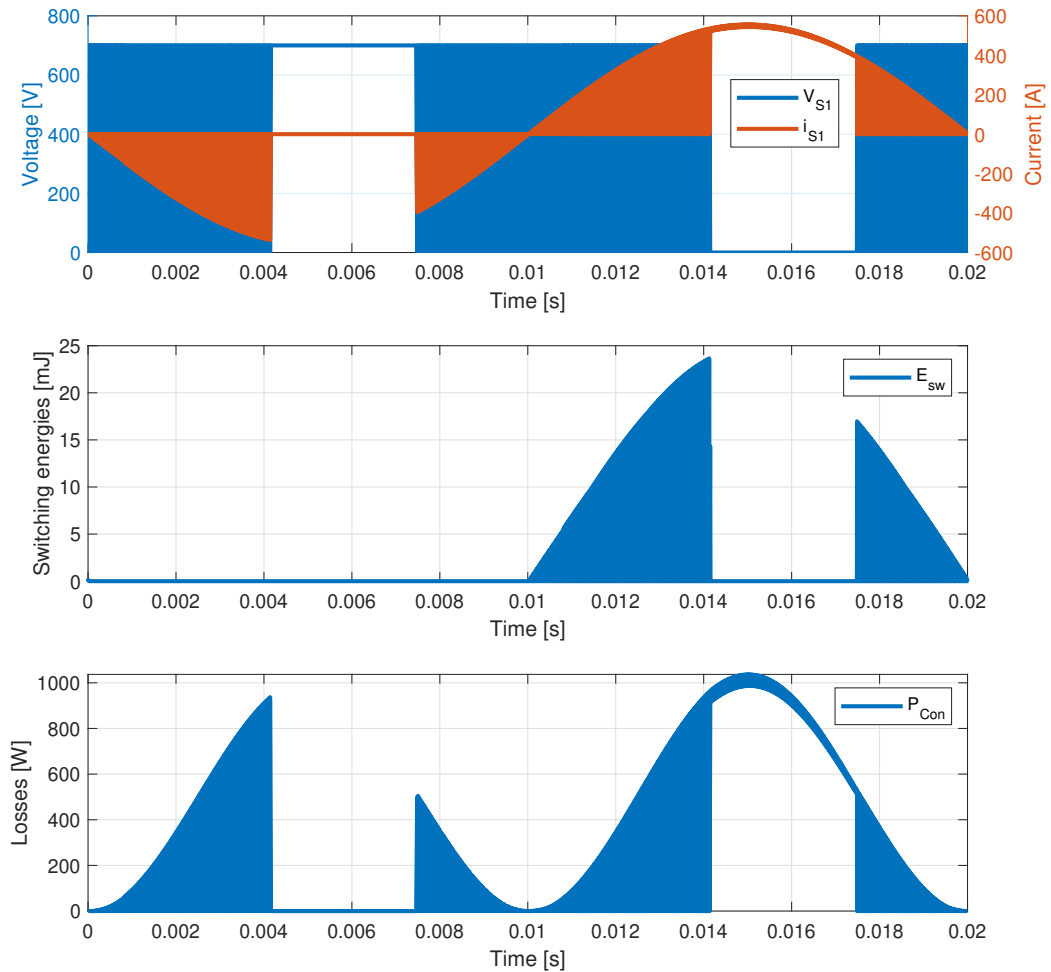


Figure 6.1.1: Simulated waveforms of HSI with SVPWM showing voltage and current (top plot), switching energies (middle plot) and conduction losses (bottom plot) of the one of the MOSFETs in phase leg a. The PWM switching frequency $f_{sw} = 33$ kHz.

Figure 6.1.2 illustrates the zoomed-in waveform of the above Figure 6.1.1 showing the switching instants during the turn on and off of the top switch S_1 in phase leg a. At the intersection of the voltage and current there is a high switching losses due to hard switching. Theoretically, the switching frequency may be decreased, but the signal's harmonic distortion would increase. From the waveform it is apparent that the turn-on switching energies are lower than the turn-off. This could be compared with the switching energies profile in the Figure 5.2.3, where the turn-off energies profile is higher than the turn-on. The observed increase in the current could be attributed to more turn-off energies. It can be seen in the bottom plot that increase in the current increases the conduction losses.

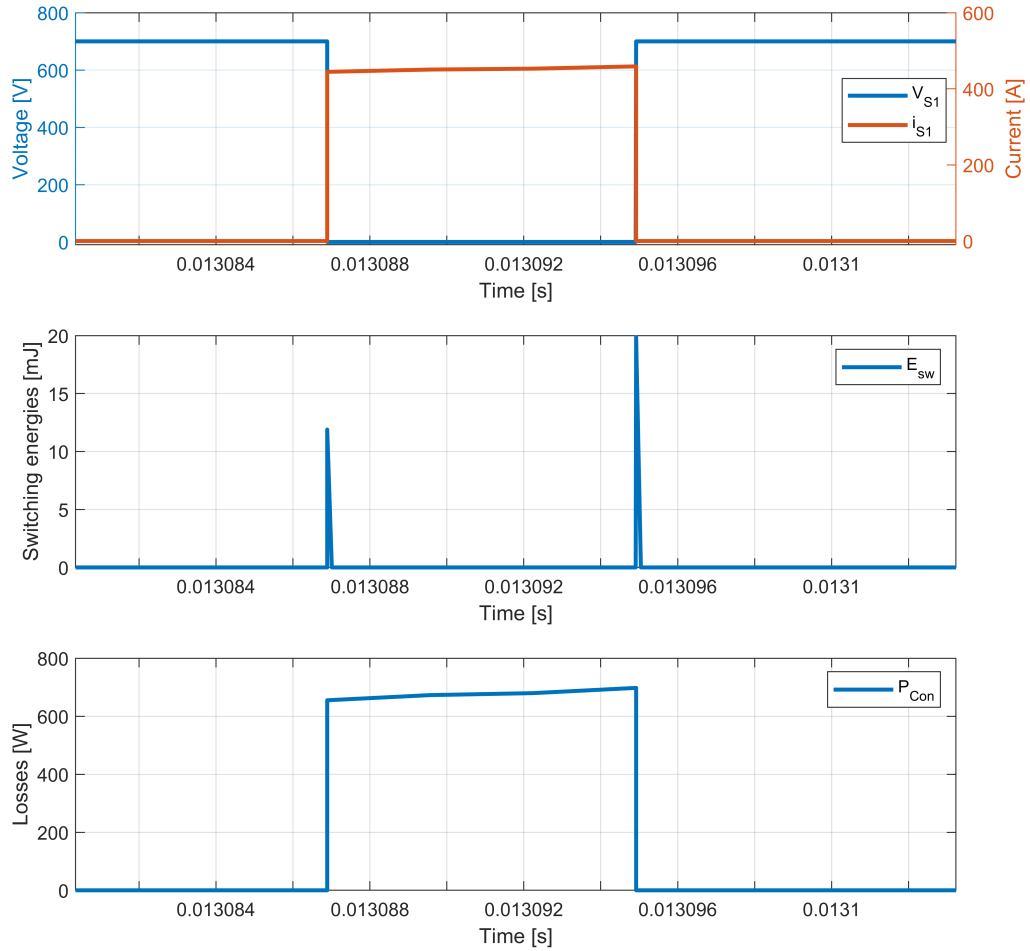


Figure 6.1.2: Zoomed-in plot showing voltage and current (top plot), switching energies (middle plot), and conduction losses (bottom plot) of the one of the MOSFETs in phase leg a. The PWM switching frequency $f_{sw} = 33$ kHz.

6.2 ACRDCLI

Figure 6.2.1 shows the simulated waveform of the resonant DC link voltage V_{Cr} for the same operation condition as for the HSI in Figure 6.1.1, but the results are zoomed in to only show the first 0.4 ms. The input DC link voltage is 700 V and the initial voltage of the clamp capacitor is 500 V, this provides a clamping voltage of 1200 V.

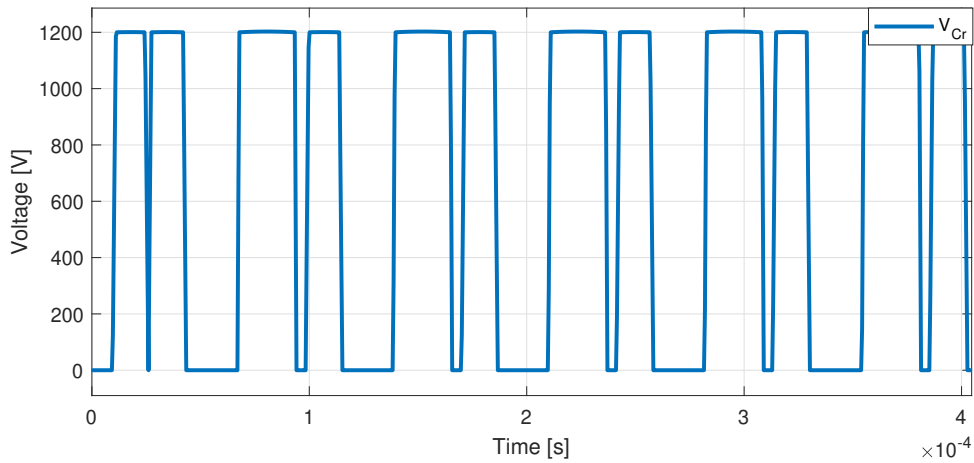


Figure 6.2.1: Resonant DC link voltage V_{Cr} waveform for the three-phase ACRD-CLI with a total clamping voltage of 1200 V.

The resonant circuit are also analysed as shown in Figure 6.2.2. The current i_{Lr}^* is calculated with (5.3.1) and i_{Lr} can follow the reference current according to the precondition of the state machine. It can be seen that when the current i_x increases the current i_{Lr} increases.

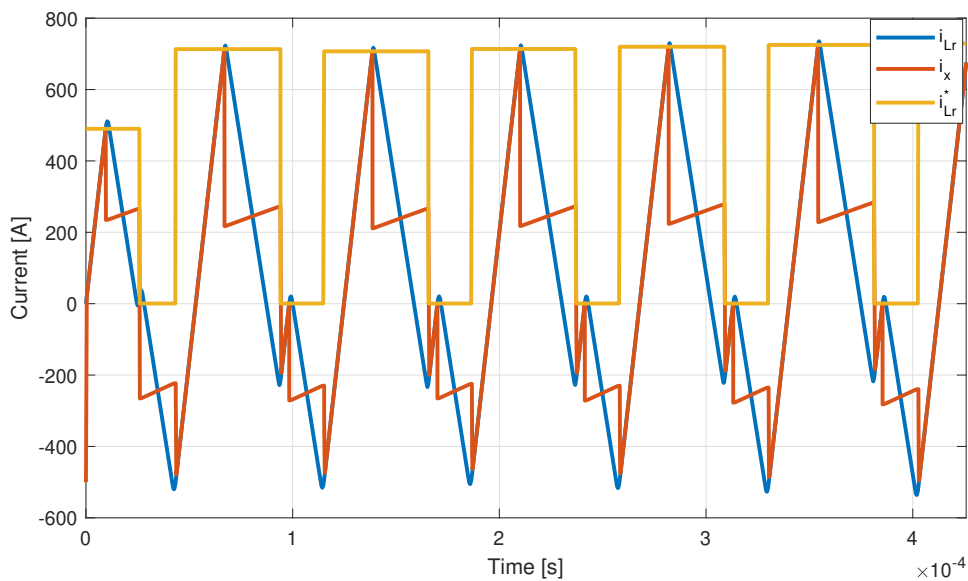


Figure 6.2.2: Simulated plots of three-phase ACRDCLI showing current flowing through the resonant inductor i_{Lr} (blue plot), inverter DC link current i_x (red plot) and the reference inductor current i_{Lr}^* (yellow plot)

In Figure 6.2.3 top plot shows the voltage across clamp capacitor V_{C_c} and the bottom plot is the current flowing through the clamp circuit i_{C_c} for the three-phase ACRDCLI.

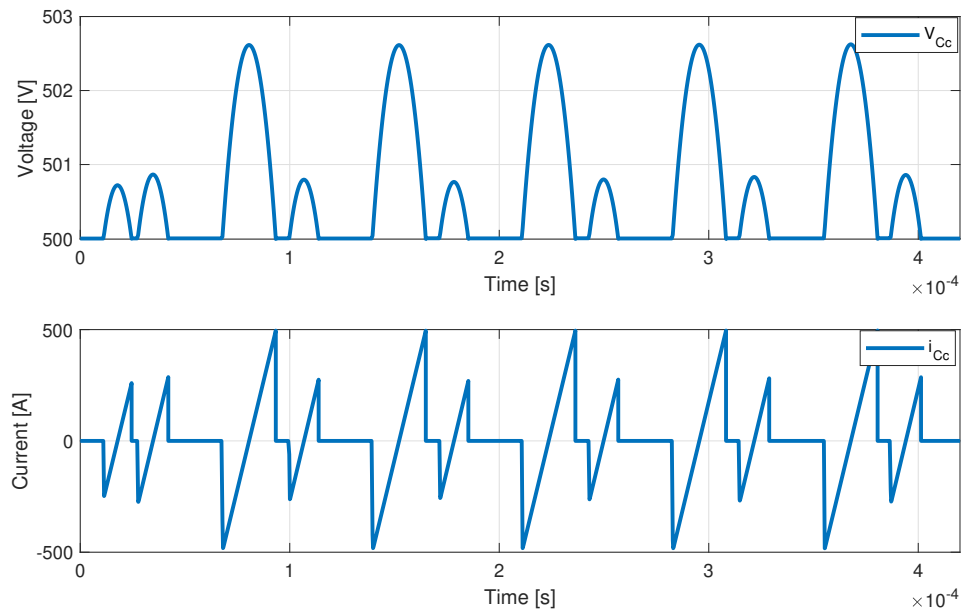


Figure 6.2.3: Voltage across the clamp capacitor C_c (top plot) and the current flowing through the clamp circuit (bottom plot). The initial voltage of the clamp capacitor is 500 V.

Figure 6.2.4 shows the zoomed in plot of above figure where the switch S_c is turned on and off. It can be observed at $t = 0.67$ ms, the clamp diode D_c is conducting and the current i_{C_c} is negative. The switch S_c is turned on under the clamp capacitor C_c charge balance i.e, the amount of charge equals to the net charge out. The control manner of the switch S_c is dependant on the clamping voltage and the current flowing through the clamp capacitor i_{C_c} .

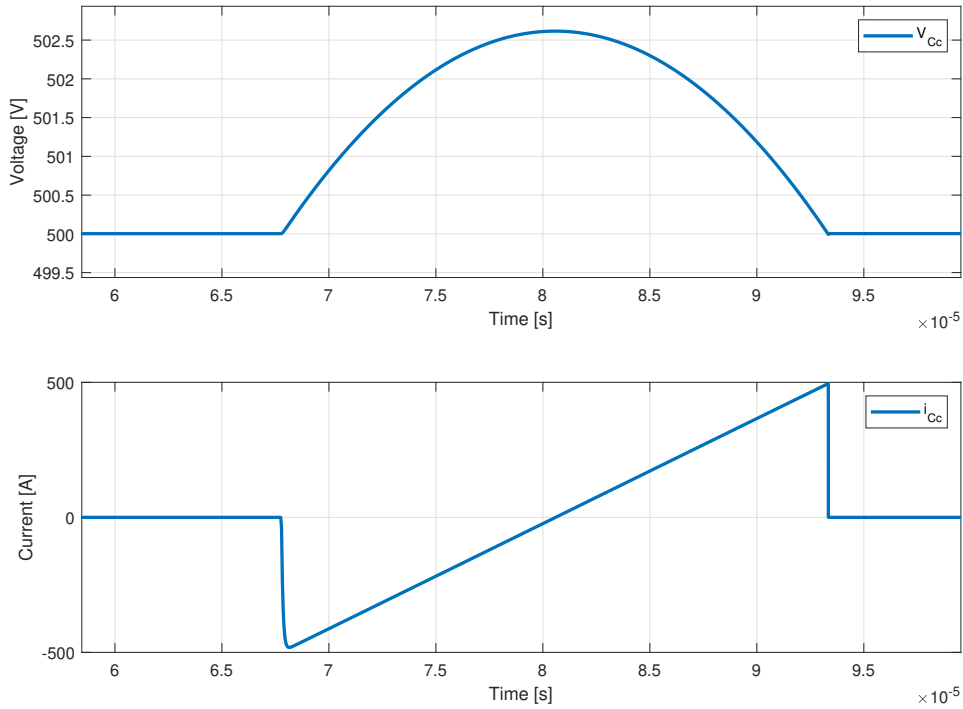


Figure 6.2.4: Zoomed in plot showing the voltage across the clamp capacitor C_c (top plot) and the current flowing through the clamp circuit (bottom plot).

6.3 ARCPI

In this section simulation results for three-phase ARCPI will be studied in detail. The input DC link voltage $V_{DC} = 700$ V and the PWM switching frequency $f_{sw} = 45$ kHz in this case. Figure 6.3.1 shows the voltage across the resonant capacitors C_{r3} , C_{r4} and the resonant inductor current i_{Lrb} when the phase current is positive.

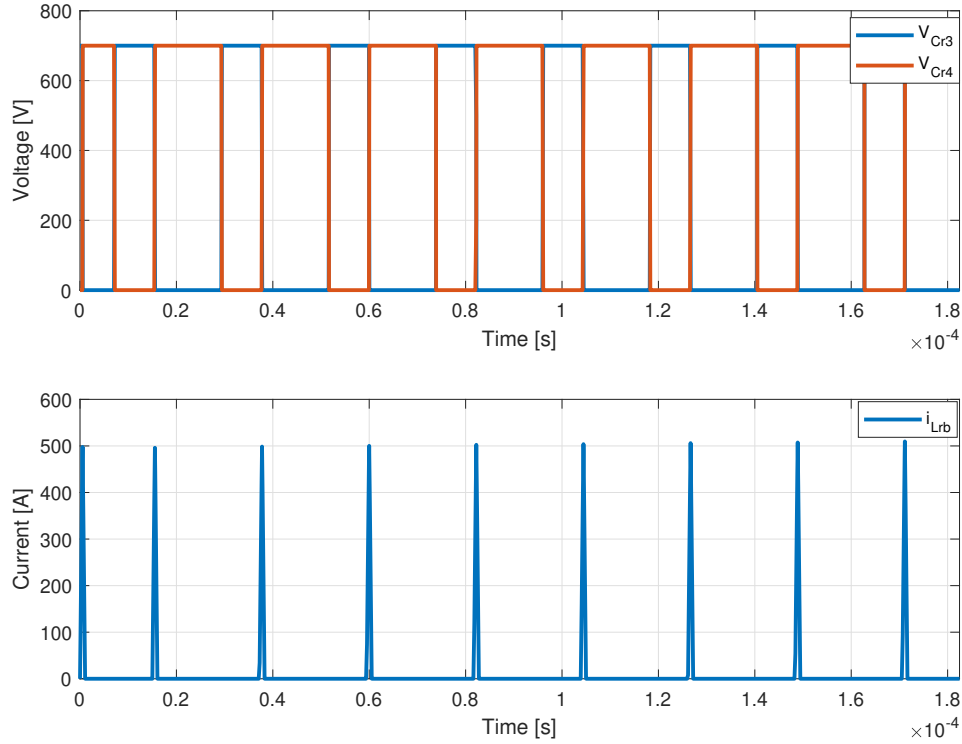


Figure 6.3.1: Simulated phase b waveforms for the three-phase ARCPI when the load current is positive. The voltage across the resonant capacitors (top plot) which are connected parallel to the top and bottom switches and the current is through the auxiliary circuit (bottom plot). The input DC link voltage is 700 V and the PWM switching frequency is 45 kHz.

Figure 6.3.2 shows the zoomed-in waveform of turn on and off of the main switches S_3 , S_4 . At $t = 0.375$ ms the auxiliary switch A_4 is triggered by the PWM signal. At this time the resonant inductor current i_{Lrb} starts increasing. When i_{Lrb} exceeds the load current, then bottom switch S_4 is turned off at $t = 0.378$ ms and the voltage V_{Cr4} reaches DC link voltage of 700 V. When the voltage V_{Cr3} reaches zero, top switch S_3 is turned on and ZVS is achieved to minimise the switching losses. It can be seen from the plots that the circuit fulfills the six operating states as explained in Section 4.2.

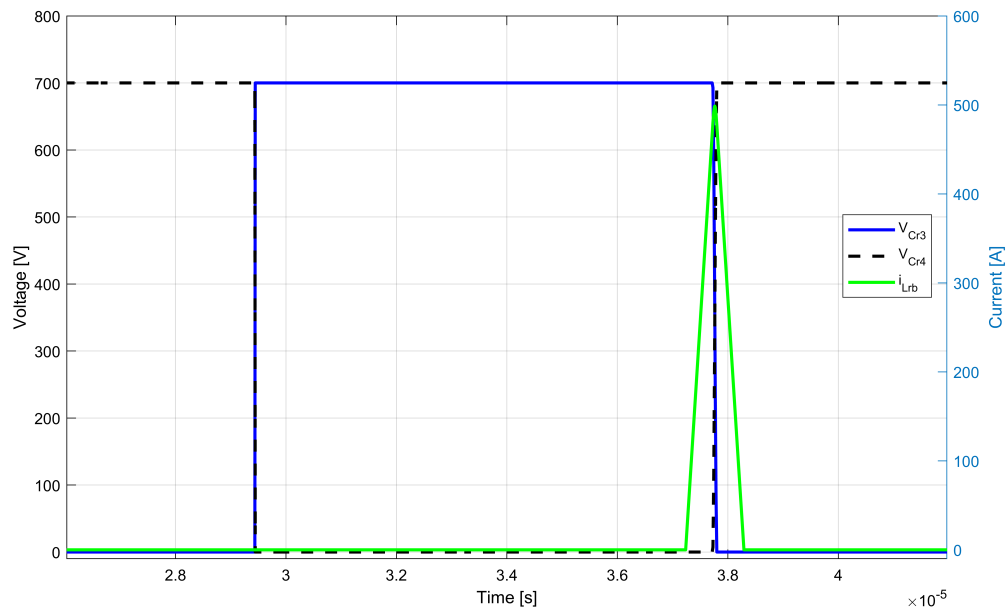


Figure 6.3.2: Zoomed-in simulated phase b waveforms showing turn on and off instants for the three-phase ARCPI when the load current is positive. The voltage across the resonant capacitors (top plot) is connected to the top and bottom switches and the current is through the auxiliary circuit (bottom plot). The input DC link voltage is 700 V and the PWM switching frequency is 45 kHz.

Figure 6.3.3 illustrates the simulated waveform showing the voltage across the resonant capacitors V_{Cr5} and V_{Cr6} , resonant inductor current i_{Lrc} when the load current is negative. Initially, V_{Cr6} is 700 V and the current i_{Lrc} is zero. The commutation from the main switches S_5 to S_6 with negative load current is successfully achieved by auxiliary switch A_5 .

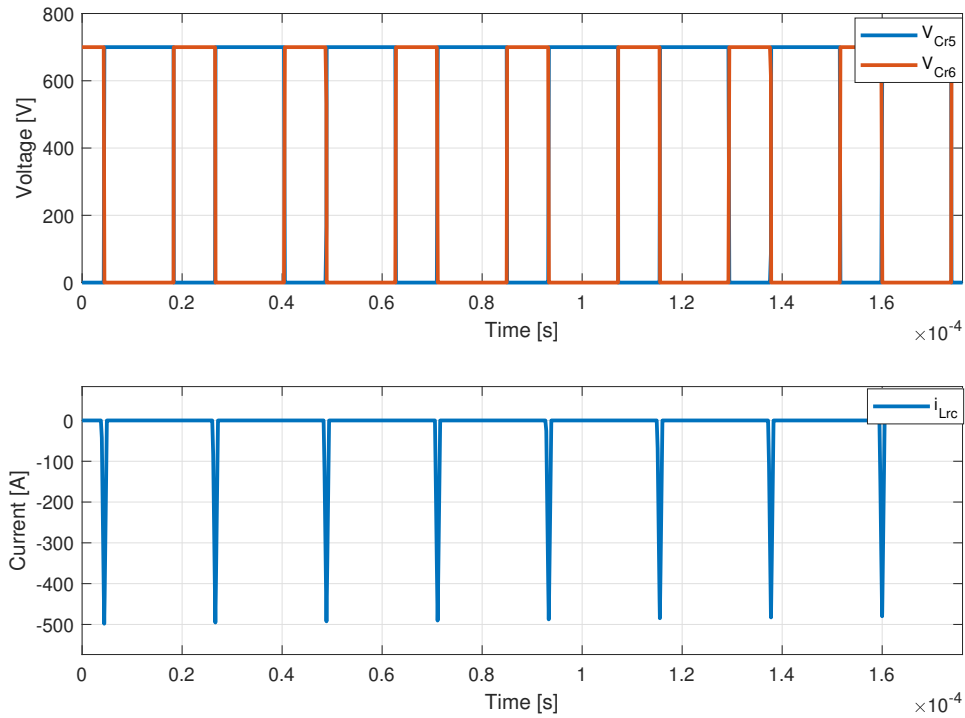


Figure 6.3.3: Simulated phase c waveform for the three-phase ARCPI when the load current is negative. The voltage across the resonant capacitors (top plot) which are connected parallel to the top and bottom switches and the current is through the auxiliary circuit (bottom plot). The input DC link voltage is 700 V and the PWM switching frequency is 45 kHz.

Figure 6.3.4 shows the zoomed-in waveform for the negative load current case for the turn on and off instants for the main switches, S_5, S_6 . Initially, the switch S_5 is conducting and the auxiliary switch A_5 is not triggered. When the switch A_5 is triggered by PWM signal, it is turned on to start the resonant operation. At $t = 0.484$ ms, the switch S_5 is turned off when the current i_{Lrc} reaches the load current. It can be observed that the voltage V_{Cr6} decreases to zero before the current i_{Lrc} drops to zero level.

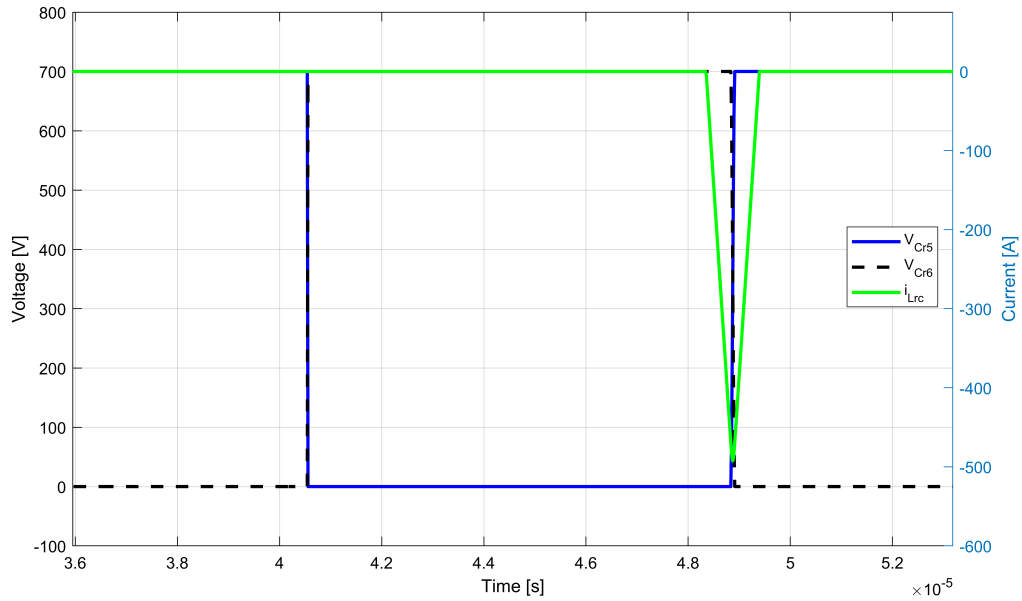


Figure 6.3.4: Zoomed-in simulated phase c waveforms showing turn on and off instants for the three-phase ARCPI when the load current is negative. The voltage across the resonant capacitors (top plot) is connected to the top and bottom switches and the current is through the auxiliary circuit (bottom plot). The input DC link voltage is 700 V and the PWM switching frequency is 45 kHz.

Figure 6.3.5 shows the three-phase output currents and the currents flowing through the auxiliary circuits. The resonant inductor currents follow the output phase current. The output power is 84.26 kW and the fundamental frequency f_1 is 50 Hz.

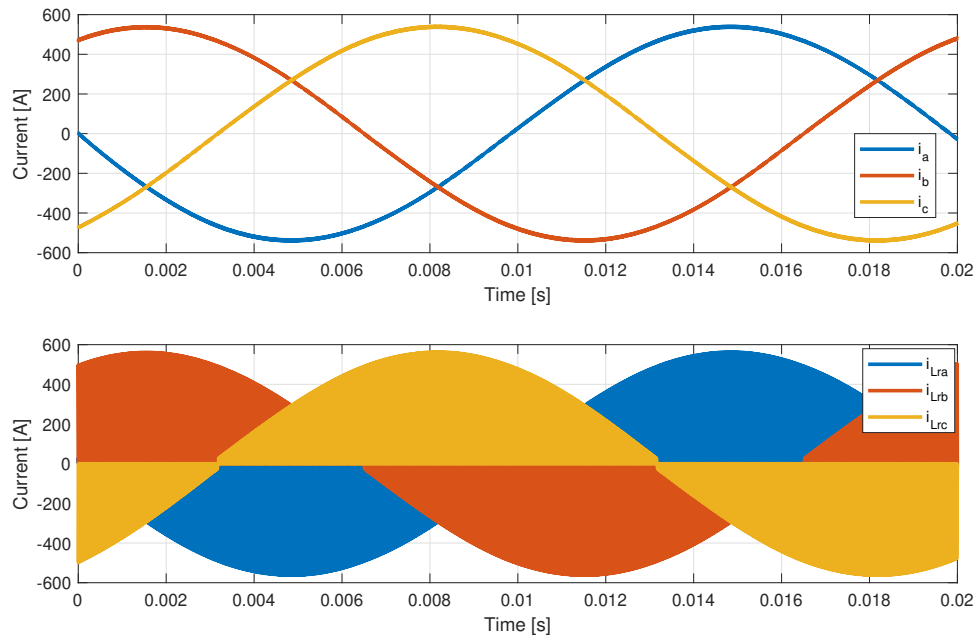


Figure 6.3.5: Top plot shows the three-phase output current and the bottom plot shows the resonant current inductor currents flowing through the auxiliary circuit.

Zero crossing transition when the output current changes from negative to positive can be seen in Figure 6.3.6. As explained in Section 5.4.2, this is achieved using hard switching. At $t = 9.8$ ms, small distortion is visible and the ARCPI can switch successfully.

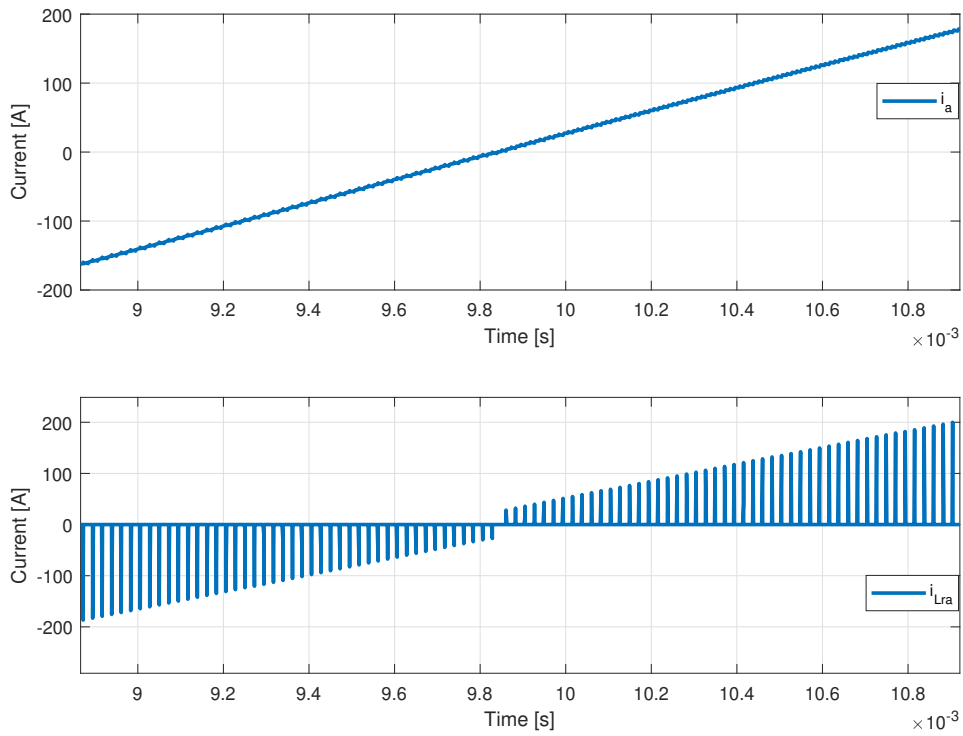


Figure 6.3.6: Zoomed-in plot of phase A output current (top plot) and resonant inductor current (bottom plot). Zero crossing can be seen when the current changes from negative to positive.

Figure 6.3.7 shows the simulated waveforms of voltage across the top switch in the three-phase ARCPI, the current flowing through it, the switching energies and the conduction losses to understand the switching behaviour.

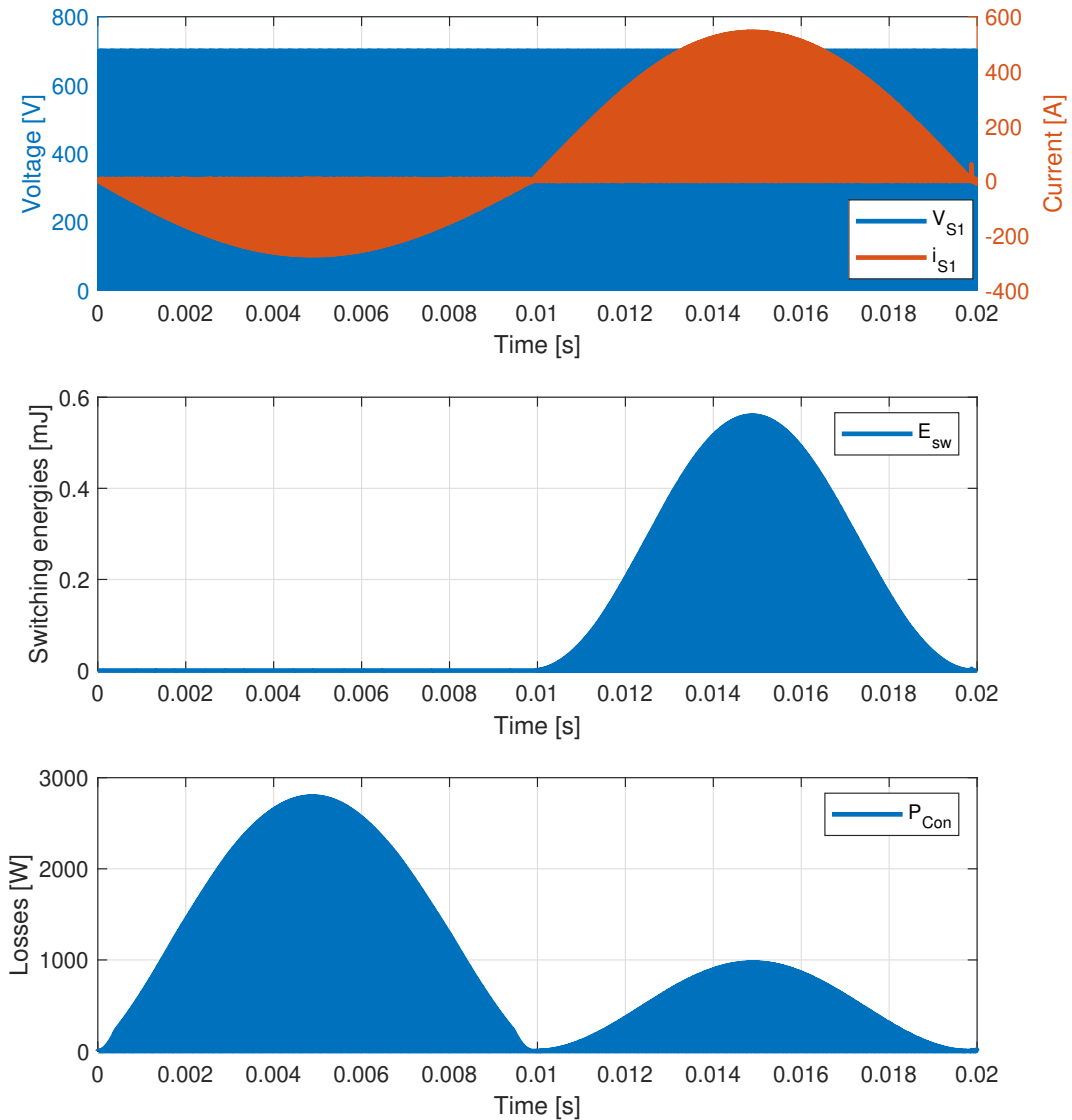


Figure 6.3.7: Simulated waveforms of ARCPI showing voltage and current (top plot), switching energies (middle plot), and conduction losses (bottom plot) of one of the MOSFETs in phase leg A. The PWM switching frequency $f_{sw} = 33$ kHz.

Figure 6.3.8 shows the zoomed-in waveform of turn on and off instant of the main switch S_1 . In the simulation result, the current flowing through the top main switch starts rising when the voltage decreases to zero during turn on instant which can be observed at $t = 13.21$ ms. The main switches are turned on at ZVS. There are no turn-on switching losses however main switches has reduced turn-off losses. This is

due to the switch is not turned off exactly at zero voltage, the current falls to zero when there is a small voltage. The average switching losses during one electrical period for the six switches are calculated with (2.3.2) to be 0.02 kW and the total average conduction losses for the six main switches and the diodes according to (2.3.7) and (2.3.9) is 1.7 kW.

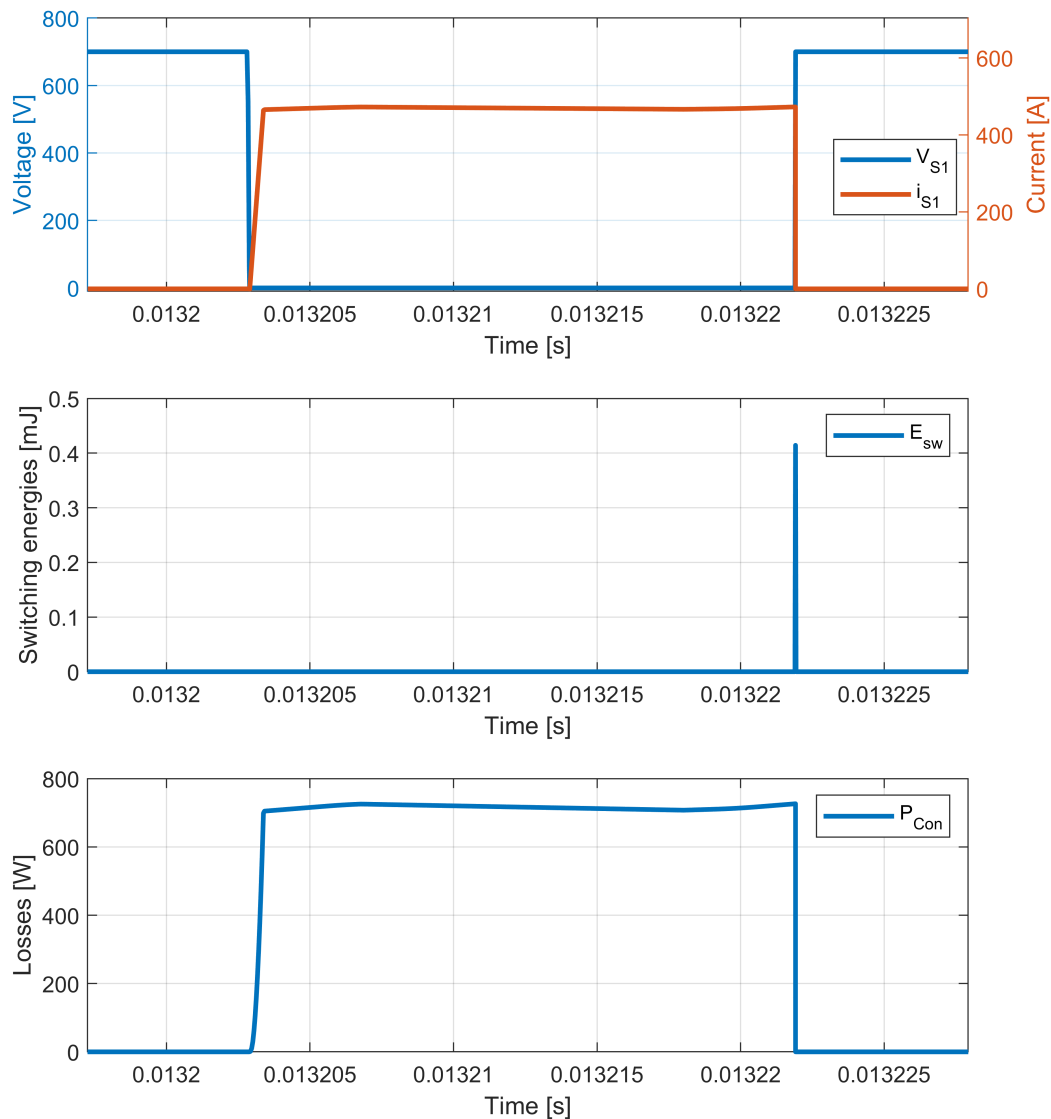


Figure 6.3.8: Zoomed-in plot showing voltage and current (top plot), switching energies (middle plot), and conduction losses (bottom plot) of the one of the MOSFETs in phase leg A. The PWM switching frequency $f_{sw} = 33$ kHz.

The Auxiliary switches in the three-phase ARCPI turn on-off under Zero Current Switching (ZCS) conditions. Hence there are only conduction losses in the auxiliary switches. The voltage across the the auxiliary switch A_1 and current flowing through,

switching energies and the conduction losses is shown in Figure 6.3.9. It can be seen that half of the DC link voltage 350 V is applied to the auxiliary switch. The rating of the auxiliary switch could be selected for the half of the DC link voltage.

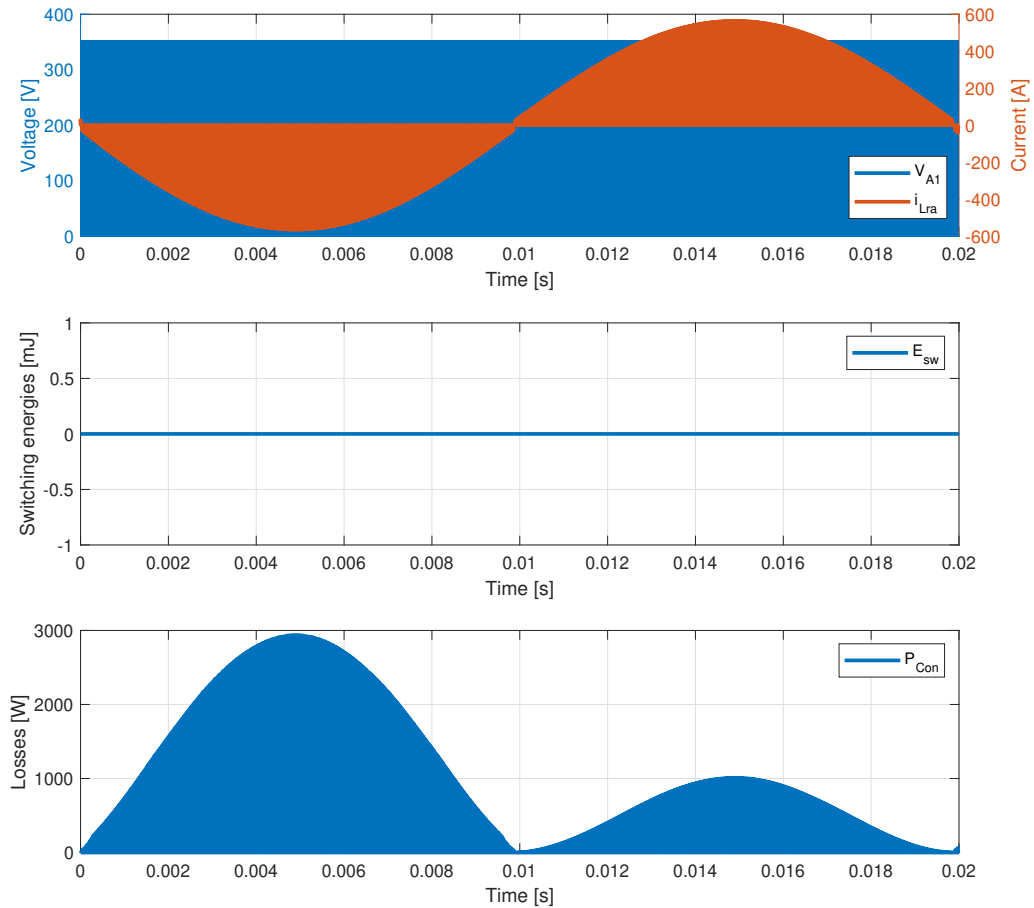


Figure 6.3.9: Simulated waveforms of the three-phase ARCPI showing the voltage across and the current flowing (top plot), switching energies (middle plot), and the conduction losses (bottom plot) of one of the auxiliary switch A_1 in phase leg a auxiliary circuit.

Figure 6.3.10 shows the zoomed-in plot, where the auxiliary switch is turned at near to zero of the resonant inductor current. The resonant inductor current flows through the auxiliary circuit. Since the auxiliary circuit is conducting for a short duration, the total average losses for the six auxiliary switches calculated with (4.3.2) is only 0.09 kW.

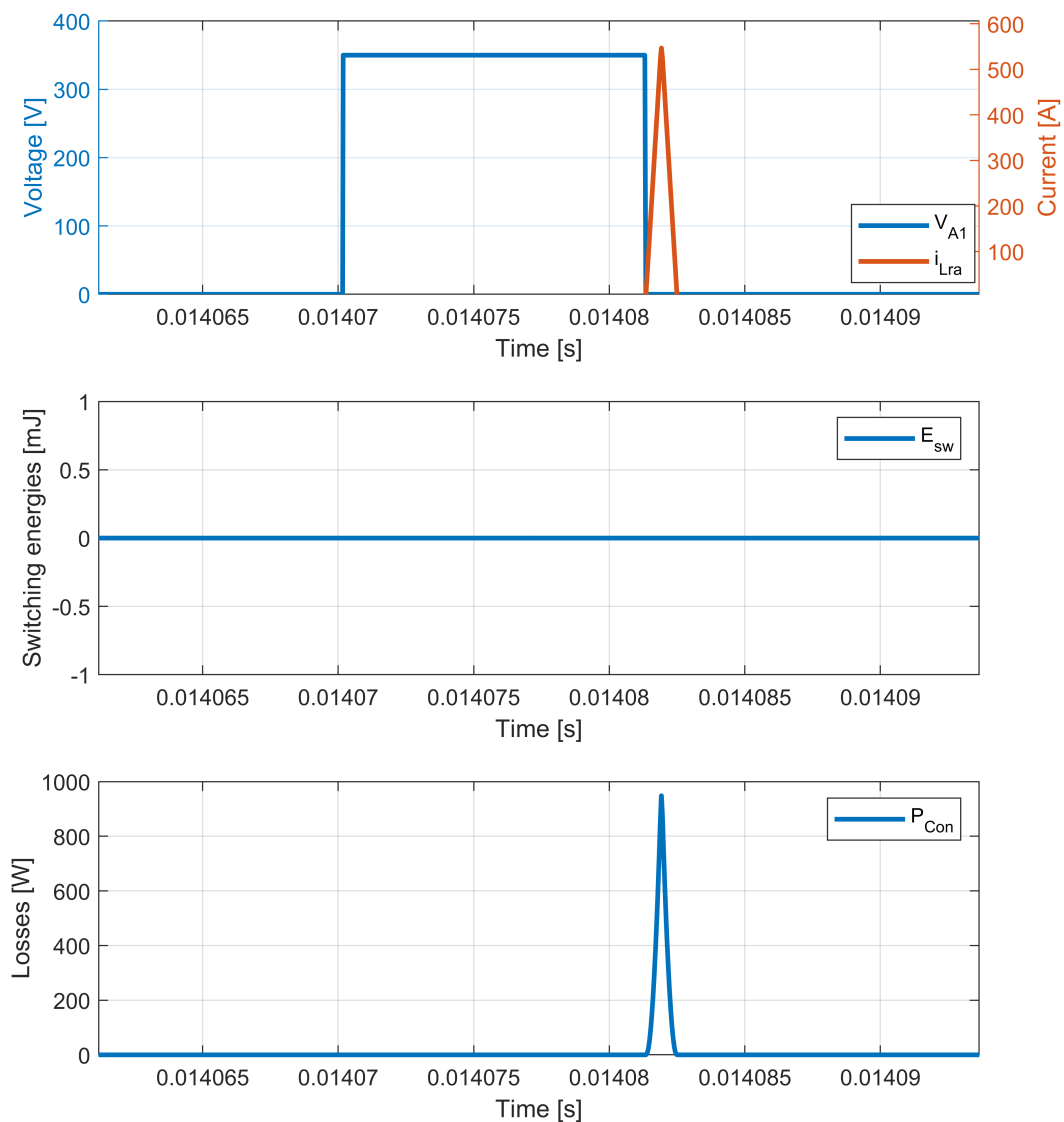


Figure 6.3.10: Zoomed-in plot showing voltage and current (top plot), switching energies (middle plot), and conduction losses (bottom plot) of one of the Auxiliary switch A_1 in phase leg A.

6.4 Comparison of ACRDCLI, ARCPI with HSI

In this section two soft switching topologies the ACRDCLI, the ARCPI will be compared with the HSI. As can be seen in Table 6.4.1 the total power losses and the harmonics are evaluated with constant reference current $i_q = 550$ A. In ACRDCLI the average resonant frequency (5.3.4) of the resonant circuit is 33 kHz. To compare at the same conditions, The switching frequency f_{sw} of the SVPWM is set to 33 kHz in the ARCPI and the HSI

Table 6.4.1: Average total power losses, efficiency, and the THD of all topologies at 33 kHz switching frequency.

Description	Symbol	HSI-hysteresis	ACRDCLI	HSI-SVPWM	ARCPI
Switching frequency	f_{sw} [kHz]	33	33	33*	33
Conduction losses	P_{con} [kW]	1.46	1.4	1.47	1.7
Switching losses	P_{sw} [kW]	1.9	0.05	1.22	0.02
Auxiliary switch losses	P_{Aux} [kW]	-	0.2	-	0.09
ESR losses	P_{ESR} [kW]	-	0.15	-	0.001
Resonant inductor losse	P_{Lr} [kW]	-	1	-	0.388
Total losses	P_{tot} [kW]	3.36	2.80	2.69	2.19
Output power	P_{out} [kW]	84.48	84.00	84.28	84.26
Efficiency	η [%]	96.17	96.77	96.90	97.46
THD	[%]	2.83	6.41	0.85	0.42

The calculated conduction losses according to Section 2.3.2 for the six main switches and the six diodes are similar in the HSI and the ACRDCLI due to constant current flowing through the main switches. However, it can be seen that for the ARCPI the conduction losses are 1.7 kW which are 15% slightly higher than the other topologies. This was due to more losses in the diodes of ARCPI compared to other topologies. The HSI with hysteresis current control method gives more switching losses (2.3.1) of 1.9 kW. This is due to the fact that when the actual current reached the hysteresis band, the controller still waits for the next switching period. So, the current will go higher than the hysteresis band which gives more switching losses with the same switching frequency with hysteresis current control in the HSI.

As expected the switching losses with soft switching are substantially lower which is about a 98 % reduction compared to HSI. The total additional component losses (3.3) for ACRDCLI is 1.35 kW which is about 45 % of the total power losses whereas for the ARCPI the losses (4.3) are relatively lower.

What is interesting about the data in this table is that the total losses of soft switching topologies are lower than that of the HSI with the same control method and with similar output power. Compared to HSI, the reduction of total power losses of the soft switching topologies is about 18 %. ACRDCLI causes higher THD (2.5) on the output current compared to HSI and ARCPI. It is apparent from this table that ACRDCLI has higher resonant circuit losses and worse load current THD. To analyse the performance of ACRDCLI with different switching frequencies, redesigning the resonant circuit is needed. This increases the complexity of the circuit as well as the uncertainty. The above factors have led to the abandonment of ACRDCLI, and further analysis will focus on the performance of the ARCPI.

6.5 ARCPI performance

The performance of the ARCPI is evaluated with different current operating points or different frequency operating points and compared with the HSI.

The left plot in the Figure 6.5.1 shows the average power losses operating at different current conditions with constant switching frequency of 33 kHz. It can be observed that with the increasing i_q , the average total power losses of the both topologies are increasing. The average total power losses of ARCPI are lower than that of HSI in all current operating points ranging from 100 to 550 A. The losses difference gets higher with increasing i_q . The average total power losses of the ARCPI and the HSI with the current $i_q = 550$ A are 2.19 kW and 2.69 kW respectively.

The right plot in the Figure 6.5.1 shows the average total power losses of the ARCPI and the HSI with different PWM switching frequencies and the reference current $i_q = 550$ A. The average total power losses of both topologies get greater with increasing switching frequency, the slope is steeper for HSI. Also, the total losses of HSI are higher than that of ARCPI in all frequency operating points, the losses difference has become even greater with increasing switching frequency. The deviation trend is more significant compared to that of different current operating points. For the highest switching frequency 80 kHz, the average total power losses of ARCPI and HSI are 2.96 kW and 4.6 kW respectively. So the switching frequency is the more influential factor for losses for both topologies compared to the current.

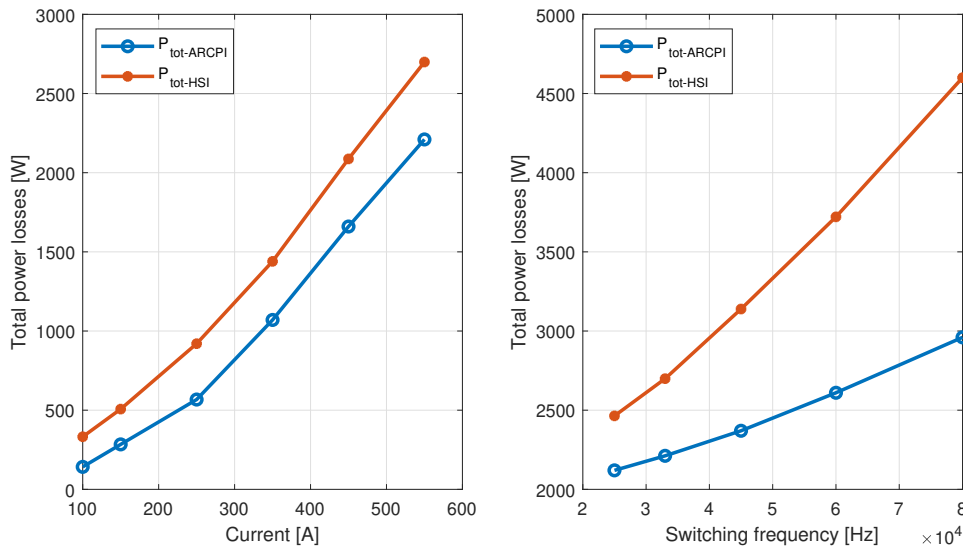


Figure 6.5.1: The average total power losses of the ARCPI and the HSI during one electrical period with different current operating points and switching frequencies. The left plot shows the Total power losses vs the current i_q ranging from 100 A to 550 A with the PWM switching frequency of 33 kHz. The right plot shows the total power losses vs switching frequencies from 25 kHz to 80 kHz with the current $i_q = 550$ A

Figure 6.5.2 shows the switching losses of the ARCPI and the HSI over one switching period with different reference current and switching frequency operating points. What can be seen in the left plot is the average switching losses of HSI is relatively high and increase significantly with higher reference i_q and the switching frequency in this case is 33 kHz.. However, the ARCPI average switching losses are low which is 0.85 W for 100 A and 18.6 W for 550 A. Data in the right plot can be compared with the data in the left plot which shows that the switching losses of the ARCPI are still small with the increasing frequency which is from 17.46 W to 55 W. For the HSI, the switching losses are high and its deviation with different frequencies is even more significant than that of the different currents. This result may be explained by the fact that increasing switching frequency leads to more switching in the same amount of time, which results in higher switching losses.

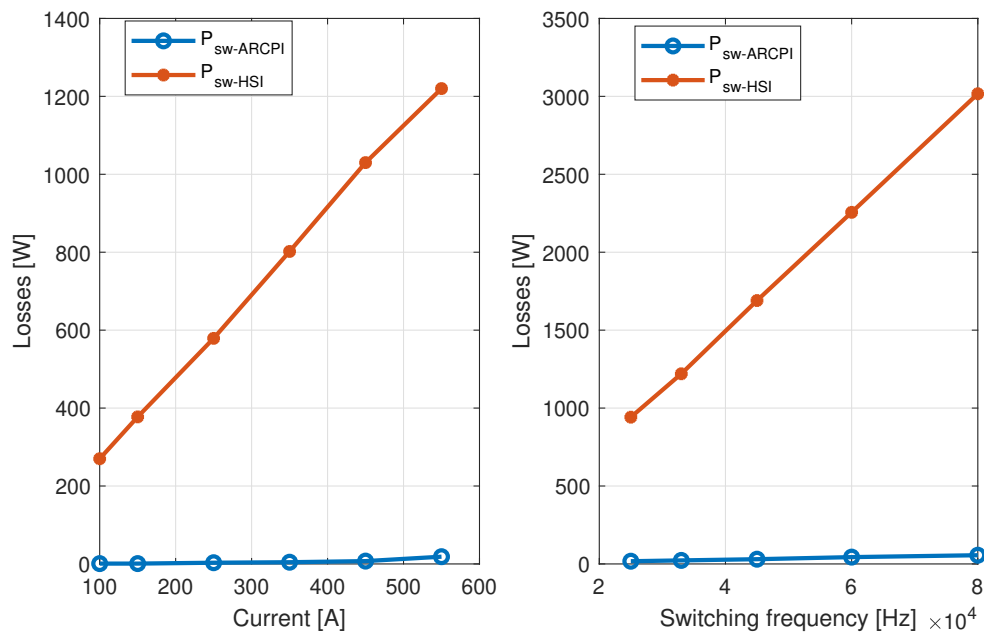


Figure 6.5.2: The average MOSFET switching losses of ARCPI and HSI during one electrical period. (Left plot) shows the switching losses with different current operating points and (Right plot) shows the total switching losses with different switching frequencies.

The left plot in Figure 6.5.3 shows the distribution of the power losses of HSI during one electrical period with different switching frequency operating points. The HSI conduction losses maintain an approximately stable value as the switching frequency increases due to constant current. For the switching losses, it increases with the frequency and the value would be higher than the conduction losses at frequencies above approximately 41 kHz. When the switching frequency is less than this frequency, the switching losses would be lower than the conduction losses. Therefore the switching losses of HSI would be more dominant at high switching frequencies.

The power losses distribution of ARCPI is also analysed which is presented in the right plot of the Figure 6.5.3. The labels from top to bottom are the switching losses, the conduction losses, the auxiliary switch losses, the ESR losses, and the resonant inductor losses respectively. As the switching frequency increases, the conduction losses remain the most dominant losses component with an average value of 1.7 kW. The resonant inductor losses and the auxiliary switch losses will increase with the increasing switching frequency and the trend is approximately linear. In the simulation, the quality factor for the resonant inductor is 200. As the frequency increases, the value of the RMS current increases, and thus the resonant inductor losses also increase. For the ESR losses and the switching losses, the switching frequency has little effect on them, and at 80 kHz frequency, they are 1.3 W and 55 W respectively. What is surprising is that the inductor losses could be an issue at high switching frequencies, but it could probably be improved by better inductance parameters.

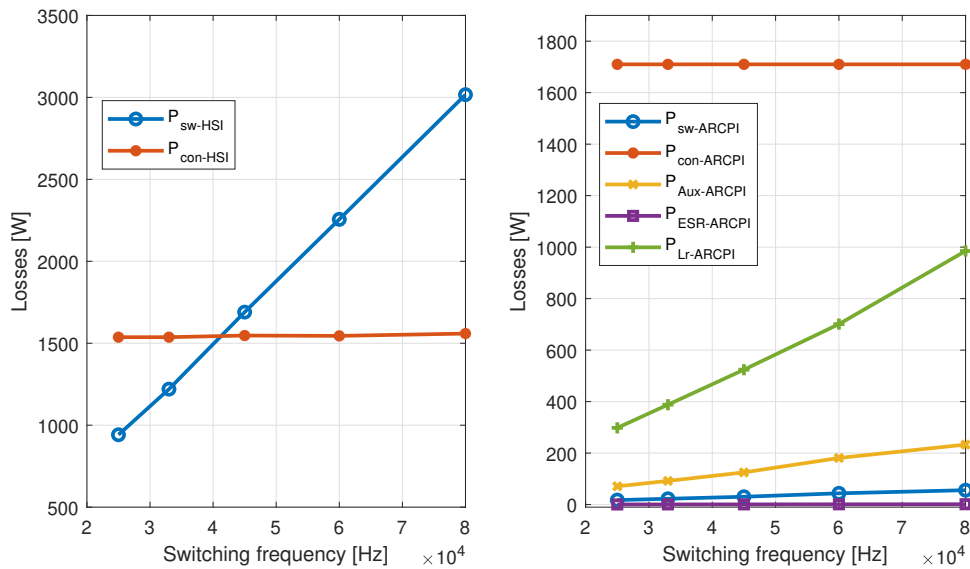


Figure 6.5.3: Simulated results showing the distribution of the power losses of HSI during one electrical period with different switching frequency operating points where the reference $i_q = 550$ A.

As explained in Section 4.3.3 the ESR value for the resonant inductor is calculated using the Quality factor Q . The resonant inductor losses of ARCPI during one electrical period with different switching frequencies and the quality factor are also analysed which is presented in Figure 6.5.4. It can be seen from the figure that lower losses for greater Q due to low ESR value.

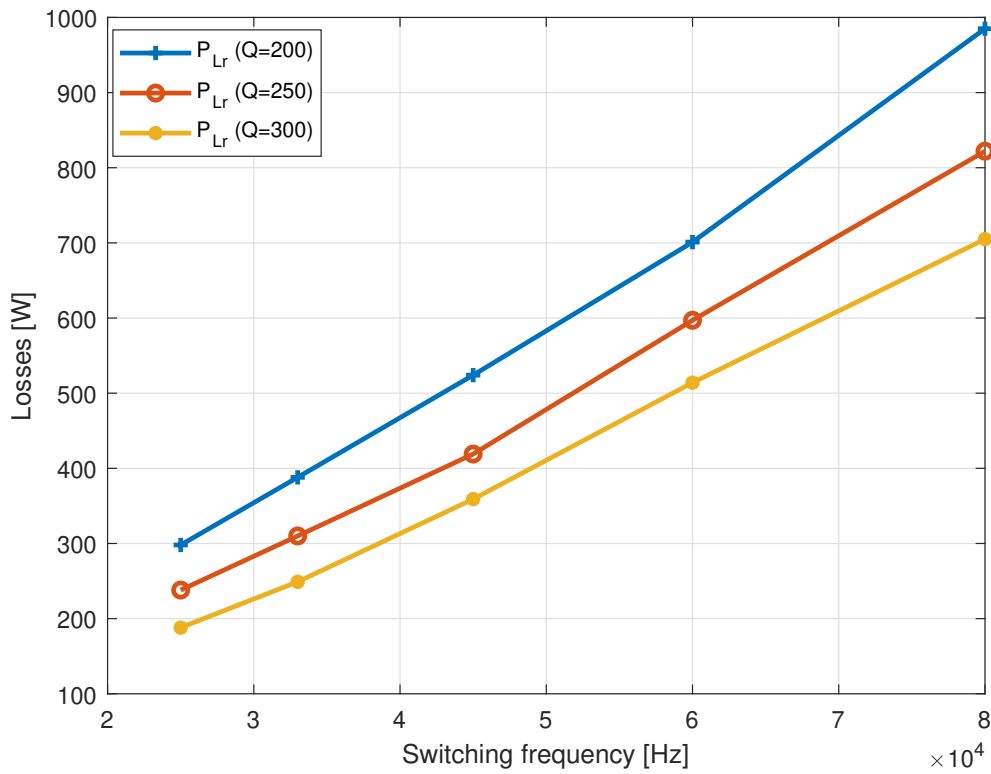


Figure 6.5.4: The resonant inductor losses of ARCPI during one electrical period with different switching frequency operating points and quality factor where the reference current $i_q = 550$ A.

Figure 6.5.5 shows the average load current THD of ARCPI and HSI during three electrical periods with $i_q = 550$ A and different switching frequencies ranging from 25 kHz to 80 kHz. At each operating point, ARCPI has a lower THD than HSI since there is no dead time in the ARCPI which results in lower current distortion. With increasing switching frequencies, the switching periods are smaller so the THD for both topologies is decreasing and the difference gets smaller. THD for HSI is in the range of 1.09 % to 0.366 % whereas for ARCPI THD value is between 0.5417 % to 0.286 %.

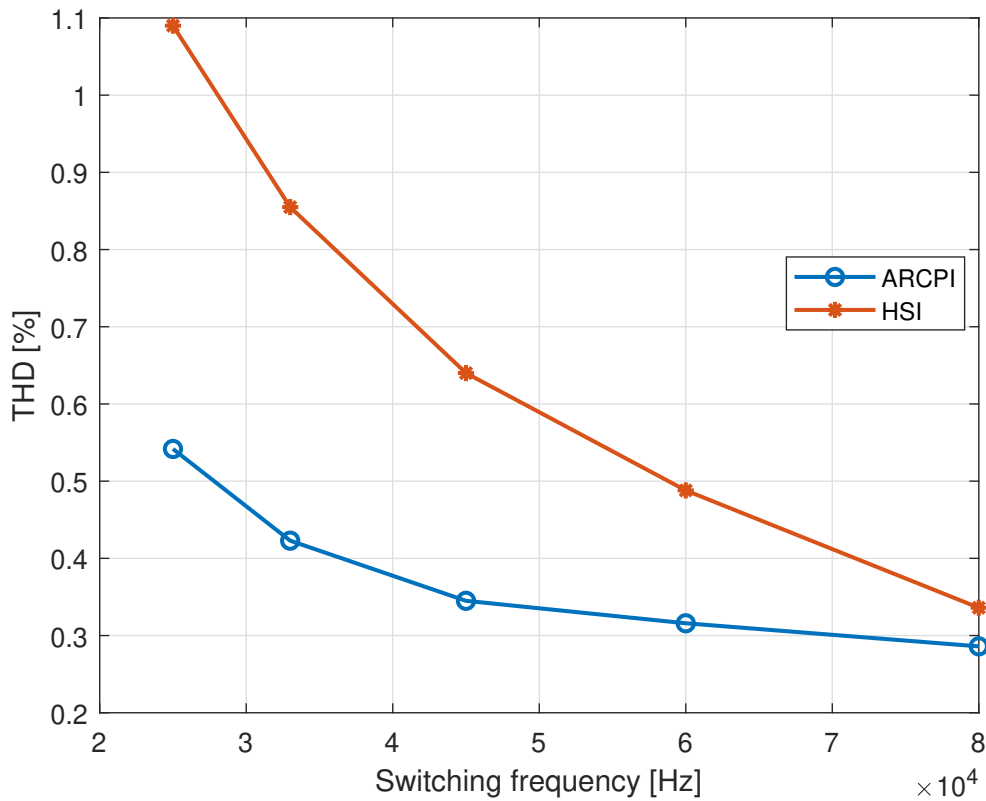


Figure 6.5.5: The average load current THD of ARCPI and HSI during three electrical periods with $i_q = 550$ A and different switching frequency operating points.

The efficiency of the inverter at high switching frequency is analyzed in Figure 6.5.6. The input DC link voltage of 700 V is applied and the output power is 84.26 kW. As the total power losses increases by increasing switching frequency, the efficiency of the inverter decreases. The maximum efficiency of the ARCPI is 97.57 % at $f_{sw} = 25$ kHz. At high switching frequency there is a efficiency improvement of 1.5 - 1.71 % with ARCPI compared to HSI.

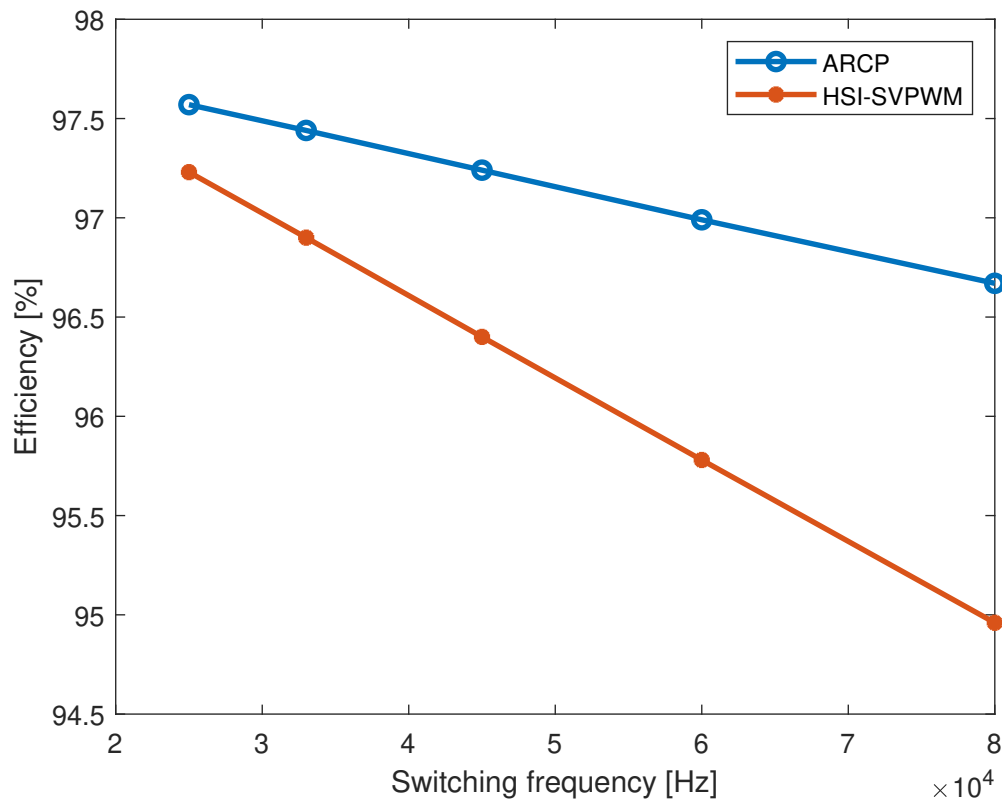


Figure 6.5.6: Efficiency of ARCPI and HSI during one electrical period with $i_q = 550$ A and different switching frequency operating points.

6.6 Component number comparison

In addition to performance, circuit complexity was also analysed by comparing the number of circuit components in the simulation. HSI, ACRDCLI and ARCPI have 6 main switches, but different circuits results in different auxiliary component numbers. There is no extra component needed for HSI in this project since it uses hard switching. ACRDCLI has a resonant circuit and a clamp circuit so it requires 4 extra components to operate soft switching. For ARCPI, three auxiliary circuits and 6 resonant capacitors are needed for zero voltage switching so there are 15 extra components. Table 6.6.1 shows the component number for three topologies.

Table 6.6.1: Circuit component number for three topologies

Number of components	HSI	ACRDCLI	ARCPI
Main switches	6	6	6
Auxiliary switches	-	1	6
Resonant capacitor	-	1	6
Resonant inductor	-	1	3
Clamp capacitor	-	1	-

7

Conclusion and Future work

This project was undertaken to simulate two soft switching inverters and evaluate their losses and harmonics compared to HSI for an EV application. The same operating conditions are applied to all topologies and different control methods were implemented for ACRDCLI and ARCPI. However, a fair comparison is still made to see their performance.

At 33 kHz switching frequency the results of the simulation show that both soft switching topologies have an 18 % reduction of the total power losses compared to HSI. The switching losses in the main switches with soft switching topologies are substantially lower which is about a 98 % reduction compared to HSI. What is surprising is that at the same output power the conduction losses for ARCPI are 15 % higher compared to ACRDCLI and HSI. It was noticed that this increase was due to more losses in the diodes and considerably further work is needed to determine these losses.

The loss equations for additional components were presented for ACRDCLI and the ARCPI which includes the Auxiliary switch losses, ESR losses and the resonant inductor losses. The dominant losses are the resonant inductor losses with the value of 1 kW in the ACRDCLI whereas for the ARCPI the losses are 0.388 kW. However, these losses could be improved with low ESR value. Future studies could be to design the resonant inductor with better quality factor Q and to calculate the other losses such as core losses, hysteresis, and eddy current losses.

The THD value of the motor current at 33 kHz for ACRDCLI is 6.41 % which is higher compared to HSI with hysteresis control. To see the performance of ACRDCLI at high switching frequencies resonant circuit components need to be designed. Further work could be done to carefully select the switching frequency to avoid distortion in the motor current. In addition, an improved soft switching inverter QRDCLI could be implemented with SVPWM technique for better performance. At different switching frequencies ranging from 25 kHz to 80 kHz, THD for ARCPI is between 0.5417 % to 0.286 % whereas for HSI the value is in the range of 1.09 % to 0.366 % . There is a significant reduction of harmonics with ARCPI compared to ACRDCLI.

By comparing the number of components ARCPI requires 15 additional components whereas ACRDCLI has 4 extra components for soft switching. The major disadvantage of soft switching inverters is control complexity and the many compo-

nents.

Overall ARCPI becomes advantageous with a reduction of harmonics and an efficiency improvement of 1.71 % at higher switching frequencies compared to HSI.

Future work could be to see the effect of voltage balance on ARCPI by connecting the auxiliary circuit to the mid-point of the DC link capacitor, which might cause voltage imbalance. Another problem with soft switching is that simulation takes a few hours to finish due to less sampling time. Due to this temperature variation of the switches could not be analysed. To reduce the simulation run time control can be implemented in PLECS instead of Matlab. Furthermore, many modified soft switching topologies have been proposed which could be worth investigating to overcome these problems.

References

- [1] X. Xu and V. Sankaran, "Power electronics in electric vehicles: Challenges and opportunities," 463–469 vol.1, 1993. DOI: 10.1109/IAS.1993.298964.
- [2] Z. Hong, R. Duke, and S. Round, "A resonant dc link inverter for an electric vehicle," pp. 32–37, 2000.
- [3] W. Dong *et al.*, "Comprehensive evaluation of auxiliary resonant commutated pole inverter for electric vehicle applications," in *2001 IEEE 32nd Annual Power Electronics Specialists Conference (IEEE Cat. No.01CH37230)*, vol. 2, 2001, 625–630 vol.2. DOI: 10.1109/PESC.2001.954186.
- [4] D. Divan, "The resonant dc link converter-a new concept in static power conversion," *IEEE Transactions on Industry Applications*, vol. 25, no. 2, pp. 317–325, 1989. DOI: 10.1109/28.25548.
- [5] T. W. Ching, "Soft-switching converters for electric vehicle propulsion," *Journal of Asian Electric Vehicles*, vol. 5, no. 2, pp. 1019–1026, 2007. DOI: 10.4130/jaev.5.1019.
- [6] D. Divan and I. Wallace, "New developments in resonant dc link inverters," in *Proceedings of Power Conversion Conference - PCC '97*, vol. 1, 1997, 311–318 vol.1. DOI: 10.1109/PCCON.1997.645631.
- [7] D. Vracar and S. Vukosavic, "Resonant dc link inverter: Mathematical modeling and computer simulations," in *EUROCON 2005 - The International Conference on "Computer as a Tool"*, vol. 2, 2005, pp. 1679–1682. DOI: 10.1109/EURCON.2005.1630295.
- [8] M.-C. Jiang *et al.*, "Analysis and design of a novel soft-switching three-phase inverter," in *The 2010 International Power Electronics Conference - ECCE ASIA -*, 2010, pp. 125–130. DOI: 10.1109/IPEC.2010.5543861.
- [9] M. Bellar *et al.*, "A review of soft-switched dc-ac converters," *IEEE Transactions on Industry Applications*, vol. 34, no. 4, pp. 847–860, 1998. DOI: 10.1109/28.703992.
- [10] R. De Doncker and J. Lyons, "The auxiliary resonant commutated pole converter," in *Conference Record of the 1990 IEEE Industry Applications Society Annual Meeting*, 1990, 1228–1235 vol.2. DOI: 10.1109/IAS.1990.152341.
- [11] W. Dong *et al.*, "Efficiency considerations of load side soft-switching inverters for electric vehicle applications," in *APEC 2000. Fifteenth Annual IEEE Applied Power Electronics Conference and Exposition (Cat. No.00CH37058)*, vol. 2, 2000, 1049–1055 vol.2. DOI: 10.1109/APEC.2000.822818.
- [12] V. Deshpande, S. Doradla, and D. Divan, "A current-prediction scheme for the prdcl inverter-fed induction motor drive," *IEEE Transactions on Power Electronics*, vol. 12, no. 1, pp. 64–71, 1997. DOI: 10.1109/63.554170.

- [13] Y. Wu *et al.*, “Generalized space-vector-modulation method for soft-switching three-phase inverters,” *IEEE Transactions on Power Electronics*, vol. 36, no. 5, pp. 6030–6045, 2021. DOI: 10.1109/TPEL.2020.3026824.
- [14] H.-J. Pfisterer and H. Spath, “Switching behaviour of an auxiliary resonant commutated pole (arcp) converter,” in *7th IEEE International Power Electronics Congress. Technical Proceedings. CIEP 2000 (Cat. No.00TH8529)*, 2000, pp. 359–364. DOI: 10.1109/CIEP.2000.891440.
- [15] T. Pre-Switch, *Switch demonstrates efficacy of ai-based soft switching using 200kva inverter reference*, Mar. 2020. [Online]. Available: <https://www.pre-switch.com/single-post/2020/03/11/pre-switch-demonstrates-efficacy-of-ai-based-soft-switching-using-200kva-inverter-referen>.
- [16] *Switch presents "disruptive drivetrain technology" - pre-switch*, Jul. 2022. [Online]. Available: <https://www.pre-switch.com/tech/pre-switch-presents-disruptive-drivetrain-technology/>.
- [17] R. Lause and E. Lund, “Design and implementation of a pmsm control system for use in a formula student car,” Master’s thesis, Chalmers University of Technology, Gothenburg, 2020.
- [18] L. Harnefors, *Control of Variable-speed Drives*. Applied Signal Processing and Control, Department of Electronics, Mälardalen University, 2002. [Online]. Available: <https://books.google.se/books?id=wyXXjwEACAAJ>.
- [19] C. J. O’Rourke *et al.*, “A geometric interpretation of reference frames and transformations: Dq0, clarke, and park,” *IEEE Transactions on Energy Conversion*, vol. 34, no. 4, pp. 2070–2083, 2019. DOI: 10.1109/TEC.2019.2941175.
- [20] D. J. Schönberger, “Space vector control of a three-phase rectifier using plects,” Plexim GmbH, Technoparkstrasse 1, 8005 Zürich.
- [21] M. H. N. Talib *et al.*, “Hysteresis current control of induction motor drives using dsp dsp controller,” in *2016 IEEE International Conference on Power and Energy (PECon)*, 2016, pp. 522–527. DOI: 10.1109/PECON.2016.7951617.
- [22] L. Syamala *et al.*, “Hysteresis based quasi fixed frequency current control of single phase full bridge grid integrated voltage source inverter,” *Energies*, vol. 15, no. 21, 2022, ISSN: 1996-1073. DOI: 10.3390/en15218112. [Online]. Available: <https://www.mdpi.com/1996-1073/15/21/8112>.
- [23] A. Acquaviva *et al.*, “Analytical conduction loss calculation of a mosfet three-phase inverter accounting for the reverse conduction and the blanking time,” *IEEE Transactions on Industrial Electronics*, vol. 68, no. 8, pp. 6682–6691, 2021. DOI: 10.1109/TIE.2020.3003586.
- [24] S. A. manual, “Power semiconductors,” second edition, 2015.
- [25] Q. Wang, “Investigation and implementation of mosfets losses equations in a three-phase inverter,” Master’s thesis, Chalmers University of Technology, Gothenburg, 2015.
- [26] A. K. D. Graovac M. Pürschel, “Mosfet power losses calculation using the data sheet parameters,” Infineon Application Note, V 1.1, July 2006.
- [27] H. Bai *et al.*, “Device-level modelling and fpga-based real-time simulation of the power electronic system in fuel cell electric vehicle,” *IET Power Electronics*, vol. 12, Nov. 2019. DOI: 10.1049/iet-pe1.2019.0101.

-
- [28] Z. Hong, “A resonant dc link inverter for an electric vehicle,” Thesis, University of Canterbury, Electrical and Electronic Engineering, 2000.
- [29] L. G. B. Rolim, “Investigation of a drive system: Soft-switched converter and switched reluctance motor,” Dr.-Ing. dissertation, Technische Universität Berlin, Berlin, Germany, 1997.
- [30] D. Divan and G. Skibinski, “Zero-switching-loss inverters for high-power applications,” *IEEE Transactions on Industry Applications*, vol. 25, no. 4, pp. 634–643, 1989. DOI: 10.1109/28.31240.
- [31] A. Tuckey and D. Patterson, “A minimum loss inductor design for an actively clamped resonant dc link inverter,” in *Conference Record of the 2000 IEEE Industry Applications Conference. Thirty-Fifth IAS Annual Meeting and World Conference on Industrial Applications of Electrical Energy (Cat. No.00CH37129)*, vol. 5, 2000, 3119–3126 vol.5. DOI: 10.1109/IAS.2000.882611.
- [32] E. A. Walters and O. Wasynczuk, *Analysis of the auxiliary resonant commutated pole inverter*. [Online]. Available: <https://docs.lib.purdue.edu/ecetr/142/>.
- [33] J. Hamond *et al.*, [pdf] *the operation of auxiliary resonant commutated pole (arcp) and its benefits for electric motor drives: Semantic scholar*, Jan. 1970. [Online]. Available: <https://www.semanticscholar.org/paper/The-Operation-of-Auxiliary-Resonant-Commutated-Pole-Hamond-Kroes/a6d3ac012fb2cb79097c56f9bc872e46c189bc78>.
- [34] K. Ma *et al.*, “The evaluation of control strategies for auxiliary resonant commutated pole inverter,” in *2009 IEEE Energy Conversion Congress and Exposition*, 2009, pp. 810–816. DOI: 10.1109/ECCE.2009.5315974.
- [35] D. Đ. Vračar, “A short overview of active-clamped resonant dc link inverter,” in *2020 International Symposium on Industrial Electronics and Applications (INDEL)*, 2020, pp. 1–6. DOI: 10.1109/INDEL50386.2020.9266172.
- [36] A. Guerra, *Switch white paper*, Jun. 2018. [Online]. Available: <https://www.pre-switch.com/single-post/2017/07/06/pre-switch-white-paper>.

DEPARTMENT OF SOME SUBJECT OR TECHNOLOGY
CHALMERS UNIVERSITY OF TECHNOLOGY
Gothenburg, Sweden
www.chalmers.se



CHALMERS
UNIVERSITY OF TECHNOLOGY